Novel Assays of Brain Networks and Applications to Neurodegeneration

By

Kalen John Petersen

Dissertation
Submitted to the Faculty of the
Graduate School of Vanderbilt University
in partial fulfillment of the requirements for the degree of
DOCTOR OF PHILOSOPHY
in
Chemical and Physical Biology
May 31, 2019
Nashville, Tennessee

Approved:
Seth A. Smith, Ph.D.
Victoria L. Morgan, Ph.D.
Kevin D. Niswender, M.D.
Daniel O. Claassen, M.D.
Manus J. Donahue, Ph.D.

To my family, who mean the world to me.

Kristin, I could not have come this far without you.

Your love and faith are the reason I have persevered.

Mom and Dad, you have always been my steadfast supporters and my personal heroes.

Kerianne, I am so proud and grateful you’re my sister.

I love you all more than words can express.

ACKNOWLEDGMENTS

First and foremost, I am thankful to Drs. Daniel Claassen and Manus Donahue, whose devotion to mentorship, love of knowledge, generosity, and friendship have brought me this far. Your extraordinary yin-yang partnership provided the best learning environment a student could hope for. I owe a debt of gratitude to Claassen lab members past and present, including Dr. Paula Trujillo, Adam Stark, Kerry Steed, Jacqueline Reid, Dr. Nelleke van Wouwe, Megan Aumann, Alex Song, Lisa Hale, Alex Lopez, Aaron Tetrault, Olivia Roman, Katie Hay, Neevi Kukreti, and Elizabeth Huitz, as well as the members of the clinical coordinator staff. Likewise, I want to acknowledge current and former Donahue lab members including Dr. Meher Juttukonda, Dr. Rachelle Crescenzi, Spencer Waddle, Katie Lants, Helen Mahaney, and Dr. Jennifer Watchmaker. I have been tremendously encouraged by your constant support and camaraderie. Collaborators including Dr. Benoit Dawant, Srijata Chakravorti, and Dr. Yurui Gao were indispensable in this research, as were Dr. Bennett Landman and the MASI lab, and the Boxer lab at UCSF. Thank you to Dr. Seth Smith, who has invested himself in my success and was always willing to lend an ear, and to Drs. Victoria Morgan and Kevin Niswender for their support and advice. Thank you to the Interdisciplinary Graduate Program, particularly to Carolyn Berry and Drs. Beth Bowman, Michelle Grundy, and Roger Chalkley. I am grateful to the faculty of the Institute for Imaging Science, including Drs. Bruce Damon and John Gore, and to Patty Mueller for making Chemical and Physical Biology a wonderful home for students. This research would not have been possible without the VUIIS technical staff, who often took the time to explain the mysteries of Philips software to me. I am grateful to our funding sources including the National Institutes of Health for making this work possible. I would be remiss without thanking Dr. David Miller, who exemplifies

the spirit of a true scientist, and who helped me along my journey, and his lab members, who have been great supporters and friends of mine. Finally, I want to thank my family, particularly Kristin, Mom, Dad, and Kerianne. You have always believed in me, even when I did not believe in myself. Thank you all from the bottom of my heart.

TABLE OF CONTENTS

LIST OF TABLES

LIST OF FIGURES

LIST OF ABBREVIATIONS

ASL	Arterial spin labeling
ASL-FC	Arterial spin labeling-based functional connectivity
BOLD	Blood oxygenation level-dependent
BOLD-FC	Blood oxygenation level-dependent functional connectivity
CBF	Cerebral blood flow
COMPCOR	Component-based noise correction
d-DRTT	Decussating dentato-rubro-thalamic tract (ipsilateral)
d/nd	Decussating/nondecussating connectivity ratio
DAA	Dopamine agonist
DMN	Default mode network
DRTT	Dentato-rubro-thalamic tract
FA	Fractional anisotropy
FDR	False discovery rate
FEAT	fMRI Expert Analysis Tool
fMRI	Functional magnetic resonance imaging
FSL	FMRIB Software Library
FWHM	Full width at half maximum
GRASE	Gradient and spin echo
GSR	Global signal regression
HCP	Human Connectome Project
ICB	Impulsive and compulsive behaviors
LASSO	Least absolute shrinkage and selection operator
UPDRS	United Parkinson’s Disease Rating Scale
MELODIC	Multivariate Exploratory Linear Optimized Decomposition into Independ. Comp.
MNI	Montreal Neurological Institute
MPRAGE	Magnetization-prepared rapid gradient-echo
MRI	Magnetic resonance imaging
nd-DRTT	Nondecussating dentato-rubro-thalamic tract (contralateral)

pCASL	Pseudo-continuous arterial spin labeling
PD	Parkinson’s disease
PSP	Progressive supranuclear palsy
QUIP-RS	Questionnaire for Impulsive-Compulsive Disorders in Park. Dis.-Rating Scale
ROI	Region-of-interest
RSN	Resting-state network
SCP	Superior cerebellar peduncle
SENSE	Sensitivity encoding
SMN	Sensorimotor network
SNR	Signal-to-noise ratio
SPM	Statistical parametric mapping
TE	Echo time
TFCE	Threshold-free cluster enhancement
TI	Inversion time
TR	Repetition time
VN	Visual network

CHAPTER 1

INTRODUCTION AND BACKGROUND

1.1 Brain connectivity

Network organization of the brain

Information processing in the brain is both localized and distributed. The cortex is regionally specialized, but also depends on communication at a distance. Interconnected areas sharing common functions are termed brain networks, and the brain as a whole may be considered a composite of such networks (Park and Friston, 2013; Sporns et al., 2004). Brain networks also extend beyond the cerebral cortex, including the cerebellum and basal ganglia.

The importance of distributed processing vs. regionally specialized activity is one of the oldest debates in neuroscience (Sarter et al., 1996). Early clinical evidence for localization came from lesion studies, in which behavioral or sensorimotor dysfunction was linked to focal sites of brain damage (Ferrier, 1876). Most famously, Paul Broca demonstrated that speech production localizes to the eponymous ventral posterior region of the frontal lobe (Broca, 1861). Other founding evidence for localization of function came from electrical stimulation experiments, which proved that cortical surface areas have discrete roles in sensation, movement, and cognition (Fritsch and Hitzig, 1870). This approach was pioneered in humans by neurosurgeon Wilder Penfield, whose tests on epileptic patients resulted in detailed motor cortex maps (Penfield and Boldrey, 1937). Lesion and stimulation approaches enabled identification of the primary motor cortex, somatosensory cortex, and the visual and auditory cortices.

In recent years, simplistic ‘localizationist’ and ‘distributionist’ views have given way to the understanding that both regional and network processing are present in brain architecture, and that the degree of distribution varies among brain systems. The most important contemporary questions concern the anatomical structure of brain networks, their functional correlates, and the spatial and temporal scales over which they communicate (Mesulam, 1994).

Long before the advent of magnetic resonance imaging techniques, it was evident that sensorimotor cortex could not account for the full range of cortical activity, and that cognitive, behavioral, and emotional processes were not as readily localized. Such diverse mental functions are the province of the association cortices, broadly defined as gray matter regions not belonging to specific sensorimotor zones. The term ‘association cortex’ has been used rather nonspecifically to refer to the entirety of the nonmotor frontal lobe, along with extensive swaths of parietal, paralimbic, and temporal cortex (Pandya and Yeterian, 2013).

The participation of sensorimotor and associative regions in neural networks is evident in the physical organization of the cortex, with white matter fibers comprised of bundled axons physically linking distant neural populations, allowing the inference of coordinated network activity even without the use of *in vivo* activity measures such as electroencephalography or functional MRI.

Parcellating association areas has often involved cytoarchitectonic properties rather than functional identity; for example, the main subdivisions of the orbitofrontal cortex were based on histologic markers rather than function (Kringelbach, 2005). More detailed descriptions of such regions were problematic until the development of functional MRI, although some inferences could be drawn from animal models, particularly from electrophysiological recording in primates during task performance.

Striato-cortical loops and limbic circuits

An important set of circuits present in both sensorimotor and associative cortex are the striato-pallido-thalamo-cortical loops (or striato-cortical loops), a system of feedback projections between the basal ganglia and cortex (Haber and Behrens, 2014; Middleton and Strick, 2000). Specific frontal cortical regions project to dorsal or ventral striatum, which sends efferents to the globus pallidus, which in turn projects to the thalamus and thence back to the cortex, generally targeting the same region from which the circuit originated. These pathways are well documented in both primate neuroanatomy and human neuroimaging (Draganski et al., 2008). Striato-cortical loop function depends on the specific part of the basal ganglia through which the circuit passes: dorsal striatum mediates motor and pre-motor loops, central striatum integrates cognitive pathways including dorsolateral frontal cortex, and ventral striatum incorporates reward and reinforcement processing in limbic loops. These pathways also maintain separation in their thalamic relays, allowing extensive parallel feedback serving diverse processes (Pessiglione, 2005), although this segregation is incomplete, suggesting that the thalamus performs an integrative function as well, exchanging information between sensation, movement, and motivational systems (Haber, 2011; McFarland and Haber, 2000).

Limbic loops, occupying the most ventral regions of the striatum and most medial portions of the thalamus, provide cortico-striatal feedback for the ventromedial prefrontal and orbitofrontal cortex, along with the anterior cingulate gyrus (Haber, 2011) and the insula, which is considered a lateral portion of the limbic lobe, cytoarchitectontically related to the orbitofrontal cortex (Morgane and Mokler, 2006). Limbic loops receive input from the dopaminergic system at the nucleus accumbens/ventral striatum, integrating the brain’s reward and learning pathways with its major cortical-subcortical communication system. Specifically, the ventral striatum exhibits strong reciprocal connections with the ventral tegmental area, the origin of the mesolimbic pathway (Haber, 2011). Limbic cortico-striatal loops are strongly implicated in behavioral dysfunctions including obsessive-compulsive disorder (Beucke et al., 2013) and substance addictions such as cocaine abuse (Hu et al., 2015). Among these regions, the orbitofrontal cortex plays an especially prominent role in reward-motivated decision-making processes.

Orbitofrontal cortex function

The orbitofrontal cortex (OFC) refers to the extensive region occupying the ventral surface of the frontal lobe. It combines sensory information about external stimuli such as reward or punishment cues with subjective emotional valance in decision-making processes. The OFC serves as an integrator of convergent sensory information, receiving auditory, visual, olfactory, gustatory, and somatosensory projections (Cavada, 2002). It has extensive connections with other limbic system components, including the anterior cingulate gyrus, ventral striatum/nucleus accumbens, and amygdala (Zald et al., 2014).

The OFC's most frequently described role in behavior is to encode information about reinforcers, tracking perceived (O'Doherty et al., 2000) and expected (Gottfried et al., 2003) values of rewarding or punishing stimuli, making this region highly salient for classical or operant learning processes. In primate studies, activity in individual OFC neurons tracks with flexible stimulus-outcome associations, including in reversal learning (Thorpe et al., 1983). The second functional category frequently identified with the OFC is the integration of behavior with somatic markers (i.e. physiological responses identified with emotional states). Damage to the OFC inhibits normal physiological-emotional responding to negative outcomes, leading to inflexible behavioral patterns and fixation on risky choices with larger potential rewards, to the detriment of overall success at gaining positive outcomes (Bechara et al., 1994). OFC damage causes impaired assessment of consequences, summed up as “myopia for the future” (Bechara and Dolan, 2002). A third view posits that OFC activity reflects the subjective economic value of stimuli. Evidence for this hypothesis comes from single-neuron recordings where OFC firing correlates with the degree of preference for a stimulus, i.e. its perceived value (Padoa-Schioppa, 2011).

It is important to note that these three major descriptions are not mutually exclusive; rather, OFC may combine the processes of stimulus-outcome learning, value perception, and emotional processing, enabling a complex set of behavioral responses to environmental cues. It is also likely that the OFC’s ability to regulate comportment depends critically on specialization of its sub-regions, which exhibit different patterns of cytoarchitecture, connectivity, and functional relevance (Kringelbach and Rolls, 2004).

Organization of the orbitofrontal cortex

Evidence from neuroimaging suggests that the OFC is primarily divisible into a medial-caudolateral network ('medial OFC'), and a lateral-orbital network ('lateral OFC') (Kahnt et al., 2012; Kringelbach, 2005). These subdivisions perform separate decision-making functions, with medial OFC representing rewarding stimuli, and lateral OFC responding to punishing reinforcers (Kringelbach, 2005).

Medial and lateral OFC also involve different white matter pathways; the former is more connected with the hippocampus and anterior cingulate cortex, and the latter with the sensory cortices (Cavada, 2002). An anterior-posterior gradient is also proposed, with posterior OFC responding more strongly to unreinforced primary rewards such as food, and anterior regions to more abstract and indirect stimuli, such as monetary incentives (Sescousse et al., 2013). Posterior

OFC features extensive connectivity with the amygdala, and is believed to modulate autonomic responding in a dopamine-dependent manner (Zikopoulos et al., 2017).

The idea of medial and lateral OFC subdivisions originated with Brodmann's famous atlas (1909), which divided the ventral OFC surface into three areas: 10, 11, and 47. Area 11 is roughly synonymous with the medial OFC, and along with the gyrus rectus consists of six-layered isocortex (Henssen et al., 2016). Medial parts of area 47 may also be included in the medial OFC. The lateral OFC consists of the central and lateral parts of area 47 and components of area 10 (Barbas, 2010).

Beyond Brodmann's general divisions, there is little strong agreement on the nomenclature for much of the human OFC, and several divergent naming schemes exist, a situation complicated by great variability of gyri and sulci among individuals. However, medial and lateral OFC are distinguishable on the basis of cytoarchitectonic, histological, and morphometric properties. These include layer IV granularity, cell density, cell size, and cortical thickness, as well as neurofilament staining. Cytoarchitecture less specifically distinguishes anterior and posterior OFC, with increasing dysgranularity marking the posterior regions near the insula (Uylings et al., 2010).

The orbitofrontal cortex and the anatomically proximate, functionally related anterior cingulate cortex participate in a series of cortico-striatal feedback circuits with the basal ganglia. These limbic loops are homologous to the motor loops of the dorsal striatum; however, they are primarily mediated via the ventral striatum/nucleus accumbens rather than the caudate and putamen (Alexander et al., 1986).

1.2 Imaging approaches to brain connectivity

Human brain networks such as the cortico-striatal loops described above can be explored with two main approaches: functional and structural connectivity. While both of these interpretive strategies can be studied with *in vivo* MRI, they can derive from fundamentally different modalities: functional MRI and diffusion-weighted imaging, respectively. Here, we will detail these methods and describe their application to the science of brain connectivity, and also discuss how structure and function can provide supporting information about brain organization and physiology, serving as mutual checks or sources of validation.

Functional MRI and the BOLD contrast

Functional MRI (fMRI) techniques seek to reflect measurements of dynamic brain activity rather than static tissue properties. Generically, fMRI refers to sequences designed to detect fluctuations in the blood oxygenation level-dependent (BOLD) effect resulting from prompted neural responses to experimental conditions, although other MRI contrasts may also be used for fMRI. The BOLD contrast depends on the difference in magnetic susceptibility between oxygen-bound hemoglobin (oxyhemoglobin) and unbound hemoglobin (deoxyhemoglobin) in brain vasculature. The former is diamagnetic, and does not distort external magnetic fields, while the latter is slightly paramagnetic, distorting adjacent field lines and producing transverse (T_2) dephasing. The paramagnetism of deoxyhemoglobin changes the fields experienced by water protons, resulting in accelerated loss of the MRI signal.

BOLD fMRI sequences are designed to exploit this effect when measuring vascular responses to brain activity (Ogawa et al., 1993, 1990). Increased activity in neuron populations causes a rapid elevation of oxygen consumption from the feeding capillary system. Naïvely, this leads to the prediction that activity would decrease fMRI signal by increasing the proportion of T_2-dephasing deoxyhemoglobin. However, this assumption neglects the coupled hemodynamic response, a critical but incompletely understood phenomenon in which cerebral blood flow (CBF) rises in response to metabolic demand, delivering increased volumes of oxygenated blood to tissue (Buxton et al., 2004). The effect of elevated CBF is a large increase in oxyhemoglobin delivery, which overcompensates for the smaller increase in the rate of oxygen consumption. This imbalance results in a smaller proportion of deoxyhemoglobin in venous vasculature, and is responsible for the BOLD effect.

The hemodynamic response function in fMRI consists of three phases. The first is a small, transient dip, likely due to the initial increase in oxygen consumption, which occurs before the vasculature can respond with compensatory blood flow. This is rapidly followed by a sustained, higher-magnitude increase in fMRI signal as excess oxygen-rich arterial blood is directed to the tissue, and finally by a post-stimulus undershoot. The net result of the hemodynamic response is higher oxygenation in draining blood, particularly in the veins serving the activated area (**Fig. 1-1**). This venous-side bias is due to the lower oxygenation saturation in blood returning to the heart: while arterial O_2 in healthy subjects is consistently near full saturation (~98%), oxygenation in veins depends on several

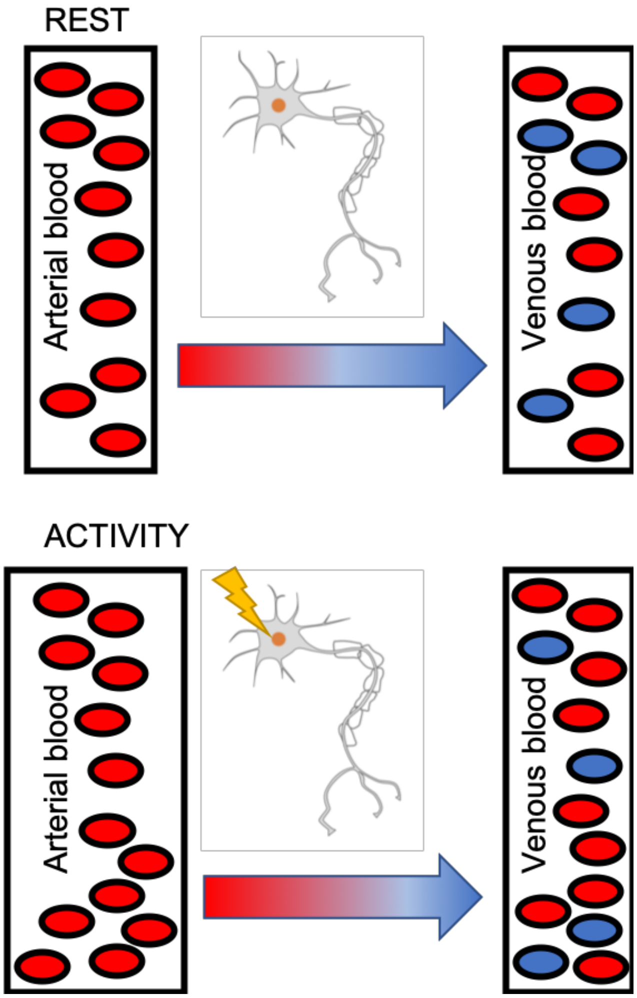

Fig. 1-1. The hemodynamic response. Illustration of the vascular response to neural activity, which is the basis for the blood oxygenation dependent (BOLD) signal. Increased cerebral blood flow in reaction to neural activity results in greater oxygen delivery to tissue. This hemodynamic response outweighs the smaller increase in metabolic oxygen consumption due to neural activity. Consequently, paramagnetic deoxyhemoglobin constitutes a smaller proportion of the draining vasculature, and the MRI signal is increased.

metabolic factors. These include CBF, the rate of blood delivery to tissue (ml of blood/100 g tissue/minute); cerebral blood volume (CBV), the quantity of blood in brain tissue (ml blood/100 g tissue); cerebral metabolic rate of oxygen consumption ($CMRO_2$; O_2/100g tissue/min) and oxygen extraction fraction (OEF), the proportion of arterial oxygen used by the tissue or returned to the veins (Duong et al., 2003; Kim et al., 1994).

Consequently, elevated metabolic demand due to neural activation produces a delayed, transient signal increase when measured with long echo-time (TE) acquisitions. Gradient-echo sequences in particular maximize the measured BOLD effect by matching TE to tissue effective T_2 (T_2*). While spin echo MRI can be used in fMRI sequences, especially at very high field strength, gradient echoes are utilized in the majority of fMRI experiments at field strengths of 3.0 Tesla or below. Gradient echoes do not refocus spins that are phase-shifted by tissue susceptibility gradients and other inhomogeneity effects, therefore they are predominated by T_2*-determining factors, including deoxyhemoglobin concentration and magnetic field inhomogeneities. Applications of T_2*-weighted BOLD-sensitive techniques include task-based fMRI and task-free (resting-state) functional connectivity.

Limitations of BOLD-fMRI

Sequences exploiting contrast related to BOLD are necessarily sensitive to susceptibility effects, in order to detect subtle variations in deoxyhemoglobin levels. Thus, other sources of magnetic inhomogeneity, such as air-tissue interfaces in the sinuses and aural canal, decrease the fMRI signal in nearby brain regions including the orbitofrontal cortex and portions of the temporal lobe (Ojemann et al., 1997). These T_2*-shortening effects cause distortions in echo planar imaging sequences generally used in fMRI. In task-based fMRI, susceptibility interferes with detection of true activations, but may also produce spurious activations, as regions of high susceptibility will be dominated by structured noise from head movement and physiological sources. While distortion effects can be corrected with field mapping, dropout (i.e. signal loss) caused by high susceptibility causes partial but irreversible signal loss in parts of the OFC (Deichmann et al., 2002). While fMRI activations can still be detected in the ventral prefrontal cortex (Cusack et al., 2005), signal-to-noise is substantially lower than in surrounding regions, raising the possibility of both false negatives and false positives.

Another limitation of fMRI is the spatial source of the BOLD signal. Due to the consistent oxygenation of arterial blood, the venous compartment is overrepresented among signal sources when compared with arteries and capillary beds. This is because measured changes in fMRI intensity will reflect the compartment with greatest activity-related changes in the proportion of deoxyhemoglobin (Duong et al., 2003). This effect can lead to incorrect mapping of fMRI signal sources, as the greatest changes occur in large draining veins located downstream of actual neural activity sites (Krings et al., 1999). Venous effects can confound measurement of correlated signal fluctuation, producing aberrant fMRI experimental results (Boubela et al., 2015). Care must be taken both when designing long-echo time pulse sequences such as T_2*-weighted BOLD, and when interpreting results of these techniques. It is equally important to avoid drawing overly detailed mechanistic conclusions from fMRI results, bearing in mind that the relationship between cellular activity in the cerebral cortex and BOLD effects is complex and incompletely understood.

Arterial spin labeling

Measurement of functional connectivity depends on the vascular response to neural activity. Several interrelated quantities describe hemodynamic responses: cerebral blood flow, blood oxygenation, metabolic rate of oxygen consumption, and oxygen extraction fraction. Each of these factors contributes to the BOLD signal changes during brain activity. While blood oxygenation is the basis for most fMRI, the quantity corresponding most directly to energy consumption in the brain is cerebral blood flow (CBF), which is tightly coupled to glucose metabolism (Jueptner and Weiller, 1995; Musiek et al., 2012). CBF can be measured in absolute quantitative units using the noninvasive MRI technique arterial spin labeling (ASL) (Detre et al., 1992). ASL includes a family of perfusion-weighted sequences in which blood water is labeled by adiabatic spin inversion using a radiofrequency pulse or a series of rapid pulses. Labeling duration (LD) is typically 1.5-2 s for

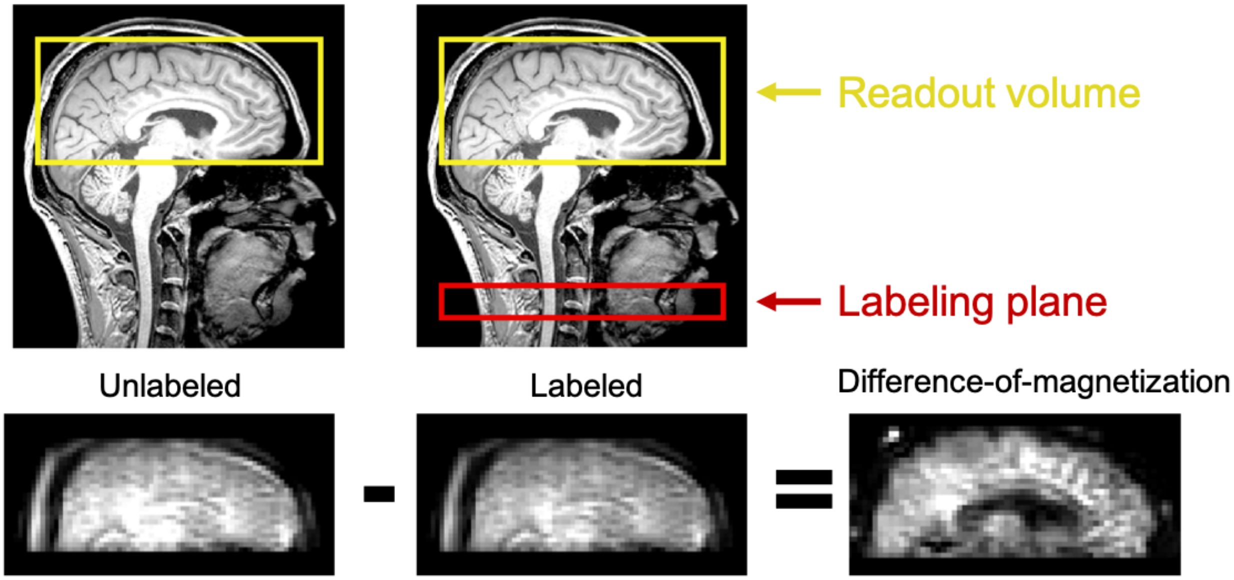

Fig. 1-2. Arterial spin labeling. Illustration of the principle of arterial spin labeling. In the labeled volume, spins in flowing blood water passing through the labeling plane are inverted by a radiofrequency pulse or set of pulses. The inversion pulse attenuates the MR signal and reduces image intensity upon exchange of blood water with tissue. Blood water flows into the head and after a fixed duration a readout is taken at various slices. The unlabeled image is formed by following the same imaging procedure without the labeling step. The difference between these images is proportional to cerebral blood flow. Control-label pairs are acquired repeatedly to reduce the impact of low signal-to-noise.

pseudocontinuous ASL, during which time blood water labeled in the neck flows into the brain for a fixed duration, and an image is then acquired. Spin-labeled water acts as a diffusible tracer which reduces the signal intensity in the capillaries and extravascular compartment.

A second image acquisition is then performed without the spin-labeling module, but otherwise identical to the labeled scan. This image acts as a control for comparison with the labeled image; since spin-labeled water accounts for the only non-noise difference, subtraction results in a perfusion-weighted difference-of-magnetization image, which is proportional to blood flow (**Fig. 1-2**). This result can be converted to actual blood flow units (e.g. ml blood/100 g tissue/min) by means of a Bloch equation modified to include fluid flow (Williams et al., 1992).

The gap between labeling and acquisition (post-labeling delay; PLD) is typically 1.5-2 s, which permits a trade-off between the time needed for water to exchange between capillaries and tissue, and signal loss due to dephasing. The combination of LD and PLD results in a longer TR than in BOLD fMRI.

ASL is also characterized by low signal-to-noise ratio (SNR), especially with single-shot echo planar imaging (EPI) readouts. SNR can be improved with 3D gradient-and-spin-echo (GRASE) readouts, or a higher spatial resolution can be acquired at the same SNR (Gunther et al., 2005).

Functional connectivity

Traditional task-based fMRI compares signal intensity between the resting state and one or more experimental conditions: motor activity, sensory input, cognition, or behavioral states. In a typical experiment, activity or signal change in each volumetric pixel (voxel) in the image is modeled as a function of a time regressor representing the experimental design, with alternating periods of activity and rest. This regressor is convolved with the hemodynamic response function to account for delayed vascular responses. fMRI voxels with activity conforming to the experimental time course are identified as activated in response to the experiment's independent variable, which is the sensory stimulus, motor activity, or mental process of interest to the experimenter. This activation is presumed to reflect underlying neural activity in the cortical or subcortical gray matter. In this context, fMRI signals fluctuating in the absence of an experimental activity are treated as noise. However, repeatable patterns in fMRI residuals resulted in the discovery that functionally meaningful information exists in these dynamics, leading to a new paradigm for fMRI: resting-state functional connectivity (Biswal et al., 1995). This field stemmed from the initial observation that fMRI signals in the right and left motor cortex are correlated even when participants were not engaged in relevant movement.

This concept led to the term resting-state network (RSN)[a]. Further experiments would demonstrate that the entire brain can be described in terms of a set of spatially discrete RSNs, and that an extended fMRI acquisition with no explicit task can resolve RSNs at the level of the single participant or across a group (Fox et al., 2005; Smith et al., 2009; Yeo et al., 2011). Such networks often correspond to regions of known function, which remain connected when that function is not engaged. RSNs include well-defined sensory regions such as the occipital visual cortex and the temporal auditory cortex, which exhibit bilateral synchrony. Other frequently encountered RSNs are defined by their roles in behavioral and neuropsychological processes, such as the salience

---

[a] An important injunction relates to the term ‘resting-state’—although the phrase is utilized here, it should be recognized as a misnomer, since even in the absence of explicit instructions, fMRI participants will engage in a variety of sensory, motor, and cognitive functions, and since the MRI environment is not ideally stimulus-free (noise, light, and physical sensation are not minimized). Other literature may use the phrases ‘intrinsically connected networks’ or ‘baseline connectivity’ in place of ‘resting-state’ to clarify this point.

network or the central executive network. By contrast, the default mode network was first identified by its activity specifically in the absence of externally directed processes, and is thought to be associated with introspection and other reflective states.

Major brain networks

The motor network was the first described RSN, corresponding to areas of previously established somatotopic activations in fMRI experiments involving finger-tapping, limb manipulation, etc., located on the primary motor cortex. However, bilateral coordinated signal was found even without motor activity (Biswal et al., 1995). The proximity of primary motor and sensory cortex makes discrimination of the two regions difficult, and thus the term 'sensorimotor' is often used to refer to the combined regions, which constitute the pre- and post-central gyri.

The visual network occupies the occipital regions which process information from the visual pathway, including the primary and secondary visual cortex, together with adjacent areas associated with visual and visuospatial perception. The visual network can be consistently activated in fMRI experiments by presentation of high-contrast stimuli such as flashing checkerboards; however, the network's connectivity remains apparent even in an eyes-closed state, implying that functional connectivity is not merely a function of sensory co-activation, but rather persistent linkage of activity. The visual network consists of several distinct sub-networks, including a lateral-superior network comprising the peristriate area, and a more medial part consisting of visual regions nearer to the precuneus (Damoiseaux et al., 2006).

Outside of sensory and motor networks, the brain's functional architecture is frequently described in terms of three major RSNs: default mode network, salience network, and central executive network. The default mode network (DMN) is named for its coordinated activity in the absence of directed tasks or major sensory input (Raichle, 2015). It is active during reflective or internally focused states, such as mind-wandering. The DMN consists of spatially separated but linked nodes: the precuneus-posterior cingulate node, the prefrontal node, and the symmetric, bilateral parietal nodes. Default mode network was first identified by its suppression during both metabolic PET studies (Shulman et al., 1997) and task-based fMRI, but was also among the first networks to be described in terms of resting-state functional connectivity (Greicius et al., 2003).

The salience network is involved in integrating sensory input to guide attention to stimuli, and determine the relevance of external information to decision-making (Seeley et al., 2007). The salience network consists of three major hubs: left and right anterior insula and ventromedial prefrontal cortex, including portions of the anterior cingulate and possibly orbitofrontal cortex (Peters et al., 2016). The salience network participates in cortico-striatal loops similar to those in the motor system, which provide

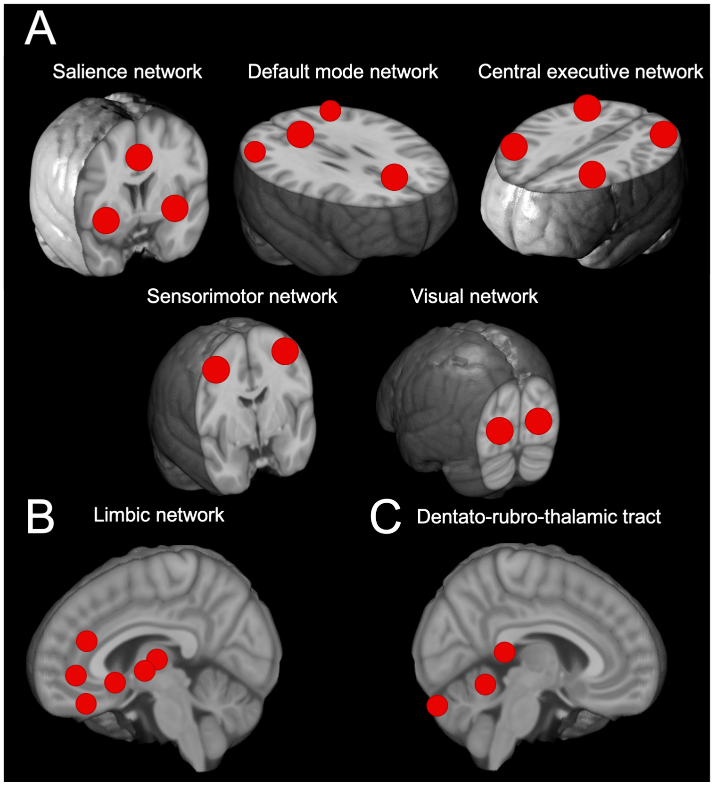

Fig. 1-3. Major brain networks. Simplified schematic of brain networks examined in this dissertation. (A) Frequently discussed resting-state brain networks include and the salience network, default mode network, and central executive network, as well as the bilateral sensorimotor and visual networks. Mapping of these networks using perfusion signals is described in Chapter 4, and this technique is applied to the orbitofrontal cortex in Chapter 5. (B) The limbic network consists of cortico-striatal loops between the basal ganglia and several regions of limbic cortex including the anterior cingulate gyrus, insula, and orbitofrontal cortex. The limbic network is involved in regulation of reward and motivated behavior, as described in Chapter 2. (C) The dentato-rubro-thalamic tract connects the cerebellar deep gray matter to the thalamus via the red nucleus. It modulates feedback from the cerebellum to the cerebral cortex, as described in Chapter 3.

feedback between the cortex and basal ganglia.

The central executive network mediates executive or ‘top-down’ control of cognitive processes (Sauseng et al., 2005). Also known as the fronto-parietal network, the central executive network is essential in the recruitment of other brain networks. Central executive network, default mode network, and salience network are functionally interdependent, as the salience network mediates switching between default mode and central executive networks, promoting transition between internally directed activities and task-oriented processes (Goulden et al., 2014; Sridharan et al., 2008).

These RSNs are summarized in **Fig. 1-3A**. While these are commonly described networks, they are not exhaustive descriptions of the sensorimotor and associative cortices. It is also important to note RSN description depends on the granularity used in the subdivision of networks. For instance, the central executive network appears in some studies as a bilateral unitary RSN, while in others it may be identified as two separate lateralized networks. Likewise, the default mode network may be found as a single structure of as separate frontal and posterior components. Because functional connectivity results are very sensitive to the choice of methodology, it is essential to understand functional connectivity in the light of the underlying anatomy of interconnected gray and white matter.

Structural connectivity

Structural connectivity is the arrangement of the brain’s axonal pathways. Anatomically, it refers to the physical course of white matter bundles linking gray matter structures, including non-contiguous zones of the cortical ribbon and the basal ganglia, brainstem, and cerebellum. Classical methods for mapping structural connectivity include postmortem dissection with white matter tract tracing and anterograde or retrograde labeling of neurons in animal models, in which an injected tracer such as a fluorescent protein undergoes axonal transport and its resulting distribution in neurons is imaged. In the context of MRI, however, structural connectivity is most often characterized *in vivo* using diffusion-weighted MRI and fiber tractography.

The principle of diffusion-weighted MRI depends on measuring the movements of water molecules. When water is unhindered, it diffuses randomly in all directions from a point of origin under Brownian motion. Such diffusion is termed isotropic. However, the presence of barriers on the time scale associated with molecular diffusion constrains motion in a non-random fashion. This is referred to as anisotropic diffusion (Beaulieu, 2002). The biological structures most relevant to this phenomenon are cell and axonal membranes, since the micron-scale diameter of membranes impairs water diffusion on time scales associated with conventional diffusion-weighted MRI sequences.

Diffusion-weighted imaging requires paired diffusion-sensitizing magnetic field gradients, which subject water protons to different fields based on their location in space, causing them to dephase in spin-echo diffusion-weighted MRI. Diffusion-sensitizing gradients are applied in a paired manner on either side of a refocusing pulse, such that the second gradient reverses phase accumulations from the first for non-moving protons across the image (Le Bihan et al., 1986). The phases of water protons not diffusing are refocused and the observed signal is unchanged by the spatial gradients. Spins associated with diffusing water molecules, however, experience incomplete phase reversal because they move relative to the diffusion gradient, and therefore there is an observed signal attenuation related to the diffusion coefficient (Mukherjee et al., 2008). The amount of diffusion-weighting is prescribed by the gradient strength, time between gradient pulses, and duration of the gradients. These determine a numerical factor called the b value, representing the degree of diffusion weighting, and typically ranges from 800 to 2000 s/mm^2 (multiple b values may also be used). Diffusion-weighted sequences are typically based on spin echoes, utilize minimal TE to reduce T_2* effects, and are ordinarily acquired at isotropic spatial resolutions from 1-2 mm.

A series of measurements are acquired to quantify diffusion along oblique axes, and with sufficient directions, orientation distributions of diffusion are estimated (32-64 directions are often used for brain studies). Representations of diffusion vary from relatively straightforward parameters such as six-component tensors to sophisticated biophysical models representing crossing white matter fibers (Behrens et al., 2007). Diffusion tensor imaging is the most widely used approach, and decomposes 3D diffusion into orthogonal vectors representing diffusion along perpendicular axes.

From DTI analyses, several structurally relevant quantities can be derived (Kingsley, 2006). Fractional anisotropy measures tensor eccentricity, with greater anisotropy corresponding to orientationally constrained diffusion, such as along axons in white matter. Lower anisotropy is characteristic of regions with less constrained structure, as in gray matter or cerebrospinal fluid. Diffusivity is another important quantity, and measured in several ways, each reflecting specific tissue properties. Axial diffusivity (AD) a measure of diffusion along the axis of maximum molecular motion (i.e. the principal vector) is thought to reflect axon integrity; radial diffusivity (RD), diffusion perpendicular to the principal vector, is related to myelination of white matter bundles (Song et al., 2002).

Diffusion tractography

The diffusion-weighted MRI application most relevant to brain connectivity is tractography. This technique can non-invasively estimate white matter pathways, producing three-dimensional tract curves and allowing structural connectivity quantification. Tractography depends on the principle that water movement reflects spatial anisotropy in the underlying microstructure (Beaulieu, 2002). The basic principle of tractography is to computationally step along putative white matter tracks using the modeled diffusion at each point. Streamlines are generated by following the direction of preferential diffusion, moving a fixed distance, and iterating this process. Streamlines are seeded in a region-of-interest, and axonal fiber bundles are then modeled by the paths these streamlines follow.

There are two major approaches to diffusion tractography: deterministic and probabilistic. In the former, streamlines will rigidly follow the principal direction diffusion; in the latter, the orientation distribution function is randomly sampled, and rather than a unitary streamline, a set of likely of paths is created by repeating this process until a sufficient sample is generated, and calculating the proportion of streamlines reaching some endpoint or passing through a waypoint (Behrens et al., 2007). Both result in estimates of structural connectivity. As streamlines generally align with the underlying white matter, structural connectivity can be taken to represent the prevalence of inter-regional axonal connections, although this relationship is indirect.

Limitations of tractographic methods

Structural connectivity has several important methodological limitations. First, the challenge of resolving streamline orientations at regions of fiber crossing, or where separate axonal pathways run in parallel, has not been fully addressed. One approach is to use orientation distribution functions that permit multiple peaks of diffusion for a given voxel (Wedeen et al., 2008). However, even with multi-fiber models the issue of crossing pathways remains significant.

Further, the problem of false positives must be considered (Yamada, 2009). Tractography parameters should be chosen to reduce anatomically unlikely tracts, such as those with sharp bends and recursive loops. As with other noninvasive approaches, it is essential to interpret results in light of known anatomical information from sources such as postmortem tract tracing (Hein et al., 2016). It is imperative that structural connectivity not be interpreted as providing conclusive, direct evidence for the existence or non-existence of white matter tracts. Rather, tractographic data can better define connectivity between structures already known to have valid links, possibly supplemented by functional connectivity or separate observations from non-imaging approaches (Meola et al., 2016; Seehaus et al., 2013).

As with functional connectivity, the resulting numerical quantities should be understood in relative terms, e.g. connectivity between areas A and B is greater than between A and C. This is because some streamlines can be found between any two regions with sufficiently permissive thresholding. As with functional connectivity, which is not described in absolute units, structural connectivity is understood in statistical terms. Functional connectivity is quantified from the correlations of spontaneous activity between two areas; analogously, structural connectivity is described by the fraction of streamlines between areas. These quantities are unitless, and not necessarily in direct proportion to any single property of the underlying tissue, metabolic or microstructural. Rather, connectivity metrics should be conceptualized as useful but indirect stand-ins for the biological properties they depend on.

Relationships between structural and functional connectivity

Relationships between fMRI-based co-activation patterns and diffusion-based structural inferences are complex (Honey et al., 2009). Persistent coordinated activity does not strictly imply the presence of direct connections between cerebral regions; rather, functional linkage may be mediated by common structural pathways to a third area. The relationship between structural and functional connectivity is asymmetric: it is easier to infer functional connectivity from anatomical connectivity than the other way around. For instance, (Koch et al., 2002) used complementary fMRI and diffusion methods to study the motor cortex, and found the two measures to be correlated. However, they observed strong functional connectivity in the absence of tractographic connections, but not vice versa.

Nonetheless, it is possible to predict anatomical pathways from functional connectivity. For instance, in a landmark study, (Greicius et al., 2009) determined the existence of tractographic pathways connecting the nodes of the default mode network, which was previously described by functional correlation. The medial-prefrontal portion of the default mode network was shown to structurally connect with one subsection of the posterior cingulate/precuneus node, while the more inferior parts of the network were connected with a different sub-region of the same node. Thus, structural connectivity can confirm and refine conclusions drawn from functional connectivity.

Importantly, connectivity values from these modalities are continuous gradations rather than binary—for instance, to assert that two regions exhibit connectivity indicates that they meet a certain threshold for number of fibers or degree of synchronous activity. The continuous nature of connectivity allows structural-functional correlations to be determined. For instance, the degree of anisotropy in the white matter bundle connecting frontal and posterior default mode network is proportional to the partial correlation in these regions' fMRI signals, after accounting for signals from other connected regions-of-interest (Van Den Heuvel et al., 2009).

This continuous relationship is not limited to single white matter pathways or specific RSNs, but rather a significant correspondence across all gray matter voxels in the brain (Skudlarski et al., 2008). The same conclusion was reached in two ROI-based studies using whole-brain approaches: (Honey et al., 2009) and (Hagmann et al., 2008), in which graph theoretical analysis was performed on the signal correlations among regions across the whole cerebrum. Again, structural connectivity was a more reliable predictor of functional connectivity than vice versa. It is also important to consider that inconsistencies between functional and structural connectivity may result from either false-positive or false-negative results, such as functional connectivity artifacts due to head motion or spurious tractography due to insufficient modeling of crossing fibers (Damoiseaux and Greicius, 2009).

These methods are complementary, reflecting different aspects of the same biological systems. The truism that in the nervous system "what wires together fires together" is as applicable to macro-scale neuroimaging as to microscopic circuits: co-active brain networks are often linked by dense, coherent white matter pathways, and thus structural and functional connectivity are expected to support one another. Nonetheless, divergent results from these approaches do not necessarily indicate a deficiency in one method, but rather reflect their fundamentally different sources of information. When different connectivity techniques produce congruent results, it should be understood as a robust, though not conclusive, description of an underlying neural pathway.

1.3 Network dysfunction in neurological disorders of movement and cognition

These neuroimaging techniques can aid in the understanding of function and dysfunction in a variety of neurological conditions by revealing changes to key brain networks. This can offer insights into the mechanisms of symptomatology and progression of neuropathology.

Parkinson's disease

Parkinson's disease (PD) is a neurodegenerative movement disorder characterized by the death of dopaminergic neurons in the substantia nigra of the midbrain. PD is the second-most-common neurogenerative disorder, affecting approximately one percent of the population older than 60 years (NINDS, 2015), and results in reduced life expectancy, with a mortality ratio approximately twice that of the unaffected population (Poewe et al., 2008). Loss of the substantia nigra pars compacta results in dopamine insufficiency at the basal ganglia, particularly the caudate and putamen, which are the target of nigro-striatal projections, and the sites of dopamine release associated with motor feedback loops.

PD is a proteopathy characterized by the formation of cytoplasmic inclusions called Lewy bodies, which are comprised primarily of toxic aggregates of the protein alpha-synuclein. It is a disease of dopaminergic system degeneration, which causes both movement symptoms—tremor, rigidity, gait problems, postural instability, and slowed movement (bradykinesia)—and cognitive impairments, including reduced executive function, failure of abstract thinking, inattention, visuospatial difficulties, and working memory loss (Jankovic, 2008).

Dopamine insufficiency is treated using the precursor molecule L-DOPA, which is converted to dopamine by the enzyme dopamine decarboxylase, and in intransigent cases with dopamine agonists, which mimic the neurotransmitter by binding to its cell-surface receptors, particularly D_2/D_3-class receptors prevalent in mesostriatal brain areas (Murray et al., 1994). Dopamine in these circuits is essential for both movement and reward-motivated behavioral control, especially in the mesolimbic and mesocortical projections from the ventral tegmental area of the midbrain to the nucleus accumbens and frontal cortex, respectively (Ghahremani et al., 2012).

Although PD is identified symptomatically, its effects on brain structure and function can be examined using neuroimaging techniques including MRI and PET. A radioligand with binding affinity for the dopamine transporter (DAT) may aid in differentiating PD from other conditions. However, there is no definitive imaging test for PD diagnosis, which is frequently misidentified as related movement disorders such as progressive supranuclear palsy (PSP). Nonetheless, a variety of characteristic PD symptoms produce signature changes in structure (especially of the dopaminergic midbrain) and function identifiable by neuroimaging. Positron emission tomography (PET) reveals dopamine receptor changes associated with disease progression. D_2/D_3 receptor availability is extensively reduced in patients with PD compared to healthy controls, not only in the striatum, where these receptors are highly expressed (Antonini et al., 1997), but also in extrastriate regions including the locus coeruleus and the temporal lobes, where the function of dopamine remains largely unknown (Stark et al., 2018b).

MRI applications in PD

Various MRI contrasts provide information related to neurologic deficits in PD, especially in the midbrain. Changes in longitudinal relaxation rates due to iron deposition in the substantia nigra correlate with motor impairment (Gorell et al., 1995), and iron in the basal ganglia is also higher in PD patients than controls (Wallis et al., 2008), an effect evident in susceptibility-weighted MRI

(Gupta et al., 2010). Volumetric analysis of the diminished substantia nigra also shows promise as a discriminative method for PD, especially in combination with diffusion-based structural connectivity (Menke et al., 2009). The presence of the pigment neuromelanin in the substantia nigra also offers potential for PD diagnosis, as NM-containing structures are detectable using MRI sequences sensitive to magnetization transfer effects (Tambasco et al., 2016). Recently developed quantitative magnetization transfer methods may augment the description of progressive nigra and locus coeruleus degeneration (Trujillo et al., 2015). While these methods may reveal localized sites of neurodegeneration in PD, this disease must also be considered in terms of network dysfunction. Structural and functional connectivity may provide insights inaccessible to static measures of tissue integrity.

Functional connectivity abnormalities in PD have been extensively studied, providing information about dysfunction in dopaminergic networks of motor control (Tahmasian et al., 2015). These studies highlight the importance of dopamine replacement therapy in modulating network synchrony. Several seed-based functional connectivity studies have focused on the basal ganglia and subcortical structures. (Hacker et al., 2012) observed decreased connectivity in striato-thalamo-cortical loops and between the putamen and midbrain, pons, and cerebellum. A broader range of brain regions were examined in (Dubbelink et al., 2014), which found widespread network disruptions over three years compared to elderly healthy controls, including connectivity decreases correlated with cognitive decline. Studies have also examined how connectivity relates to altered cognition. For example, poor performance on the Stroop task and more severe PD symptoms correspond to disturbed connectivity of the caudate nucleus, putamen, globus pallidus, and thalamus, the major components of cortico-striatal feedback loops (Müller-Oehring et al., 2015).

Independent component analyses of resting fMRI data have also been reported in the literature. ICA revealed decreased connectivity in regions including the temporal lobes and the default mode network in PD, the latter correlating with cognitive scores (Tessitore et al., 2012). Symptom-modifying therapies may also restore functional linkage. Performance of computer-assisted cognitive training for PD patients improves brain connectivity, particularly the central executive network and an attentional network involving the superior parietal cortex (Cerasa et al., 2014).

The studies highlighted above were conducted while on dopamine replacement medication. This is a key consideration, as dopamine levels are major determining factors in both symptomatology and network function in the mesocorticolimbic pathways. Additional studies of PD effects have been conducted in an off-dopamine state, and merit separate consideration. Altered connectivity of the bilateral striatum was found in PD patients off dopamine replacement therapy, with posterior putamen connectivity to sensorimotor network, and increased anterior putamen connectivity to motor regions and parietal cortex (Helmich et al., 2010). Compared to healthy controls, another study found decreased putamen connectivity with cortico-striatal and mesolimbic circuits (Luo et al., 2014).

Circuit connectivity is likely related to dopamine receptor status. Striatal dopamine levels in the putamen as measured by PET are correlated with functional connectivity of that structure, suggesting that functional dynamics are responsive to neurotransmitters (Baik et al., 2014).

Amygdala functional connectivity has also been examined, though to a lesser extent. Connectivity between the whole amygdala (i.e. central and basolateral) and supplementary motor area is elevated in PD, implying that non-striatal limbic structures may also be affected in dopamine depletion, and suggesting that compensatory connectivity to motor-associated cortex may play a role in movement disorders (Yu et al., 2013). The major conclusions of the existing body of literature highlight the importance of altered linkage between the striatum and cerebral cortex, and the sensitivity of such changes to the pharmacology of dopamine replacement therapy.

Impulsive-compulsive behaviors (ICBs) are associated with dopaminergic therapy for PD, particularly the administration of non-ergot dopamine agonist drugs, which preferentially target D_2/D_3 receptors, with relatively high affinity for D_3. ICBs include binge eating, gambling addiction, compulsive shopping or hobby participation, and hypersexuality (Claassen et al., 2011; Voon et al., 2011; Weintraub et al., 2015). The common factor in ICBs is excessive participation in rewarding activities. Association of ICBs with artificially increased dopamine tone suggests activity changes in mesocorticolimbic pathways mediating addiction and reinforced learning. Specifically, they may involve dopamine projections between the ventral tegmental area of the midbrain, the ventral striatum, and limbic loops related to incentive salience and reward-motivated behavior (**Fig. 1-3B**). ICB-related changes in network connectivity are addressed in detail in Chapter 2.

Progressive supranuclear palsy and Parkinson-plus syndromes

Parkinson-plus syndromes refer to a cluster of neurodegenerative movement disorders with progressive clinical features similar to PD, but with additional and distinguishing symptoms and different underlying molecular pathologies. These diseases include progressive supranuclear palsy (PSP), corticobasal syndrome, and multiple systems atrophy. Parkinson-plus syndromes are either synucleinopathies like PD or tauopathies (characterized by accumulation of the protein tau) (Mark, 2001).

Progressive supranuclear palsy (PSP), also called Steele-Richardson-Olszewski Syndrome, is a Parkinson-plus syndrome that manifests with progressive impairments to movement and cognition. Over time, these result in disability and death, with a median survival less than 10 years (Golbe et al., 1988). Although its cause is unknown, PSP a neurodegenerative tauopathy, linked to a haplotype of the tau protein-encoding gene (Baker et al., 1999). PSP progression is characterized by tau aggregation (i.e. neurofibrillary tangles) in several brain regions, including the dentate nucleus of the cerebellum (Hauw et al., 1994; Williams et al., 2007).

The dentato-rubro-thalamic tract (DRTT) is a major pathway originating in the dentate nucleus and passing through the superior cerebellar peduncle (SCP) to reach the red nucleus, thalamus, and connecting with ascending pathways to the cerebral cortex (**Fig 1-3C**). The DRTT carries motor and nonmotor feedback signals from cerebellum to cortex. The dentate nucleus is the primary deep gray matter structure of the cerebellum and is marked by distinct pathophysiological processes in PSP. In addition to tau protein aggregation, the dentate nucleus undergoes grumose degeneration (accumulation of eosinophilic clusters), with microgliosis, demyelination, and axonal degeneration (Ishizawa et al., 2000).

Diffusion MRI studies have consistently identified PSP-related changes in DRTT microstructure. In this pathway, the dentate nucleus passes axons through the SCP, the main efferent white matter structure of the cerebellum. Compromised integrity of the SCP has been repeatedly linked to PSP progression: its diameter is reduced, with evidence of deterioration in diffusion-weighted MRI. White matter degeneration in the DRTT, together with evidence of dentate tauopathy, and motor, oculomotor, and visuospatial symptoms, imply that this tract plays a critical role in PSP. However, the effects of DRTT degeneration on functional connectivity of the dentate nucleus have not been directly characterized. In Chapter 3 we test the hypothesis that in PSP, pathological white matter microstructural changes to the DRTT correspond to reduced functional connectivity of the dentate nucleus. We hypothesize that the relationship between microstructure and DRTT connectivity is related to disease severity and progression, and therefore examine longitudinal trends in structural integrity, measured by diffusion-weighted imaging.

1.4 Summary

Imaging contrasts sensitive to hemodynamic activity, diffusion, and perfusion are a toolkit allowing inferences to be drawn about connectivity within and between brain regions, and to answer questions about the complex relationship between structure and function in a variety of neural networks. It is crucial to remember that while the flexibility of MRI permits a vast range of neuroimaging contrasts, each individual technique reflects specific but narrow physical or functional aspects of brain organization. This fact is especially relevant in disease processes where degeneration or dysfunction in isolated brain regions cause cascading pathological effects throughout the brain. For instance, the most readily observed neural phenotype in PD is degeneration of substantia nigra neurons; however, effects of this localized degeneration are systemic, with altered connectivity patterns in extended regions of cortex.

In this dissertation, we will investigate structural and functional connectivity both in specific networks and across the brain. **Fig 1-3** provides an overview of the major brain networks that will be examined. The aim of this work is to expand our knowledge of networks in both healthy function and in pathology. In Chapter 2, we will investigate the relevance of frontal limbic networks to aberrant reward-motivated behavior caused by medical management of PD. In Chapter

3, we will examine the major circuit linking the cerebellum with the cerebrum, and detail novel findings about the connectivity of a newly discovered branch of this pathway. We will also describe preliminary evidence suggesting that structure and function of this tract undergo parallel impairment in PSP. Chapter 4 will report an alternative approach to the identification of functional brain networks, which relies on dynamic perfusion signal in the brain's gray matter. Finally, in Chapter 5 this method will be applied to a longstanding question about the neuroanatomy of a key limbic region, the orbitofrontal cortex.

CHAPTER 2

MESOLIMBIC FUNCTION AND CONNECTIVITY IN PATIENTS WITH REWARD-BASED COMPULSIVE BEHAVIORS

2.1 Purpose

Functional connectivity can probe not only the architecture of co-active functional brain networks, but also the neural correlates of altered behavior and cognition in neuropsychological disorders. To understand the causes of reward-motivated behavior including pathologically altered activity, we examined the dopaminergic pathways of the limbic system in the context of exogenous dopamine replacement therapy. The goal of this study was to identify whether the brain's reward circuits have different functional connectivity in patients susceptible to atypical drug responding, and whether this predisposition is related to changes in reward-incentivized learning.

2.2 Summary

A subgroup of Parkinson's disease (PD) patients treated with dopaminergic therapy develop compulsive reward-driven behaviors, which can result in life-altering morbidity. The mesocorticolimbic dopamine network guides reward-motivated behavior; however, its role in this treatment-related behavioral phenotype is incompletely understood. Here, mesocorticolimbic network function in PD patients who develop impulsive and compulsive behaviors (ICB) in response to dopamine agonists was assessed using BOLD fMRI. The tested hypothesis was that network connectivity between the ventral striatum and the limbic cortex is elevated in patients with ICB and that reward-learning proficiency reflects the extent of mesocorticolimbic network connectivity. To evaluate this hypothesis, 3.0 T BOLD-fMRI was applied to measure baseline functional connectivity on and off dopamine agonist therapy in age and sex-matched PD patients with (n=19) or without (n=18) ICB. An incentive-based task was administered to a subset of patients (n=20) to quantify positively or negatively-reinforced learning. Whole-brain voxelwise analyses and region-of-interest-based mixed linear effects modeling were performed. Elevated ventral striatal connectivity to the anterior cingulate gyrus (p=0.013), orbitofrontal cortex (p=0.034), insula (p=0.044), putamen (p=0.014), globus pallidus (p<0.01), and thalamus (p=0.024) was observed in patients with ICB. A strong trend for elevated amygdala-to-midbrain connectivity was found in ICB patients on dopamine agonist. Ventral striatum-to-subgenual cingulate connectivity correlated with reward learning (p<0.01), but not with punishment-avoidance learning. These data indicate that PD-ICB patients have elevated network connectivity in the mesocorticolimbic network. Behaviorally, proficient reward-based learning is related to this enhanced limbic and ventral striatal connectivity.

2.3 Introduction

Motor symptoms in patients with Parkinson's disease (PD) improve with dopamine replacement therapy, but patients can develop debilitating reward-driven impulsive and compulsive behaviors (ICB). Dopamine agonist (DAA) use in particular is the greatest risk factor for this behavior, where prevalence estimates indicate approximately 15 percent of patients on DAA therapy develop these symptoms (Weintraub et al., 2015). Consequent maladaptive activities include hypersexuality, compulsive gambling, shopping, and binge eating (Perez-Lloret et al., 2011) (American Psychiatric Association, 2013).

Medication effects likely target the mesocorticolimbic incentive-learning network, an integrated system of cortical and subcortical structures in which the ventral striatum plays a central role (Haber and Behrens, 2014). More specifically, the ventral striatum receives dopaminergic projections from the ventral tegmental area of the midbrain, and mediates behavior-reinforcing effects of rewarding activities. Analogous to the nucleus accumbens in lower order species, the ventral striatum is important in motivation and reward-associative learning (Ikemoto and Panksepp, 1999; Olds and Milner, 1954) and is consistently implicated in drug addiction (Pierce and Kumaresan, 2006). Additionally, the amygdala, traditionally identified with associative learning involving fear or negative emotional valance, is a key mesolimbic structure. The amygdala encodes affective and motivational significance to rewarding events, mediates reward-learning (Tye et al., 2008), and interacts with the ventral striatum dopamine system to connect reward-association effects with behavior (Cador et al., 1989). While these structures have been studied extensively in the context of normal function and disease states, the behavioral outcomes of dopaminergic therapy for PD patients present a unique opportunity to investigate pathological activity in these networks, and related behavior, under differing pharmacologic conditions.

In this context, the effect of DAA-linked ICB on functional neural networks remains poorly understood. It is unclear why a subset of individuals receiving DAA therapy develop these altered behaviors. As DAAs show a preference for D_2-like receptors, which localize to the ventral striatum and mediate its activity (Claassen et al., 2017; Murray et al., 1994), altered connectivity within this region to other mesocorticolimbic structures may have relevance. We have previously shown that administration of DAAs to patients with ICBs results in a greater increase in cerebral blood flow to the ventral striatum than in the non-ICB population, indicating a greater metabolic response in this region (Claassen et al., 2017) (**Fig. 2-1**). A clearer understanding of circuits that may be altered in patients with these behaviors could inform better clinical practices to mitigate the impact of these side effects.

It is unknown whether DAAs produce ICB by directly reshaping brain connectivity, or by acting upon pre-existing group differences in network activity. Only one previous study examined striatal functional connectivity in PD-ICB patients (Carriere et al., 2015) and found functional disconnection in striato-cortical circuits. However, this study did not evaluate on and off

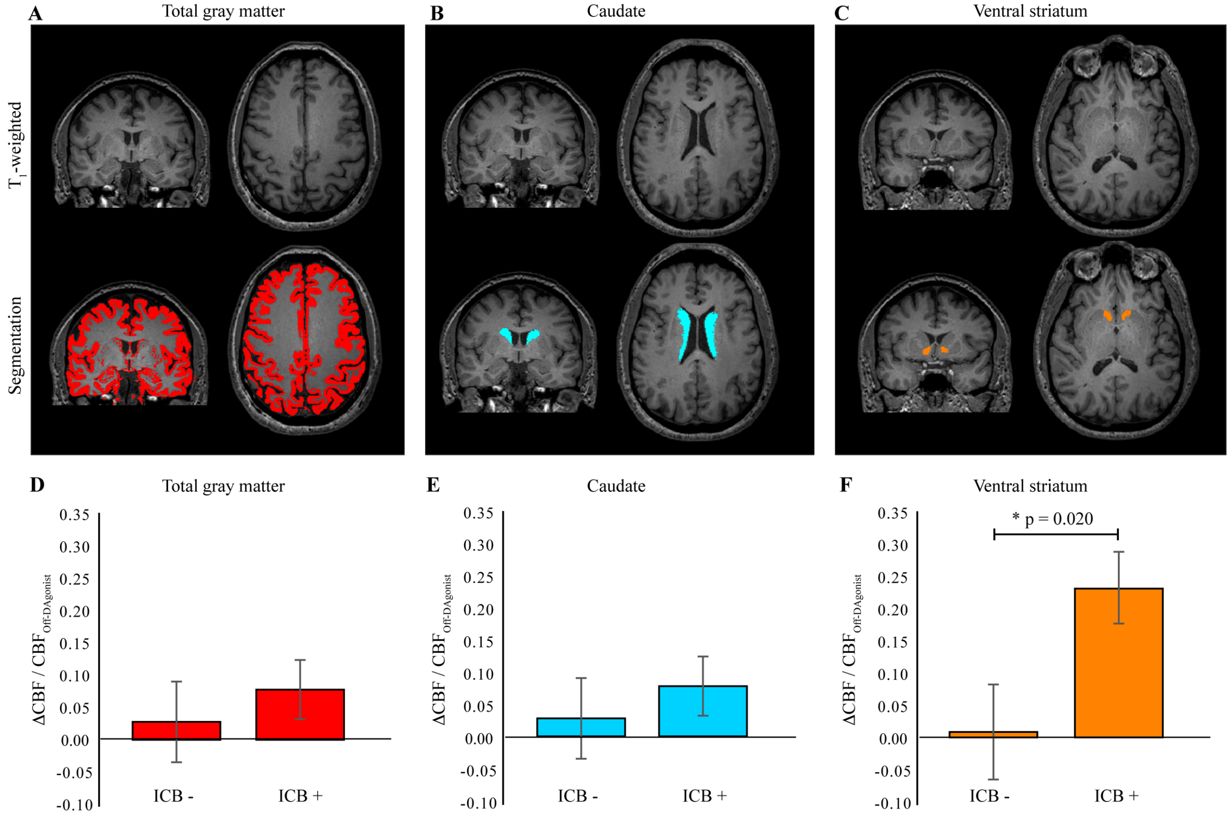

Fig. 2-1. Hemodynamic response to dopamine agonists is specific to the ventral striatum. Blood flow on and off DAA therapy was quantified in (A) all cortical gray matter, (B) subcortical nuclei including the caudate (shown here), putamen, amygdala, and thalamus, and (C) the ventral striatum/nucleus accumbens. The percent change in blood flow when resuming DAA administration after washout is not different between ICB+ and ICB- in total gray matter (D) or other subcortical regions-of-interest (E), but was significantly greater for ICB+ patients than ICB- patients in the ventral striatum (F) (Claassen, 2017).

medication states nor did it examine connectivity between subcortical structures (rather than exclusively between the basal ganglia and cortical surface) or include the amygdala.

As ICB manifestations are often categorized as behavioral addictions (Dagher and Robbins, 2009; Voon and Fox, 2007), we hypothesized that DAA-treated PD patients with this behavioral phenotype have increased functional connectivity between the ventral striatum and components of the limbic striato-pallido-thalamo-cortical loop, including pathways to the anterior cingulate gyrus and orbitofrontal cortex. To test this hypothesis, we applied pharmacological baseline blood oxygenation level-dependent (BOLD) fMRI to measure regional connectivity of the hemodynamic signal between the ventral striatum and mesocorticolimbic regions implicated in incentive salience, motivation, and addiction. Because amygdala activity has also been linked with reward-motivated behaviors (Hitchcott et al., 1997; Murray, 2007) on and off DAA, we additionally examined amygdala connectivity with reward network components. Finally, since striato-cortical networks are implicated in action choice and reward valuation (Bogacz and Gurney, 2007; Tanaka et al., 2004), we tested whether functional connectivity was linked to differences in incentive-based learning. To our knowledge, this is the first study to test ICB-related connectivity differences while modeling controlled on-DAA and off-dopaminergic medication states.

2.4 Methods

Patients with PD (n=37; gender=12F/25M; age=61.8±8.4 years) were recruited from the Vanderbilt University Movement Disorders Clinic and provided informed, written consent for this prospective study. Participants met the following inclusion criteria: no history of (1) non-PD-related neurological disease; (2) psychiatric disease including bipolar affective disorder, schizophrenia, or other condition known to compromise executive cognitive functions; (3)

moderate-to-severe depression, based on the Center for Epidemiological Studies Depression Scale-Revised; (4) medical conditions known to interfere with cognition (e.g., diabetes, pulmonary disease), and (5) confounding medical therapies such as antipsychotics or acetylcholinesterase inhibitors. All participants reported stable mood functioning, absence of major depression, and did not meet clinical criteria for mild cognitive impairment or dementia based on a neurological exam. Patients completed the Questionnaire for Impulsive-Compulsive Disorders in Parkinson's Disease-Rating Scale (QUIP-RS). To measure PD severity, a clinical examination was administered by a board-certified neurologist (D.O.C.). The Movement Disorders Society's United Parkinson's Disease Rating Scale (UPDRS) part II (Goetz et al., 2008) was used to assess self-reported disease severity. Patients' current prescribed dosages of dopaminergic medication, including Levodopa and DAAs, were converted to levodopa equivalent daily dosage (LEDD) (Tomlinson et al., 2010).

Patients were categorized as *ICB+* (n=19) or *ICB-* (n=18) according to previous methods (Weintraub, 2009) based on a structured behavioral interview with the patient and spouse. ICB+ patients were defined as those exhibiting one or more of the following behaviors that emerged after the initiation of DAA medication: compulsive eating, compulsive gambling, compulsive shopping, hypersexuality, and compulsive hobbyism. In this sample, most commonly encountered problematic behaviors were hypersexuality and compulsive eating; no patients exhibited compulsive gambling. ICB- patients served as the control group, since the object was to identify ICB-specific (rather than PD-specific) connectivity patterns.

Patients were required to refrain from taking all dopaminergic medications prior to the off-dopamine therapy scan (16 hours Levodopa-free, 36 hours DAA-free, due to differential drug kinetics) to reduce circulating drugs and abrogate residual drug effects. For the on-DAA scan, patients took their prescribed DAA dosage (but not levodopa) such that the clinical testing and exam were performed in the on-DAA-only state.

A subset of participants (n=8 *ICB+*; n=12 *ICB-*) completed an action-valence learning task, both on-DAA and off-dopamine. Participants were exposed to new stimuli in each visit, so each session required new learning. Stimulus order within each session was randomized. For a detailed description of the trials, see Van Wouwe *et al.*, 2017. Subjects were instructed that the goal of this task was to learn to act or withhold action in response to each of four cartoon characters to maximize earnings by gaining rewards (+25 cents) and avoiding losses (i.e., punishments, -25 cents).

Unbeknownst to the subjects, two of the cartoon characters provided outcomes that were rewarded or unrewarded, and the other two cartoon characters provided outcomes that were either punished or unpunished. Thus, the former two characters were associated with reward learning, whereas the latter two characters were associated with punishment avoidance learning. Also unknown to the subject, one character from each set of two produced the optimal outcome (i.e., either gain reward or avoid punishment) when the subject acted, but the other character from each set produced the optimal outcome when the subject withheld action.

This setup orthogonalized both reward/punishment valence and action/inaction. The optimal response was probabilistically rewarded (A and B), or not punished (C and D) 80% of the time, whereas the non-optimal response always yielded the undesired outcome (either no reward in A and B or a punishment in condition C and D). Subjects were unaware of the exact probabilities of each action-outcome association, but they were instructed that each action associated with a particular stimulus would lead to a particular outcome most of the time, but not always. Before the actual experiment, participants performed 15 practice trials during which they experienced the probabilistic nature of the task.

Subjects completed 160 learning trials, divided into four 40-trial blocks. Accuracy was defined by the percentage of trials in which the subject selected the optimal response. To confirm that participants learned throughout the task, performance across the four learning blocks was first analyzed. Subsequent analyses were performed on the final block, reflecting asymptotic maximum learning.

Scans were performed at 3 Tesla (3.0T) in separate on-DAA and off-dopamine conditions using a Philips Achieva scanner (Philips Healthcare, Best, the Netherlands) with body coil transmission and 8-channel SENSE array head coil reception. The multimodal imaging protocol included a standard T_1-weighted anatomical (3D MPRAGE; spatial resolution=1x1x1 mm^3; TR/TE=8.9/4.6 ms), T_2-weighted FLAIR (3D T_2-weighted turbo-spin-echo; spatial resolution=1x1x1 mm^3; TR/TI/TE=4000/2800/120 ms), and BOLD (spatial resolution=3.5x3.5x3.5 mm^3; single shot gradient echo planar imaging; TR/TE=2000/35 ms; flip angle=75°, duration=5 min). The BOLD field-of-view was 224 x 224 x 122.5 mm (matrix size = 64 x 64 x 35) and was oriented to have a 30° angle between the anterior commissure – posterior commissure line and the plane of the imaging volume (chosen to reduce the spatial extent of phase heterogeneity and signal dropout beyond lower frontal lobe voxels). The slice acquisition order was interleaved ascending.

Image pre-processing was performed using standard routines from the FMRIB software library (FSL) (Smith et al., 2004). The first three volumes of each scan were removed to ensure the signal was at steady-state, leaving 147 frames. Next, BOLD scans were motion-corrected by registration to the central frame, slice-time corrected, spatially smoothed with a Gaussian kernel (full-width-half-maximum (FWHM)=5 mm), and bandpass filtered to exclude frequencies below 0.01 Hz (scanner drift) and above 0.15 Hz (high-frequency nuisance fluctuations).

Next, to reduce contributions from residual motion and nuisance fluctuations, a conservative data-driven approach similar to COMPCOR (Behzadi et al., 2007) was applied. Here, FSL MELODIC was used to decompose the voxel-wise time courses into 25 independent components. Next, *fsl_regfilt* was applied to regress out components found to be artifactual using the following criteria (1) no resemblance to known functional networks, e.g. those described in (Smith et al., 2009) or (2) localization to the skull. Nuisance regressors were selected to remove a similar percentage of explained variance in all subjects and variance removed was similar between ICB groups (*ICB*+: 27.3%; *ICB*-: 25.2%; not significant in a two-tailed t-test).

Next, anatomical T_1-weighted images were skull-stripped and automatically segmented and seed regions in ventral striatum and amygdala were defined by FSL FIRST outputs (Patenaude et al., 2011) (**Fig. 2-2A**). All seed regions were bilateral. T_1-space masks were examined by a board-certified neurologist (D.O.C) and neuroradiologist (R.K.) to confirm

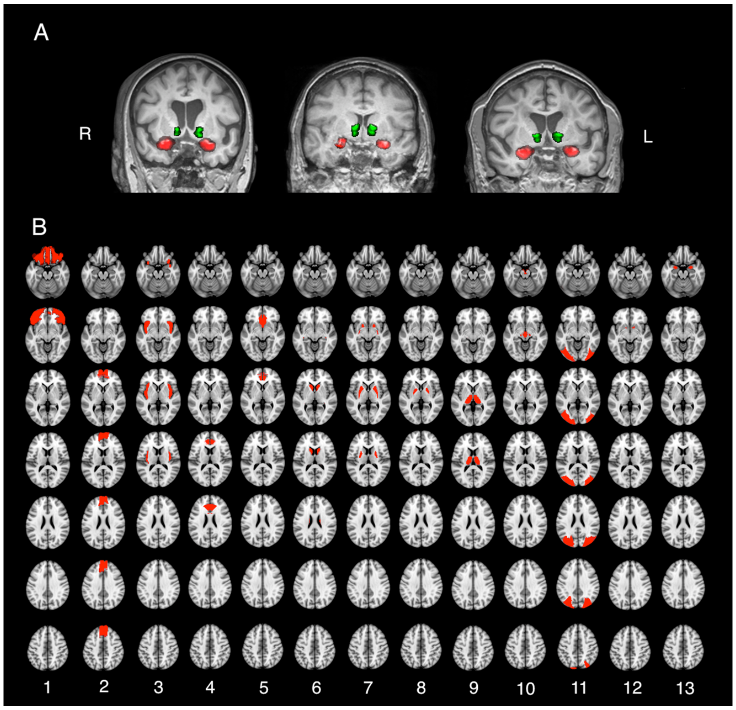

Fig. 2-2. Mesocorticolimbic regions-of-interest. (A) Representative seed regions determined by FSL-FIRST. Green=ventral striatum, red=amygdala. (B) All mesocorticolimbic ROIs used in group-level analysis. ROIs were defined using the IBASPM116 segmentation tool implemented in the WFU pick-atlas Matlab toolbox. Orbitofrontal cortex (1), ventromedial prefrontal cortex (2), insula (3), dorsal anterior cingulate gyrus (4), subgenual anterior cingulate (5), caudate (6), putamen (7), globus pallidus (8), thalamus (9), midbrain (10), occipital lobe (11), ventral striatum (12), and amygdala (13).

that the segmentation was representative of the structure. Seed region masks were then transformed to the BOLD scans and used to extract the seed time courses from the pre-processed BOLD images. This procedure was used to reduce confounds in which time courses are modified as a result of co-registration and resampling. The use of subject-derived seed masks reduces confounding partial volume effects due to variability in shape, size, and relative position of brain structures that are difficult to account for when using standard space atlases, but are common in older patients with neurodegeneration (Cherubini et al., 2009; Zhang et al., 2014).

Next, subject-level connectivity modeling was performed using FSL-FEAT. Seed time courses were used as explanatory variables in a voxelwise linear regression in native space. Each voxel's z-statistic was calculated using Fisher's z-transform. Subject-level connectivity maps were registered to native T_1 space and subsequently to the 2-mm Montreal Neurological Institute (MNI) 152 standard brain atlas. These MNI-space connectivity z-statistic maps were then used as inputs in a group-level analysis.

To determine whether regions outside of the mesocorticolimbic network are differently connected with the ventral striatum or amygdala in ICB patients, a group-level analysis was performed using voxelwise statistics in standard space using Statistical Parametric Mapping (SPM), with familywise error rate correction for multiple comparisons. Explanatory variables were ICB status (+/-) and drug status (on-DAA/off-dopamine). Age was treated as a covariate of no interest.

Image pre-processing for the ROI-based analysis was identical to methods in voxelwise analysis, except in two respects. First, a smaller spatial smoothing kernel was applied (FWHM=3 mm), as the ROI-based approach did not require as high a signal-to-noise ratio, and the goal was to avoid partial volume effects between the ventral striatum and lateral ventricles. 3-5 mm spatial smoothing is used routinely in fMRI analyses. Secondly, global signal regression was used rather than data-driven denoising in this analysis to ensure that voxelwise results were not due to bias in the selection of noise components. To extract global signal, whole-brain masks were created using FSL BET applied to the motion-corrected fMRI image. Global signal was then included as an additional regressor of no interest to account for residual motion effects and spatially non-specific physiological noise.

ROI-based connectivity analysis was performed using a mixed-effects linear model implemented in R Statistical Software version 3.3.2 (Foundation for Statistical Computing). Explanatory variables were ICB status (+/-), drug status (on-DAA/off-dopamine), and drug-ICB interaction. Twelve target ROIs were tested, as motivated by our study hypotheses: orbitofrontal cortex, ventromedial prefrontal cortex, insula, dorsal anterior cingulate gyrus, subgenual anterior cingulate gyrus (inferior to the genu of the corpus callosum), caudate, putamen, globus pallidus, thalamus, midbrain (ventral tegmental area and substantia nigra), occipital lobe (negative control), and ventral striatum (for the amygdala seed) or amygdala (for the ventral striatum seed) (**Fig. 2-2B**). ROIs were defined using the Wake Forest University pick-atlas tool Individual Brain Atlases using Statistical Parametric Mapping Software (IBASPM)-116 definitions (Maldjian, 1994). All target ROIs were bilateral.

Continuous measurements of patient demographics (**Table 1**) were compared between groups using the Mann-Whitney *U* test. Hypothesis 1, that ICB+ individuals would exhibit increased ventral striatal connectivity with reward network components while on DAA, was tested using both a voxelwise analysis with familywise error rate correction and an ROI-based approach with false discovery rate (FDR) correction. For the ROI analysis, a mixed-effects linear model was employed since the assumption of independence in a general linear model was violated by repeated measurements (on- and off-drug scans). Connectivity differences were considered significant at

Variable	PD ICB-	PD ICB+	*p*-value
N	18	19	
Gender (Male/Female)	13/5	12/7	
Age (years)	62.7±10.1	61.0±7.1	0.56
Disease Duration (years)	6.1±4.5	6.2±3.7	0.91
CES-D	15.1±7.2	17.4±11.2	0.46
MDS-UPDRS Part II	23.2±7.7	22.3±9.6	0.75
QUIP-RS Total	18.9±11.1	35.9±9.7	<0.001*
ICB Symptom Distribution			
Hobbyism	0/19	12/19	
Eating	0/19	13/19	
Sex	0/19	12/19	
Shopping	0/19	4/19	
Gambling	0/19	0/19	
Dopamine Replacement Therapy			
Total LEDD (mg/day)	609.8±390.3	639.1±417.1	0.82
Agonist Single Dose Equivalent (mg/day)	103.9±65.1	117.6±73.7	0.47

Table 1. Parkinson's disease group demographics, behavioral and cognitive traits. Values reported as mean +/- one standard deviation or fractions of subjects. *Meets significance criteria of two-sided p<0.05.

FDR=0.10, a threshold recommended by Benjamini (Benjamini and Hochberg, 1995; Genovese et al., 2002). The voxelwise parametric analysis was performed using multiple regression with ICB group and drug status as covariates of interest, and age as a covariate of no interest. Voxels were thresholded at $p<0.001$. Clusters were considered significant at family-wise error corrected $p<0.05$.

To test Hypothesis 2, that while on-DAA, ICB+ patients exhibit elevated reward-based learning, but not punishment avoidance-based learning, a mixed ANOVA was performed, with three within-subject factors; Action (action, inaction), Valence (reward, punishment avoidance), Medication (on-DAA, off-dopamine); and one between-subjects factor, Group (ICB+, ICB-).

To test Hypothesis 3, that ventral striatal connectivity relates to incentive learning, ventral striatal connectivity values with mesocorticolimbic ROIs were used as independent variables in least absolute shrinkage and selection operator (LASSO) regressions, where task score was the dependent variable. LASSO regression performs variable selection to determine what covariates are important in explaining the dependent variable, setting less-important terms to zero (Tibshirani, 1996). This analysis was collapsed across drug status, since the goal was to compare connectivity and reward learning independent of drug effects. LASSO regression was performed using the glmnet package (Friedman et al., 2010) and bootstrapped in R. LASSO regression was performed with two different datasets: reward vs. ventral striatum connectivity, and punishment vs. ventral striatum connectivity. In each regression, ICB status was included as a non-penalized explanatory variable (i.e. controlled for). The LASSO regression was performed on 500 bootstrap samples per condition, and the number of times each seed-target pair was chosen reported. Seed-target pairs were considered *highly important* if they were chosen in 80 percent or more bootstraps. For any seed-target pairs thus categorized, Spearman's ρ was calculated.

2.5 Results

Demographics

Table 1 summarizes non-imaging study values. *ICB+* and *ICB-* groups were matched ($p>0.05$) for age, disease severity (UPDRS part II), depression (CES-D), disease duration, and dosage (LEDD or DAA single dose equivalent). QUIP-RS was significantly greater for *ICB+* patients after correction for multiple comparisons ($p<0.001$).

Hypothesis 1: network connectivity in PD-ICB

The voxelwise analysis and ROI-based analysis yielded largely consistent results. In the voxelwise approach, we found increased ventral striatal connectivity with two significant clusters in ICB+

patients. Cluster 1 extended from the right thalamus through the basal ganglia (esp. globus pallidus and putamen) into the subgenual anterior cingulate gyrus as well as lateral orbitofrontal and dorsolateral prefrontal cortex. Cluster 2 mirrored cluster 1 in the left prefrontal cortex (**Fig. 2-3**).

In the ROI-based analysis, the ventral striatum of ICB+ patients exhibited increased connectivity with dorsal anterior cingulate gyrus (p=0.013), orbitofrontal cortex (p=0.034), insula (p=0.044), putamen (p=0.014), globus pallidus (p<0.01), and thalamus (p=0.024) (all reported p-values significant after FDR correction) (**Fig. 2-4A**). No main effect was observed for drug. An ICB-drug interaction effect between the amygdala and the midbrain was observed, such that off-dopamine, ICB+ status is associated with *decreased* connectivity, but on-DAA, ICB+ status is associated with *increased* connectivity. This effect was individually significant, but was not significant after FDR correction (p=0.011) (**Fig. 2-4B**).

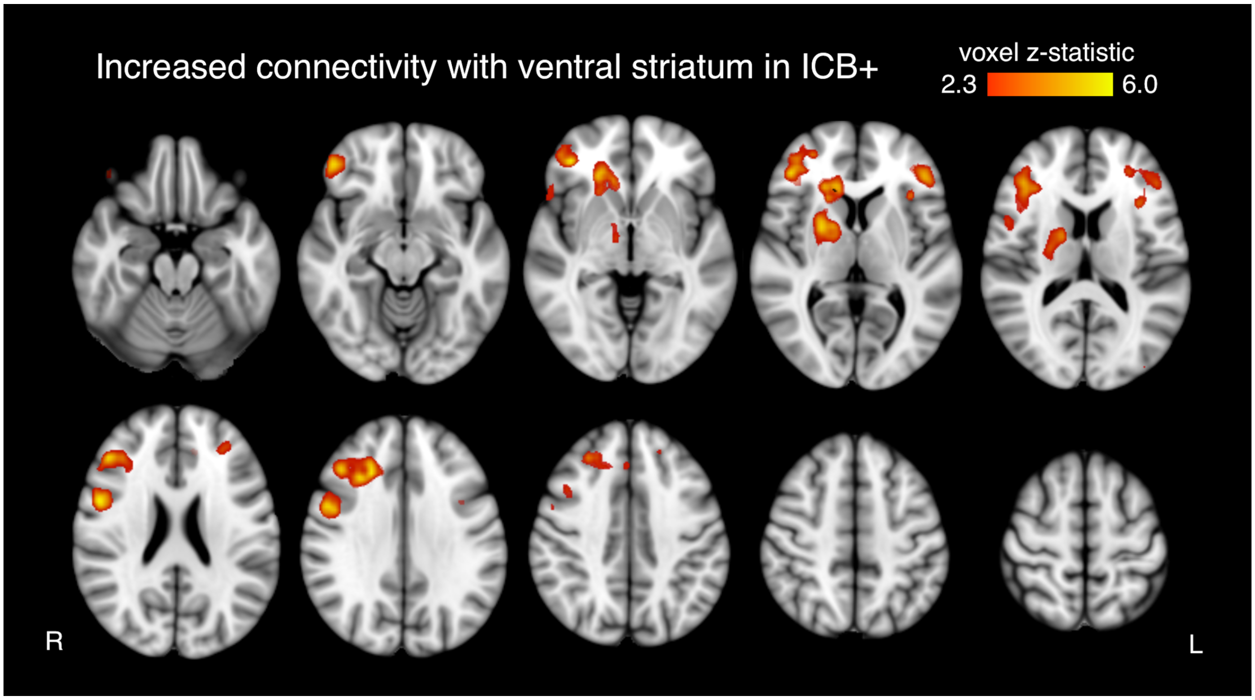

Fig. 2-3: Effects of impulsive and compulsive behaviors on voxelwise connectivity. Ventral striatum connectivity between ICB groups. No DAA effect was observed. Only clusters significant after family-wise error correction are shown.

Hypothesis 2: incentive learning

All patients showed an increase in learning across blocks, both on- and off-medication (off-dopamine, p<0.001; on-DAA, p<0.002). Learning proficiency was higher on average in ICB+ patients (91% correct responses) than in ICB- patients (79%) (p<0.01). There were no significant main effects of Medication or Action, nor any significant interaction between these two factors. Based on our hypothesis that ICB+ patients will particularly excel at learning from rewards, we compared reward and punishment learning (across medication states and action-learning conditions) separately between ICB groups. Reward learning was more proficient (p<0.01) in ICB+ patients (90%) compared to the ICB- patients (73%). ICB+ patients also tended to be more proficient on punishment avoidance learning (93%) than the ICB- patients

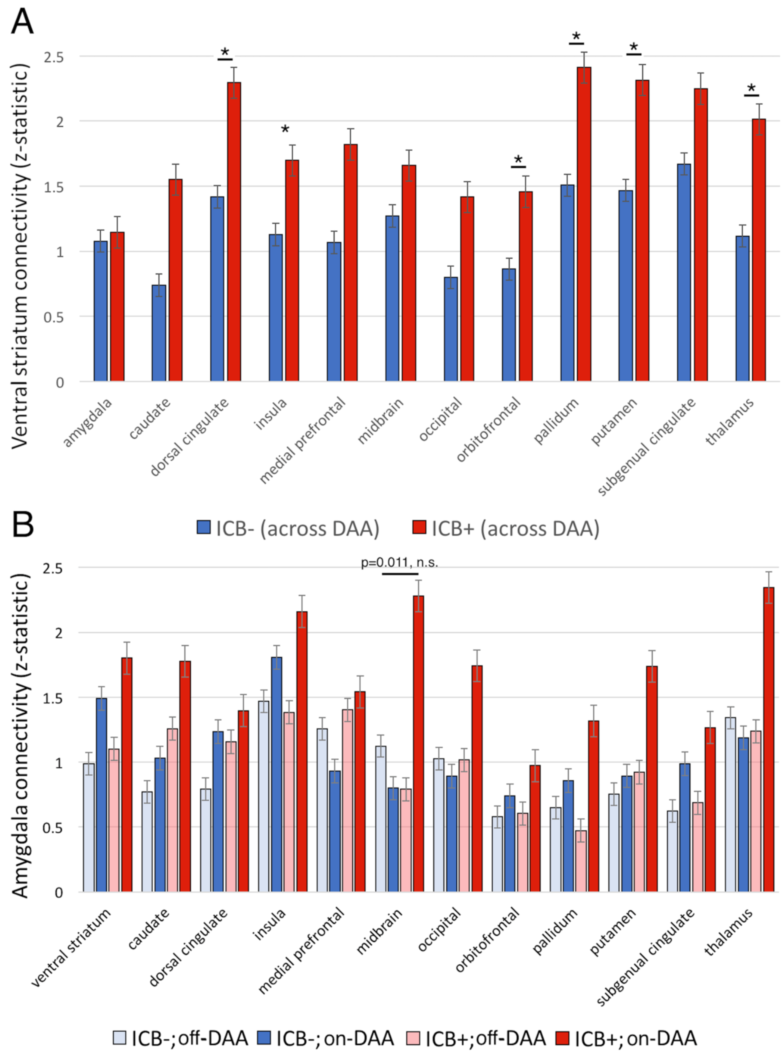

Fig. 2-4: Effects of impulsive and compulsive behaviors on ROI-based connectivity. Connectivity differences between ICB and DAA groups. (A): Ventral striatum connectivity between ICB groups. No DAA effect was observed. Asterisk indicates seed-target pairs significant after multiple comparisons correction. (B): Amygdala connectivity among ICB groups and drug states. Bar with p-value represents a DAA-ICB interaction effect not significant after multiple comparisons correction. Error bars represent standard error of the mean. These data support the idea of increased connectivity in cortico-striatal circuits involving the ventral striatum.

(84%), but this did not meet significance criteria (p=0.07).

	Subgenual anterior cingulate	**Occipital cortex**	**Insula**	**Midbrain**	**Dorsal anterior cingulate**
Reward learning	91.0†	63.2	54	53	25.2
Punishment learning	30.8	5.8	4.4	22.8	1.8
	Putamen	**Amygdala**	**Pallidum**	**Orbitofrontal cortex**	**Ventromedial prefrontal cortex**
Reward learning	16.6	10.4	0.4	0.2	0.2
Punishment learning	1.2	5.4	5.8	63.8	4.4

Table 2. Incentive learning and connectivity regression results. Values represent the percentage of bootstrapped LASSO regressions in which connectivity between ventral striatum and the given ROI was chosen as important for explaining reward or punishment learning. The regression was collapsed across drug states, and controlled for impulse control disorder. Results exceeding 80 percent are indicated with (†).

Hypothesis 3: network connectivity and incentive learning

Ventral striatum connectivity was tested for a relationship with incentive learning. This analysis controlled for ICB status, since learning scores were different between ICB groups. For reward score, ventral striatum to subgenual cingulate was highly important, chosen in the LASSO regression in 91% of bootstrapped samples. Ventral striatum to subgenual anterior cingulate connectivity was positively correlated with reward learning performance ($\rho=0.43$, $p<0.01$). No other seed-target connectivity pair exceeded the 80% threshold, nor did any regions exceed this threshold for punishment avoidance. **Table 2** summarizes LASSO regression results.

2.6 Discussion

In this study, we asked: *are mesocorticolimbic networks altered in patients with medication-induced impulse control disorder?* We used baseline fMRI to test for altered brain connectivity in impulsive and compulsive individuals and found heightened connectivity between the ventral striatum and the limbic loop to the anterior cingulate gyrus and orbitofrontal cortex, as well as to other limbic structures. We found evidence in support of the strength of this connection relating to reward-based learning.

Altered striato-cortical connectivity is associated with an array of behavioral disorders involving impulse control problems including cocaine addiction (Hu et al., 2015) and obsessive-compulsive disorder (Beucke et al., 2013; Menzies et al., 2008). Such connectivity is known to be dopamine-sensitive (Cole et al., 2013). Thus, we hypothesized that impulsive PD patients would exhibit altered limbic connectivity, especially while on-DAA. The ventral striatum is the target of the mesolimbic pathway classically implicated in incentivized behavior, response to reward cues, and reward-based learning (Ikemoto and Panksepp, 1999; Olds and Milner, 1954). DAAs can alleviate motor impairment in PD patients by mimicking endogenous dopamine effects on the dorsal striatum. However, exogenous dopamine also activates the ventral striatum, modifying reward and behavioral circuit activity, including striatal feedback loops serving non-motor cortical regions (Cools et al., 2007, 2001). The involvement of the ventral striatum in ICB is substantiated by our finding of increased cerebral blood flow to this structure in ICB+ patients (Claassen et al., 2017).

Carriere *et al.*, 2015, observed altered striato-cortical connectivity in PD-related ICB; however, they identified ICB-related functional disconnection only in the dorsal striatum, especially the putamen. Our results build on these studies and demonstrate the importance of increased ventral striatum connectivity as a correlate and potential driver of ICB. The difference in these findings may be due to the prior study’s inclusion of the ventral caudate and putamen in the ventral striatum seed region, rather than the nucleus accumbens alone, as in our study.

Surprisingly, our analysis did not indicate a DAA effect on ventral striatum connectivity. It is thus possible that DAAs act upon pre-existing group differences in connectivity. Alternatively, the absence of a direct drug effect may suggest that the impact of DAA on functional connectivity persists during the 36-hour drug washout we employed. Future studies with longer off-dopamine periods may resolve this question. Our results nonetheless reveal that elevated connectivity in striatal-limbic cortex pathways reflects enhanced incentive-based learning and impulse control problems.

Parts of the anterior cingulate gyrus and orbitofrontal cortex participate in a cortico-striatal-pallido-thalamo-cortical loop, one of a series of parallel feedback pathways between the cortex and striatum (Alexander et al., 1986) (**Fig. 2-5A**). Unlike other cortical areas which connect via

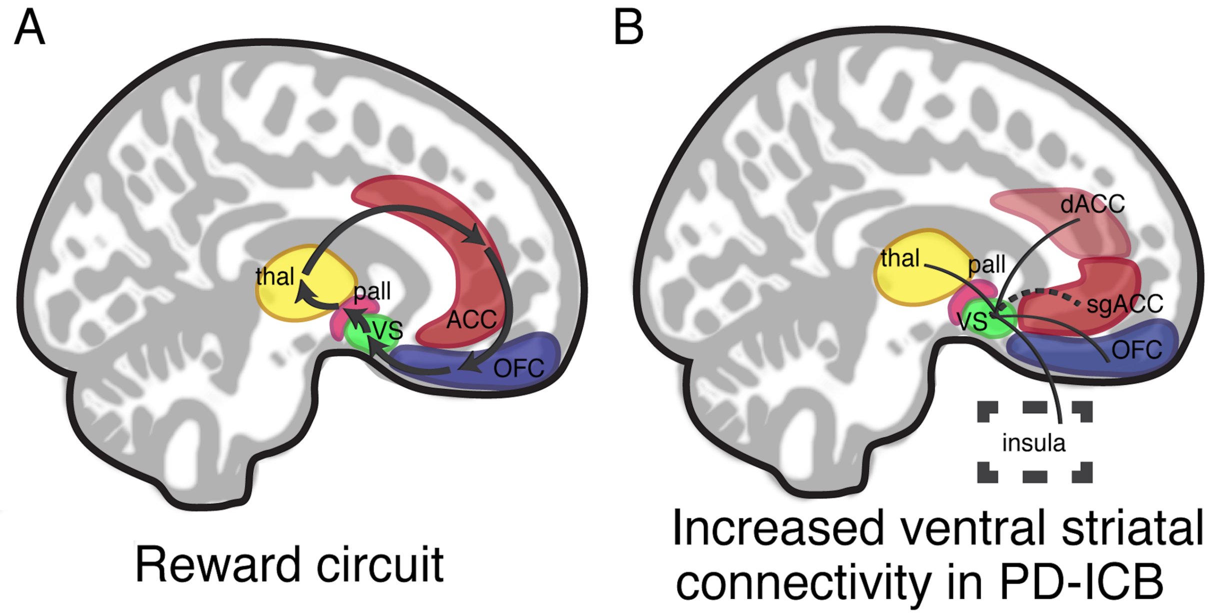

Fig. 2-5: Schematic representation of ICB-related network changes. (A) The limbic or affective striato-pallido-thalamo-cortical loop. Arrows represent anatomical connections as described in Alexander, 1986. The loop consists of the ventral striatum (green), the globus pallidus (magenta), the thalamus (yellow), and limbic cortical structures such as the orbitofrontal cortex (blue) and anterior cingulate gyrus (red). We propose that this structural and functional network is involved in incentive valuation and reward-driven behavioral modification. (B) Increased functional connectivity correlates of ICB. Bands indicate select regions of significantly increased connectivity, generally corresponding to the cortico-striatal-pallido-thalamo-cortical loop, which is highly connective in ICB+ PD individuals. Dashed connecting line between ventral striatum and subgenual ACC represents functional connectivity related to reward-incentivized learning.

the caudate or putamen, the limbic loop between the basal ganglia and the limbic cortex passes through ventral, rather than dorsal, striatum. Johansen-Berg *et al.* (2008) used diffusion tensor tractography to evaluate structural connectivity between the nucleus accumbens and the anterior cingulate. Our findings are consistent with functional connectivity between these regions reflecting positively reinforced learning in humans.

Since the ventral striatum-anterior cingulate network is more synchronous in individuals with ICB, and ICB involves heightened sensitivity to reward outcomes and more proficient learning, this suggests a mechanism whereby DAA medication may influence the development of problematic reinforced behaviors. The anterior cingulate is involved in decision-making and outcome evaluation (Bush et al., 2000), and its activity is modulated by expected reward (Amiez et al., 2005). Moreover, in primates, it has been implicated not only in reward valuation and decision-making (Shima and Tanji, 1998), but in reward learning (Hadland et al., 2003).

Similarly, activity of the orbitofrontal cortex has been linked to both cued and uncued impulsive choices (Zeeb et al., 2010). Along with the cingulate cortex, it contributes to reward valuation processes, and may mediate hedonic experiences (Kringelbach, 2005; Dolan, 2007). An important caveat is that the orbitofrontal cortex is prone to signal dropout and geometric distortion in long echo time gradient echo sequences due to its proximity to the sinuses (Deichmann et al., 2002); this effect can produce spurious results due to signal dropout. The insula is also associated with decision-making and risk evaluation (Bossaerts, 2010; Clark et al., 2008), and is activated when taking risks, especially when the gamble is successful (Xue et al., 2010).

Our results show a pattern of ventral striatal functional involvement with cortical areas known to affect action choice when outcomes are uncertain but potentially rewarding or reinforcing. Based on these data, we propose a model in which DAAs activate ventral striatum

$D_{2/3}$ receptor-bearing neurons, leading to increased connectivity in feedback pathways between the ventral striatum and limbic cortex (**Fig. 2-5B**). This, in turn, intensifies reward-learning behavior, leading to decision-making that is highly reward-sensitive and hedonic.

It is important to avoid drawing overly detailed mechanistic conclusions from functional connectivity studies, especially in striatal networks, where inhibitory and excitatory stop-and-go circuits function in parallel in the same space. However, the relationship between the limbic loop and reward-learning argues that our functional connectivity findings mirror basic neuropsychological processes which may help explain the singular behavior of individuals with ICBs.

The amygdala, like other limbic system components, has been repeatedly linked to reward-guided learning (Murray, 2007), and one study showed that its effects on reward-based learning vary with the application of D_3 agonist (Hitchcott et al., 1997). The amygdala receives dopaminergic connections from the midbrain (Hyman et al., 2009), and functional and structural connectivity between the two regions has been implicated in feedback-guided learning (M. X. Cohen et al., 2008). Unexpectedly, we found a strong trend toward increased connectivity between these regions in ICB, but only when on-DAA. This indicates a second limbic substrate upon which DAAs may act to promote impulsivity. Further studies are needed to identify how striato-cortical and amygdala-midbrain networks differ in their contributions to impulse control problems.

These findings should also be considered in the context of several limitations. While this study was powered to examine differences in ICB phenotypic groups, it is possible that drug effects on ventral striatal connectivity might be revealed by a larger sample size. A future study might also examine potential network differences between more risk-related ICB manifestations such as gambling (our study did not include any problem gamblers) and more hedonic variants such as binge eating. Additionally, the performance of the incentive-learning task was limited to a subset of patients (n=20) outside of the scanner. The task was designed to limit the impact of between-session learning by several means, including practice sessions to ensure task familiarity on both study days, and new reward-stimulus associations on the second day to prevent a cumulative learning effect. Nonetheless, we cannot rule out the possibility of some inter-session learning unrelated to drug or ICB group.

Another possible limitation of the incentive-learning task is the observation that ICB patients trended toward superior punishment avoidance-learning as well as reward-learning. This suggests that they may be more learning-proficient in general, although we note that punishment-based learning was not found to be strongly related to reward circuit connectivity. Future studies that use a task-based fMRI paradigm may provide insights into acute activity changes experienced by impulsive and compulsive drug-responders when evaluating potential outcomes of risky choices, and adapting behavior to seek rewards. Finally, only BOLD connectivity patterns are reported here, which provide insights with regard to network connectivity differences but limited information on underlying mechanisms. Ongoing work is focused on understanding these findings in the context of dopamine availability and ^{18}F PET studies, cerebral blood flow CBF using arterial spin labeling MRI (Claassen et al., 2017), and neurotransmission using magnetic resonance spectroscopy.

2.7 Conclusions

These results illustrate important relationships between reward circuits, D_2-like agonists, and behavioral phenotypes in PD. The findings of enhanced connectivity in the striato-pallido-thalamo-cortical network in patients with compulsive reward-driven behaviors has long been biologically suspected, but we can now localize an anatomic network to defined behavioral changes in PD patients. The relationship between connectivity of the ventral striatum and anterior cingulate with improved incentive learning provides important clinical relevance to BOLD findings. Furthermore, the finding that DAA therapy may augment amygdala to midbrain connectivity emphasizes that these key regions, the ventral striatum, cingulate cortex, and amygdala, act together in concert to regulate reward-driven behaviors, where alterations to these connected regions may fundamentally change an individual's ability to regulate comportment.

CHAPTER 3

STRUCTURE-FUNCTION RELATIONSHIP OF THE DENTATO-RUBRO-THALAMIC TRACT

3.1 Purpose

While functional connectivity is a potent tool to examine the dynamic activity of brain networks in behavior and neurological conditions, examination of structural connectivity enables more precision in the identification of specific white matter pathways. This is especially important in a surgical context, where localization of key pathways may prevent both unnecessary tissue damage and erroneous placement of electrical leads. Here, we utilize complementary structural and functional relationships to examine the detailed neuroanatomy of a critical pathway linking the cerebellum and cerebrum.

3.2 Summary

The dentato-rubro-thalamic tract (DRTT) regulates motor control, connecting the cerebellum to the thalamus. This tract is modulated by deep-brain stimulation in the surgical treatment of medically refractory tremor, especially in essential tremor, where high-frequency stimulation of the thalamus can improve symptoms. The DRTT is classically described as a decussating pathway, ascending to the contralateral thalamus. However, the existence of a nondecussating (i.e. ipsilateral) DRTT in humans was recently demonstrated, and these tracts are arranged in distinct regions of the superior cerebellar peduncle. We hypothesized that the ipsilateral DRTT is connected to specific thalamic nuclei and therefore may have unique functional relevance. The goals of this

study were to confirm the presence of the decussating and nondecussating DRTT pathways, identify thalamic termination zones of each tract, and compare whether structural connectivity findings agree with functional connectivity. Diffusion-weighted imaging was used to perform probabilistic tractography of the decussating and nondecussating DRTT in young healthy subjects from the Human Connectome Project (n=91) scanned using multi-shell diffusion-weighted imaging (270 directions; TR/TE=5500/89 ms; spatial resolution=1.25 mm isotropic). To define thalamic anatomical landmarks, a segmentation procedure based on the Morel Atlas was employed, and DRTT targeting was quantified based on the proportion of streamlines arriving at each nucleus. In parallel, functional connectivity analysis was performed using resting-state functional MRI (TR/TE=720/33 ms; spatial resolution=2 mm isotropic). It was found that the decussating and nondecussating DRTTs have significantly different thalamic endpoints, with the former preferentially targeting relatively anterior and lateral thalamic nuclei, and the latter connected to more posterior and medial nuclei ($p<0.001$). Functional and structural connectivity measures were found to be significantly correlated ($r=0.45$, $p=0.031$). These findings provide new insight into pathways through which unilateral cerebellum can exert bilateral influence on movement and raise questions about the functional implications of ipsilateral cerebellar efferents.

3.3 Introduction

The dentato-rubro-thalamic tract (DRTT) links cerebellar efferents with white matter tracts ascending from the thalamus to the motor cortex, premotor cortex (Middleton and Strick, 1998), and supplementary motor area (Wiesendanger and Wiesendanger, 1985), where they regulate fine movement. The DRTT is one of the major outflow pathways of the cerebellum. It originates in the dentate nucleus, a major gray matter deep cerebellar structure, passes through the superior cerebellar peduncle, decussates in the midbrain and contacts the contralateral red nucleus. From the red nucleus, the DRTT ascends to the thalamus, and connects to the ventral intermediate nucleus, where it synapses with neurons ascending to the cortex.

The classically described DRTT is a decussating pathway (d-DRTT); however, recent work applying deterministic fiber tractography in healthy subjects and human brain microdissection has shown the existence of an ipsilateral or nondecussating DRTT (nd-DRTT) (Meola et al., 2016). The discovery of uncrossed fibers in humans is an important advance in cerebellar anatomy. While primate (Wiesendanger and Wiesendanger, 1985), rodent (Aumann and Horne, 1996), and feline (Flood and Jansen, 1966) anatomical studies have demonstrated the existence of some non-crossing fibers from the dentate nucleus to the ipsilateral cortex, the nd-DRTT in humans remains virtually unstudied.

To ascertain the function of this pathway, it is essential to better characterize its structure. Meola *et al.* noted that the d-DRTT and nd-DRTT occupied different portions of their shared white matter bundles, with the nd-DRTT following a more dorsal trajectory in the superior cerebellar peduncle (SCP). This finding suggests that spatial segregation of the pathways may extend beyond the peduncle and into the thalamus. The thalamus is a dense and anatomically complex structure containing numerous white and gray matter sub-regions. In such a heterogeneous area, it is critical to know precisely which thalamic loci serve which cerebellar motor circuits.

Dysfunction of the DRTT is implicated in the emergence of tremor, which thalamic-targeted deep-brain stimulation can ameliorate. Clinical correlates of DRTT impairment include essential tremor, the most common adult movement disorder, Parkinson’s disease (Alesch et al., 1995), multiple sclerosis (Torres et al., 2010), and progressive supranuclear palsy (Surova et al., 2015). For electrode-placement surgery, diffusion tractography can preoperatively define the thalamic endpoint of the DRTT (Coenen et al., 2014, 2011; Fenoy and Schiess, 2017), and successful DRTT stimulation is associated with improved motor outcomes (Schlaier et al., 2015). However, previous studies employing tractography measures have focused exclusively on the d-DRTT (e.g. Kwon *et al.*, 2011; Anthofer *et al.*, 2014), even though unilateral cerebellar activity exerts bilateral effects on movement and cortical activity (Amrani et al., 1996; Cho et al., 2012; Cui et al., 2000; Immisch et al., 2003; Küper et al., 2012).

The conservation of the nd-DRTT across mammalian taxa suggests an unknown functional role for this pathway, perhaps in the coordination of bilateral movements, or as a compensatory system for movement after unilateral cerebellar damage. To identify the nd-DRTT's functional role, its subcortical anatomy must first be defined in greater detail. Thus, we examined its thalamic connectivity in comparison to the d-DRTT. We utilized 1.25-mm-resolution multi-shell diffusion-weighted magnetic resonance imaging (MRI) data from the Human Connectome Project (HCP) to identify thalamic nuclei that are preferentially targeted by the d-DRTT and nd-DRTT. To test whether functional connectivity between the cerebellar dentate nuclei and their ipsilateral and contralateral thalamic targets reflects d-DRTT and nd-DRTT structure, we utilized baseline (resting-state) blood oxygenation level-dependent (BOLD) functional MRI (fMRI) to quantify functional connectivity both ipsilaterally and contralaterally in the same cohort of healthy subjects.

3.4 Methods

Imaging

HCP data for healthy subjects were obtained from the WU-Minn consortium 500 subjects release (Van Essen et al., 2013) (n=91; age=29.3±3.3 years; sex=54 F, 38 M). HCP diffusion-weighted brain images were acquired at 3.0 Tesla in a Siemens Skyra scanner. HCP images were acquired using 2D echo-planar readout with 270 directions (TR/TE=5500/89 ms; spatial resolution=1.25 mm isotropic). A multishell diffusion scheme was used with b-values of 1000, 2000, and 3000 sec/mm^2 (Sotiropoulos et al., 2013; Uğurbil et al., 2013). Scan time was approximately 55 minutes. Resting-state BOLD fMRI scans were acquired (TR/TE=720/33 ms; 1200 volumes; spatial resolution=2 mm isotropic) (Smith et al., 2013) in the same volunteers.

Image processing

Diffusion and functional images were pre-processed by the Human Connectome Project according to the procedures described in (Glasser et al., 2013). As part of the pre-processing pipeline, diffusion data were corrected for motion, echo planar imaging distortion, and eddy currents. fMRI pre-processing included distortion correction, motion correction, intensity normalization, and registration of fMRI series to Montreal Neurological Institute (MNI) 2-mm standard space. Subsequent image processing and analysis were performed using the FMRIB software library (FSL) (FMRIB, Oxford, UK) and custom Matlab scripts. We brain-extracted the pre-processed diffusion images with the 'BET' utility with fractional intensity threshold set to 0.3 (Smith, 2002). T_1- and T_2-weighted images were also brain-extracted using 'BET.' Fractional anisotropy (FA) values were calculated from the diffusion images, b-values, and b-vectors using the 'dtifit' tool.

To reduce contribution from cardiac and respiratory signals in fMRI, as well as random high-frequency fluctuations, we also applied high-pass and low-pass temporal filtering to exclude frequencies outside the 0.01-0.15 Hz range. fMRI data were spatially smoothed using a Gaussian kernel with a full-width-half-maximum of 5 mm.

Tractographic seed and waypoint regions for all subjects were hand-drawn excepting the thalami, which were automatically segmented, and inspected by a board-certified neurologist (DOC). The dentate nucleus was drawn on FA images in the coronal view, identified as a hypointensity in local FA values, representing a gray matter region surrounded by white matter, approximately 15 mm from the midline, lateral and posterior to the fourth ventricle. The superior cerebellar peduncle waypoint masks were drawn in single coronal slices on the FA maps, while the red nucleus was defined in axial T_2-weighted images as the hypointense ellipsoid area in the medial brainstem. The gross thalamus was segmented in native T_1 space using FSL-'FIRST' (Patenaude et al., 2011). All regions were drawn or segmented bilaterally.

Intrathalamic segmentation was carried out with a novel statistical shape model method constructed using high-field (7.0T) MR images from 9 healthy volunteers (Liu et al., 2015). The inputs to the thalamic shape model are the whole thalamus, previously segmented by 'FIRST,' and a known correspondence between the native T_1 space and the shape model space, which was generated by a combination of rigid (Maes et al., 1997) and nonrigid (Rohde et al., 2003) registration. The final segmentation results are 23 distinct intrathalamic nuclei on each hemisphere in the native T_1 image space. An example of thalamic segmentation is shown in **Fig. 3-1**. Further comment on the validity and accuracy of this method can be found in section 3.6.

T_1-weighted images were linearly registered to diffusion space using FSL's 'flirt' tool with 12 degrees of freedom (Jenkinson et al., 2002). The inverses of the resultant affine matrices were used to transform thalamus and red nucleus masks to diffusion space. T_1-weighted images were also non-linearly registered to the 2-mm MNI-152 brain using FSL's 'fnirt' tool, and warp parameters preserved.

The DRTT was defined by probabilistic fiber tractography with FSL's diffusion toolbox 'Fdt' (Behrens et al., 2007, 2003), which allows multiple fibers per voxel, permitting robust detection of crossing fibers. Probabilistic tractography was utilized in lieu of deterministic tractography since the goal was to build a quantitative distribution of fiber endpoints in the thalamus rather than to find a single small zone of maximum connectivity. First, diffusion parameters at each voxel were modeled using 'bedpostx,' which builds up a distribution of diffusion directions at each voxel using Bayesian estimation. Then, fiber-tracking was performed with 'probtrackx2.' Four tracts were defined per subject: left d-DRTT (i.e. originating in left dentate and terminating in right thalamus), right d-DRTT, left nd-DRTT, right nd-DRTT. The

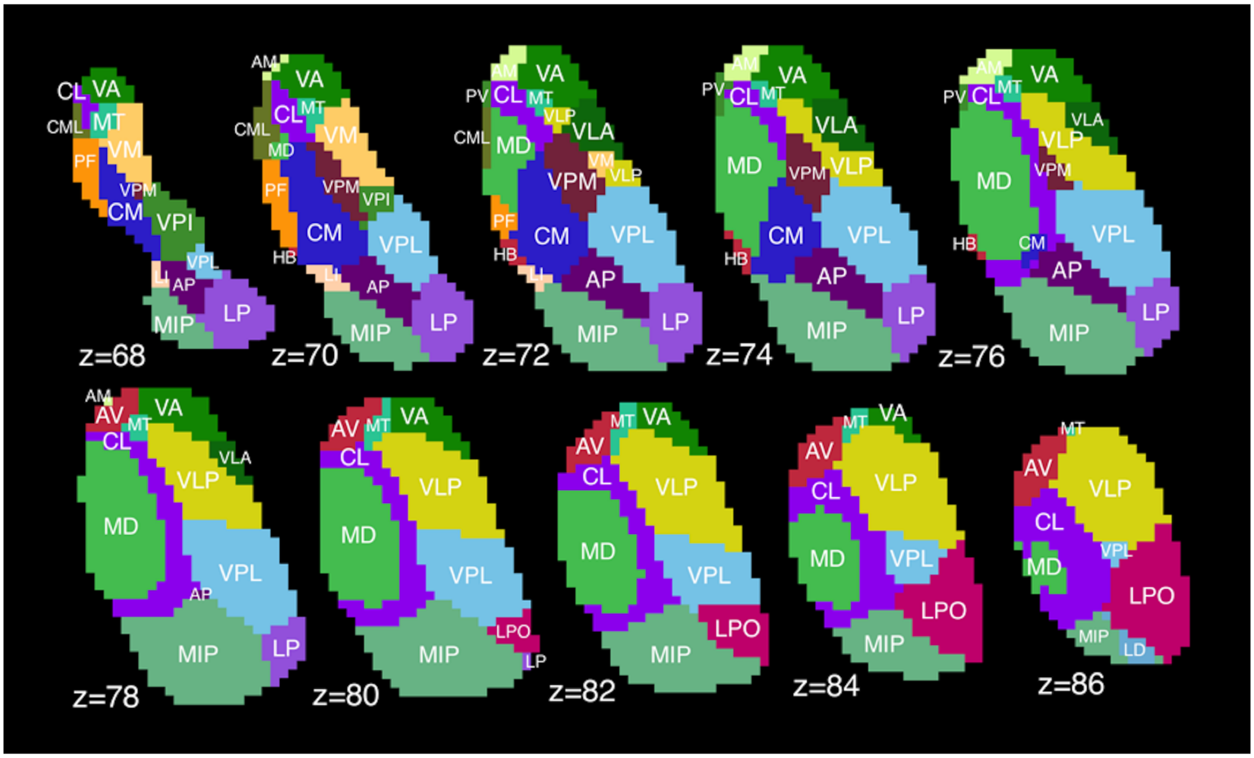

Fig. 3-1. Thalamic segmentation. Example of thalamic sub-segmentation using shape-fitting model based on Morel atlas. Displayed in MNI-1mm space; z represents slice number, not millimeters. VA=ventral anterior, CL=central lateral, MT=mammillothalmic tract, PF=parafascicular nucleus, CM=centromedian, VPM=ventral posterior medial, VPI=ventral posterior inferior, LI=limitans, AP=anterior pulvinar, VPL=ventral posterior lateral, MIP=medial+inferior pulvinar, LP=lateral pulvinar, AM=anteromedial, CML=central medial, HB=habenular, MD=mediodorsal, VLP=ventral lateral posterior, VLA=ventral lateral anterior, AV=anteroventral, LPO=lateral posterior, LD=lateral dorsal, PV=paraventricular, VM=ventral medial.

dentate nuclei served as the seed regions, with the SCP, red nucleus, and thalamus as sequential forced-order waypoints. Step length was set at 0.5 mm with a maximum of 320 steps per fiber (this value was empirically determined as sufficient for both d-DRTT and nd-DRTT to reach the thalamus). No curvature threshold was set, since the presence of three waypoint masks was sufficient to exclude any streamlines deviating from the main track. 5000 streamlines were calculated per tract, per subject. Track maps were then registered to subject T_1 space, and then to MNI space, using the affine transformation matrix and then the warp coefficients generated from structural image registration.

For each MNI-space track-map, a thalamic center-of-gravity measure was calculated to estimate the locus of maximum connectivity for each tract. Center-of-gravity measures for d-DRTT and nd-DRTT were obtained by weighting all intra-thalamic voxels by the number of streamlines passing through each, and computing a weighted mean, thus producing a single Cartesian point, per subject, representing the 'center' of d-DRTT or nd-DRTT structural connectivity. These computations were performed on MNI-space-transformed tracks for spatial comparability.

Structural connectivity

Mapping structural connectivity to thalamic nuclei was performed in subject T_1-weighted space. Because more streamlines completed tracking for the nd-DRTT than the d-DRTT, likely due to hindrance by crossing fibers in the d-DRTT, statistical analysis was performed on the percentage of the total streamlines arriving at each thalamic nucleus rather than the absolute number of streamlines. Because thalamic nuclei differed in size, percentage structural connectivity was adjusted proportionally to size of the target nucleus. A custom Matlab script was used to calculate the adjusted percentage for each thalamic nucleus; this measure defined structural connectivity. Left and right structural connectivity values were averaged, as laterality was not of interest. Nuclei accounting for 5% or more of the total structural connectivity with the d-DRTT, nd-DRTT, or both were considered to have high structural connectivity. This threshold was chosen because the median structural connectivity accounted for by a given nucleus was 1.9% and 1.2% for d-DRTT and nd-DRTT, respectively (see Results), and hence nuclei with 5% or higher had structural connectivity several times greater than the typical value. Finally, for each thalamic nucleus, we calculated the ratio of d-DRTT structural connectivity to nd-DRTT structural connectivity, a quotient we term structural d/nd ratio. A ratio above 1 indicates that a greater proportion of decussating fibers contact a given nucleus, while a ratio below 1 indicates the opposite. For instance, a nucleus in which a typical voxel received 12% of d-DRTT streamlines and 6% of nd-DRTT streamlines would have a structural d/nd ratio of 2.0.

Functional connectivity

All functional connectivity analysis was performed in standard space. Time courses were extracted from the left and right dentate nuclei, which were defined in MNI space using a probabilistic atlas available in FSL (Diedrichsen et al., 2011). These time courses were then used as inputs in subject-level connectivity modeling using FSL-fMRI Expert Analysis Tool ('FEAT'), in which the activity at each brain voxel is fit to the dentate nucleus time course. Voxelwise group-level functional connectivity was assessed with a 1-sample t-test using FSL's randomise function. Thalamic voxels with mean functional connectivity values (i.e. temporal correlations with the dentate timeseries) greater than 0.3 or less than -0.3 were included in group-level analysis, and t-statistics reported. We employed this threshold to eliminate weak correlations, similar to the approach in (Long et al., 2016). To assign functional connectivity according to the thalamic shape atlas, z-statistics for each nucleus were calculated using the Fisher transform. Functional d/nd ratio was defined for each of the 23 nuclei by dividing the d-DRTT z-statistic by the nd-DRTT z-statistic.

Statistics and hypothesis testing

The major hypothesis was that the d-DRTT and nd-DRTT differ in thalamic connectivity. This hypothesis was tested by comparing thalamic centers of gravity between d-DRTT and nd-DRTT. Center-of-gravity x- and y-coordinates in MNI space for the d-DRTT and nd-DRTT were compared using two-tailed t-tests, and p-values reported. To compare structural connectivity for each of 23 thalamic nuclei, we used a two-tailed, paired Student's t-test to assess whether d-DRTT connectivity was significantly different from nd-DRTT connectivity. Resultant p-values were then corrected for multiple comparisons using false discovery rate (FDR)<0.05 (Benjamini and Hochberg, 1995). Only p-values significant after FDR correction are reported. Structural and functional d/nd values were compared across the 23 nuclei using a Spearman's correlation.

3.5 Results

Structural connectivity

Probabilistic tractography for the d-DRTT and nd-DRTT was successful in all subjects, in that at least some fibers completed tracking from the dentate to the thalamus. 54.5% more streamlines completed tracking from dentate to thalamus for the mean nd-DRTT than the mean d-DRTT.

Fig. 3-2 depicts both pathways in axial slices, as well as in a three-dimensional streamline representation. **Fig. 3-2B** was generated using Diffusion Toolkit and TrackVis (Cui et al., 2000).

The nd-DRTT structural centers-of-gravity were more posterior in the thalamus than the d-DRTT by an average of 1.8 mm in MNI space ($p<0.001$), and more medial by 2.42 mm ($p<0.001$). (**Table 3**).

8 of 23 thalamic nuclei examined exhibited high structural connectivity with either d-DRTT, nd-DRTT, or both. These were: centromedian, parafascicular, ventral anterior, ventral lateral anterior, ventral medial, ventral posterior lateral, ventral posterior medial, and ventral posterior inferior. Of these 8 nuclei, all exhibited statistically significant biases in d/nd ratio, either toward the d-DRTT (4/8; ventral anterior, ventral lateral anterior, ventromedial, and ventral posterior inferior), or nd-DRTT (4/8; centromedian, parafascicular, ventral posterior lateral, and ventral posterior medial) ($p<0.001$ for all) (**Fig. 3-3**).

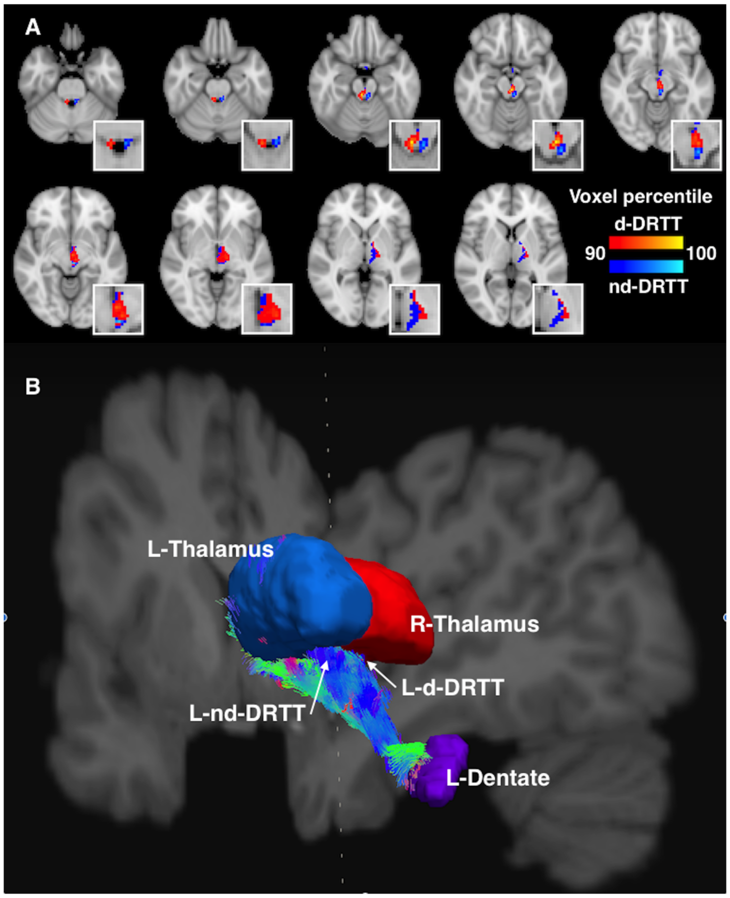

Fig. 3-2. The decussating and nondecussating DRTTs. (A) Axial slices showing the d-DRTT (red) and nd-DRTT (blue), thresholded to include the top 10% of nonzero voxels by structural connectivity for each tract. For clarity, only the DRTT tracks arriving at the left thalamus (i.e. right decussating and left nondecussating tracts) are depicted. Figure has been up-sampled to 0.5mm isotropic resolution for better visualization clarity. Insets are enlargements of the same axial slices. (B) A 3-dimensional visualization of the DRTT pathways originating in the left dentate nucleus and arriving at the ipsilateral (blue) and contralateral (red) thalamus. View is from the posterior aspect, with coronal and saggital slices of T_1-weighted image shown for reference. Streamline coloration is based on fiber orientation, where blue is superior-inferior, green is anterior-posterior, and red is left-right, per convention.

	Center-of-gravity of structural connectivity values in thalamus		
	X	Y	Z
d-DRTT (l)	37.6	56.4	35.1
d-DRTT (r)	51.9	55.8	35.1
nd-DRTT (l)	50.9	55.0	35.2
nd-DRTT (r)	38.9	55.4	35.1
d-DRTT mean	n/a	56.1	35.1
nd-DRTT mean	n/a	55.2	35.2
d- minus nd-*	1.2 voxels	0.9 voxels	0.1 voxels
mm difference	2.4 mm	1.8 mm	0.2 mm
p-value	<0.001	<0.001	n.s.

Table 3. Thalamic mean centers of gravity for DRTT tractography in 2-mm MNI space. *Note: because x coordinates reflect left or right thalamus position, rather than location within the thalamus, x-coordinates were compared by distance from the midline (medial-lateral), rather than by absolute x-coordinate.

These values are first reported unilaterally for left and right tracts, then for the mean of left and right. Next, the difference in x, y, and z coordinates between the two tracts is reported in voxels and mm. Finally, p-values from two-tailed t-tests are reported.

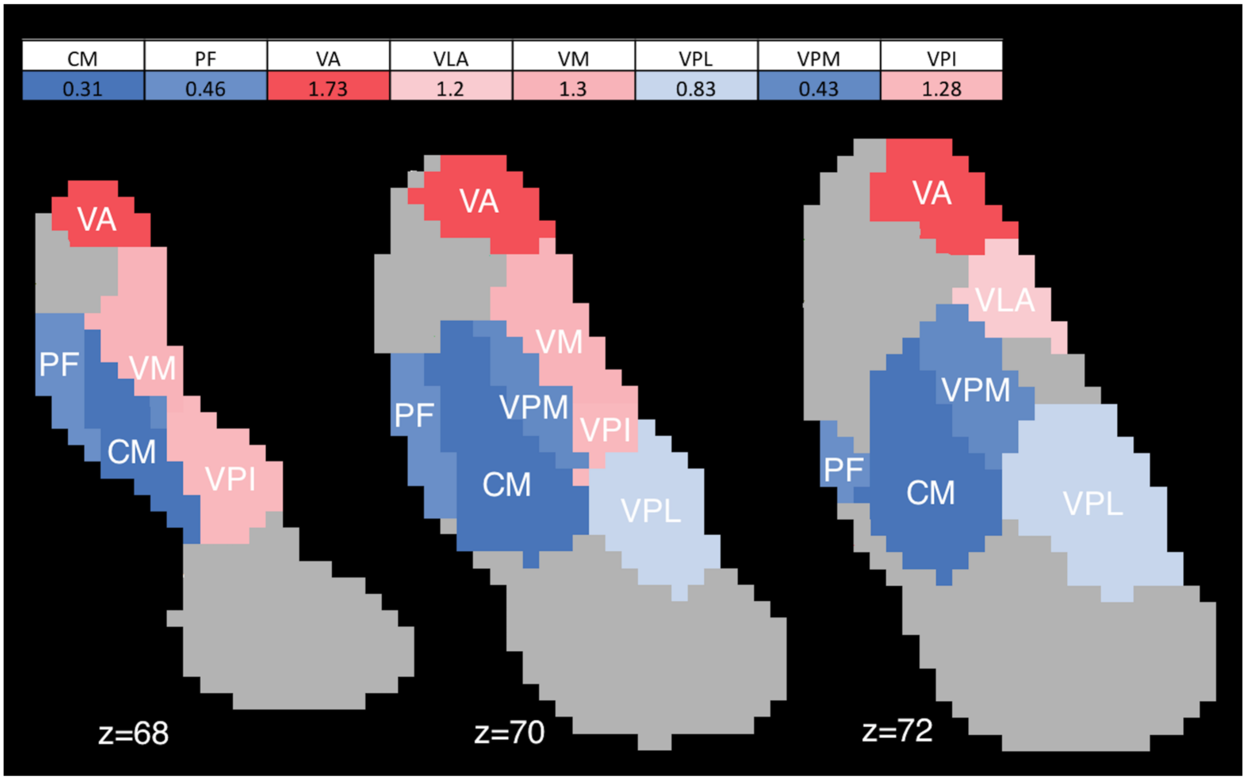

Fig. 3-3. DRTT thalamic structural connectivity. Map of structural d/nd ratios for thalamic nuclei with high (>5%) structural connectivity, and significant bias towards d-DRTT or nd-DRTT, in 1-mm MNI space. Blue indicates bias toward nd-DRTT, red indicates bias toward d-DRTT**.** Color intensity corresponds to degree of bias. Abbreviations: CM=centromedian; PF=parafascicular; VA=ventral anterior; VLA=ventral lateral anterior; VM=ventral medial; VPL=ventral posterior lateral; VPM=ventral posterior medial; VPI=ventral posterior inferior. These results represent a connectivity difference between d-DRTT and nd-DRTT, although they also include a substantial amount of overlap between the two thalamic termini.

Functional connectivity

Within the thalamus, significant functional connectivity with the dentate nucleus occurred in a distinctive band which traversed the medial aspect of the bilateral thalami, regardless of ipsilateral or contralateral dentate seeding (**Fig. 3-4**). While the functional connectivity did not display the same clear anterior/posterior bifurcation between d-DRTT and nd-DRTT targeting as did structural connectivity, there was a statistically significant correlation between structural d/nd ratio and functional d/nd ratio across the 23 nuclei (Spearman's ρ=0.45, p=0.031) (**Fig. 3-5**), which indicates that for cerebello-thalamic connectivity, structural and functional measures independently confirm d-DRTT and nd-DRTT patterns of thalamic targeting. One nucleus (ventral posterior inferior) was an outlier for functional d/nd ratio according to Grubbs' test, and was omitted from this analysis; however, its inclusion or exclusion did not affect the statistical significance of the relationship.

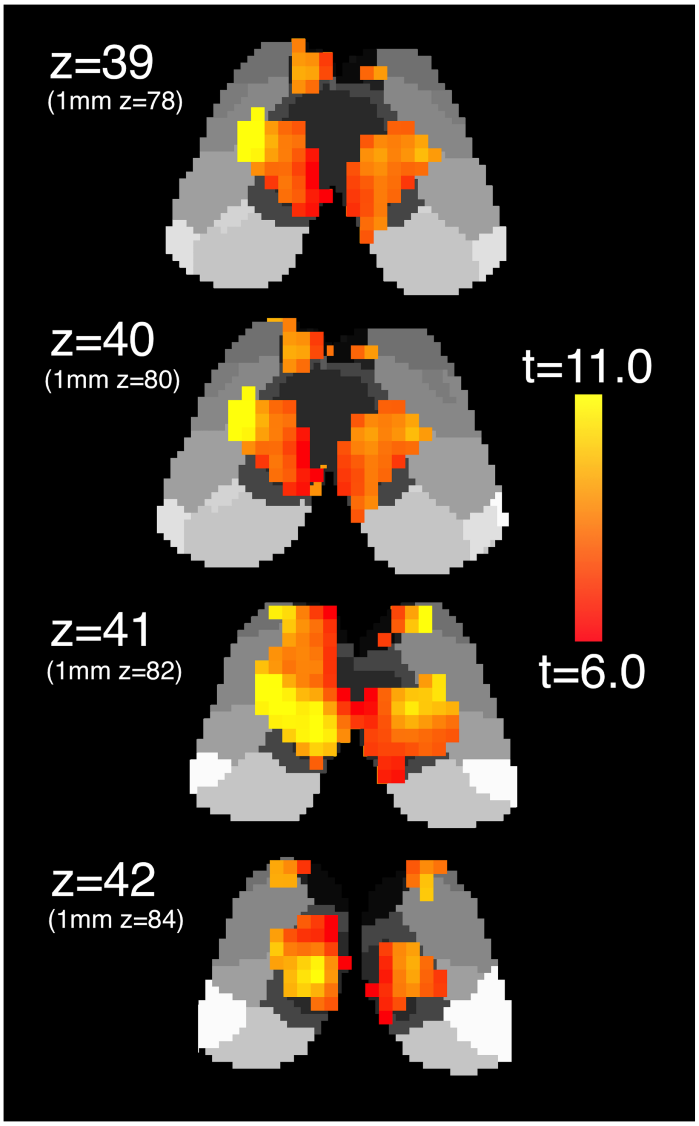

Fig. 3-4. Dentato-thalamic functional connectivity. Voxelwise functional connectivity of the unilateral dentate nucleus with bilateral thalamus in 2-mm MNI space. Left dentate connectivity displayed. 1-mm MNI equivalent z-slices listed in parentheses for comparison with Figs. 3-1 and 3-2.

3.6 Discussion

We have shown that the decussating and nondecussating DRTT pathways connect to distinct regions of the thalamus, and linked these to probable thalamic nuclei. The nd-DRTT sends a greater proportion of its fibers to regions which are more posterior and medial than the classical d-DRTT, suggesting that these two pathways may participate in discrete cerebello-cerebral circuits. This finding was reinforced by the identification of a strong positive relationship with functional connectivity measurements. These results are consistent with the idea of separable cerebellar "output channels" performing different functions in parallel (Middleton and Strick, 1998). Further

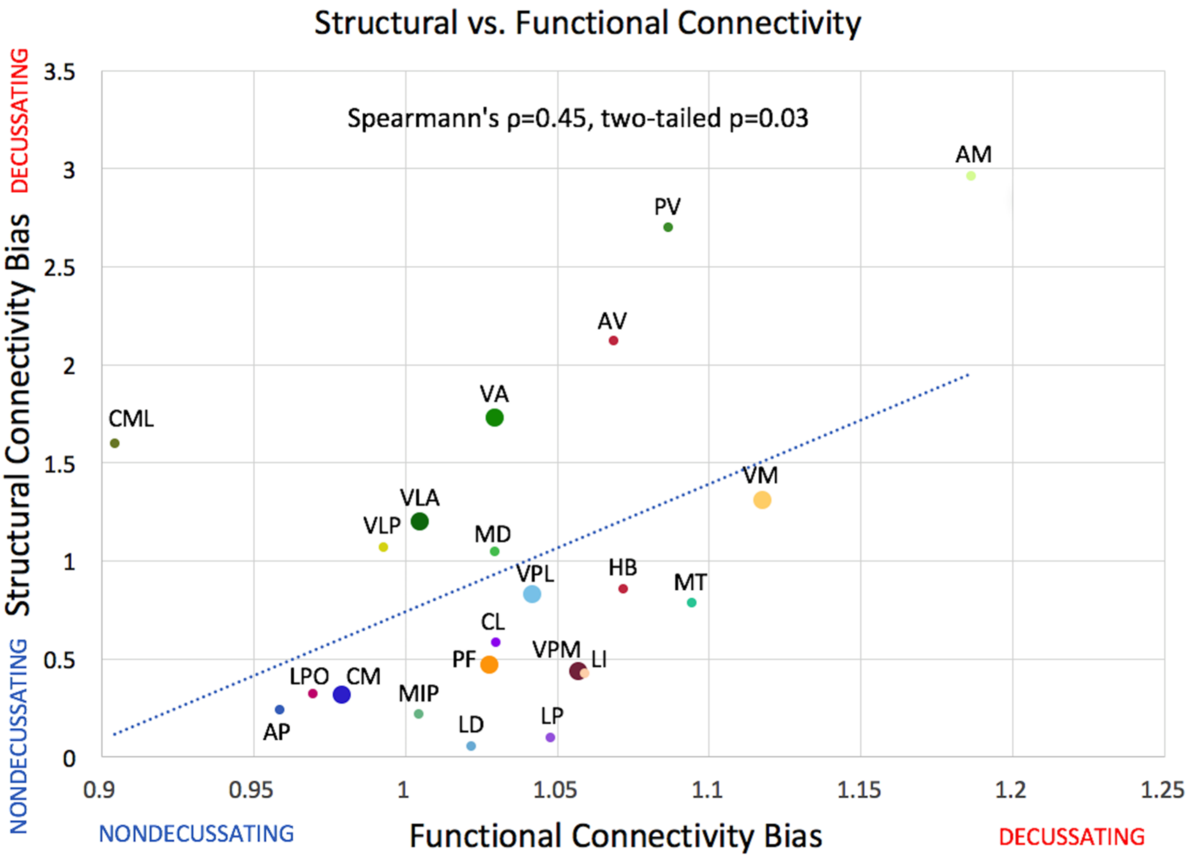

Fig. 3-5. Relationship between DRTT structural and functional connectivity decussating / nondecussating bias across nuclei. Structural connectivity d/nd ratio shown on x-axis for 23 thalamic nuclei, functional d/nd shown on y-axis (unitless). Colors and labels correspond to **Fig. 3-1**. Enlarged points represent nuclei receiving 5% or more of streamlines after adjustment for size. One nucleus (VPI) was a statistical outlier according to Grubb's test and has been omitted from this figure; however, its inclusion or exclusion did not affect the statistical significance of the relationship.

tractography studies, with streamlines originating in the various thalamic nuclei, may help to test the hypothesis that the d-DRTT and nd-DRTT have different cortical termination zones. Conversely, the substantial overlap between the d-DRTT and nd-DRTT in medial thalamic zones argues that the two pathways also participate in some shared circuits, which may explain how unilateral signals in the thalamus can exert effects on bilateral limb movements (Ellerman et al., 1994; Jäncke et al., 1999; Soteropoulos and Baker, 2008), and how surgical intervention in unilateral thalamus can result in bilateral cerebellar ataxia (Chun and Chang, 2017).

These findings are likely to influence our understanding of the mechanisms of tremor reduction in deep-brain stimulation. It is probable that a thalamic electrode placed unilaterally in the thalamus will activate some fibers of both the d-DRTT and nd-DRTT, thus exerting a more direct influence on bilateral cerebellar pathways that would be predicted from commissural interhemispheric connections alone. A straightforward way to test this principle would be to inactivate one-sided electrodes in subjects with bilateral movement disorders, such as essential tremor, and monitor tremor severity in both the ipsilateral and contralateral limb to determine if stimulation effects are bilateral when performing reaching and grabbing tasks.

It is important to note that diffusion-based tractography alone is insufficient to fully establish or refute the existence of a white-matter pathway. The existence of the nd-DRTT was shown by a prior study which performed human brain microdissections in addition to diffusion imaging (Meola et al., 2016). We make no claim to have independently verified the existence of this pathway, but rather offer comment on its anatomy in light of prior existential claims. Our observations likely warrant a future examination of the thalamic termination of the pathway in post-mortem brains coupled with high-resolution diffusion imaging.

This finding should be considered in the context of several limitations. First, the thalamic segmentation applied here was an interpolative estimate based on a model created using high-field structural MRI. At typical field strength (3.0 Tesla or less), accurate and consistent intrathalamic segmentation on T_1 images is challenging due to insufficient contrast. Therefore, although our model is a reasonable approximation of thalamic nuclei, some inconsistencies with the actual structures are likely. Our method can identify 23 distinct nuclei according to the Morel convention (Morel et al., 1997). Cross-validation on a leave-one-out basis on 9 subjects confirmed that this hierarchical statistical shape model significantly improved upon simple single-atlas and multi-atlas segmentation methods and agreed most strongly with the manual delineations of the nuclei. Structural connectivity data on a separate cohort of 43 healthy subjects also validated the segmentation of the pulvinar nucleus (Chakravorti *et al.*, 2018), one of the largest nuclei of the thalamus. This approach has thus been shown to perform accurately and reliably on healthy volunteers, and therefore was chosen for our segmentation purposes.

The size of some thalamic nuclei presents another challenge. For smaller nuclei, such as the habenula, with a volume of around 30 mm^3, precise determination of connectivity from these images may be difficult, as has been noted with regards to fMRI studies (Lawson et al., 2013), since the structure is only a few voxels in size. Our findings are best interpreted in terms of broader spatial patterns of connectivity rather than narrowly at each thalamic nucleus. Nevertheless, the consistent results between structural and functional connectivity support the conclusion that even for relatively small connectivity targets, repeatable connectivity measures are obtainable, even with divergent imaging modalities.

3.7 Clinical application

Multiple neurological diseases are linked to DRTT dysfunction. While our work on essential tremor has shown DRTT-related diffusion changes indicating microstructural pathology in the superior cerebellar peduncle (SCP) (Juttukonda et al., 2019), the role of this tract in the neurodegenerative Parkinsonian disorder progressive supranuclear palsy (PSP) is equally important but less extensively described. PSP is a tauopathy characterized by degeneration of white matter pathways, particularly the DRTT. To date, however, no study has linked this phenotype directly to changes in cerebellar functional connectivity.

We hypothesized that in PSP, (1) damage to DRTT white matter microstructure is associated with reduced functional connectivity between the dentate nucleus of the cerebellum, where the DRTT originates, and the thalamus, which is its terminus. We further hypothesized that (2) DRTT functional connectivity at baseline is predictive of longitudinal progression of white matter degeneration as measured by diffusion tensor imaging (DTI) metrics including diffusivity and anisotropy.

PSP patients (n=45) were curated from the 4 Repeat Tauopathy Neuroimaging Initiative (4RTNI) (age at baseline=69.6±7.4; 24 F/21 M). Patients were enrolled at four sites, The University of California-San Francisco, The University of California-San Diego, Massachusetts General Hospital, and the University of Toronto, which followed identical procedures for clinical testing and MRI. This patient cohort has previously been described in Gardner *et al.*, 2013; Dutt *et al.*, 2016; and Zhang *et al.*, 2016.

Patients underwent functional, structural, and diffusion MRI at the baseline visit and 6-month follow-up. MRI was conducted at 3.0 Tesla and included a standard T_1-weighted sequence, diffusion-weighted imaging (TR/TE=9200/82ms, spatial resolution=2.7 mm isotropic, 41 diffusion directions), and resting-state BOLD fMRI (TR/TE=2000/27 ms, spatial resolution=2.5 × 2.5 x 3 mm, slice gap=0.6mm). Diffusion-weighted MRI was eddy-corrected and motion-corrected, tensors were fit, and fractional anisotropy (FA) and mean diffusivity (MD) were calculated and mapped onto a common white-matter skeleton in standard space using tract-based spatial statistics (TBSS). The left superior cerebellar peduncle region-of-interest was defined using Johns Hopkins University white matter atlas (Mori et al., 2005), and the thalamus was defined using FSL FIRST. FA and MD values were extracted from the skeletonized DTI values within these regions.

Resting fMRI data preprocessing were performed using methods similar to those described in Chapter 2. Briefly, BOLD fMRI series were motion-corrected, spatially smoothed (FWHM=5mm), and co-registered to subject T_1 space and to the standard 2-mm MNI atlas. Functional connectivity was calculated using FEAT, with the combined bilateral dentate nuclei as the seed region in voxel-wise linear regression analyses. Motion parameters and the global signal were used as covariates of no interest. Z-statistics from subject-level modeling were averaged within the thalamus and these values were utilized as inputs in group-level statistics.

Statistics and hypothesis testing

Relationships between functional connectivity and structural measures of DRTT integrity were examined at baseline.

To test Hypothesis 1, that functional connectivity reflects white matter degeneration in the DRTT, we correlated baseline dentate-thalamus functional connectivity and DTI measures along this tract. FA and MD were calculated in the bilateral SCP and thalamus, and compared with subject-level dentate-thalamus connectivity z-statistics (FC).

Hypothesis 2 stated that functional connectivity is associated with future changes in DRTT white matter microstructure. Specifically, higher dentate-thalamus connectivity at baseline is hypothesized to reflect better DRTT function, and to correlate with smaller changes in DTI metrics. This hypothesis was tested by calculating 6-month changes in FA and MD in the SCP and thalamus (ΔFA and ΔMD) and correlating these values with functional connectivity at baseline. These analyses were conducted using Spearman's correlations to reduce the effects of outliers endemic to parametric tests. The false discovery rate was controlled at 0.10.

Results

Disease duration at baseline was 4.8±3.3 years (duration data were available for 32/45 patients). Baseline disease severity was assessed using PSP Rating Scale (PSPRS), with a mean score of 34.5±13.5 (PSPRS scores were available for 38/45 patients). In 6 months, PSPRS scores increased by a mean of 9.4±7.8 in this subset.

Hypothesis 1 indicated that functional connectivity and DRTT white matter integrity are positively related. Therefore, it predicts that white matter degeneration (lower FA, higher MD) is correlated with decreased functional connectivity between the dentate nucleus and thalamus. We found that dentato-thalamic functional connectivity was negatively correlated with MD in the SCP (rho=-0.41; p=0.0049) and thalamus (rho=-0.33; p=0.025), but was not correlated with FA in either of these regions.

Hypothesis 2 was that dentate-thalamus functional connectivity at baseline is associated with 6-month changes in white matter integrity. Baseline dentato-thalamic connectivity was not correlated with ΔFA or ΔMD in the SCP, but was positively correlated with ΔFA in the thalamus (rho=0.34; p=0.023), meaning that greater functional connectivity at initial measurement is related to less severe declines in thalamic white mater DTI over 6 months longitudinal follow-up.

Discussion

Both the dentate nucleus and SCP are susceptible to degeneration in PSP, and are possible biomarkers of disease severity (Agosta et al., 2014; Knake et al., 2010; Surova et al., 2015; Whitwell et al., 2014; Zhang et al., 2016). The dentate is especially vulnerable to tau aggregation (Kanazawa et al., 2009), however, no studies have linked longitudinal microstructural changes with functional connectivity in this pathway using the same subject cohort. We hypothesized that functional synchrony between the origin and terminus of this pathway reflect structural changes to the underlying white matter.

Our data suggest that in PSP, DRTT white matter degeneration is related to decreased cerebellar-cerebral functional connectivity. Further, baseline DRTT connectivity appears to correlate with white matter changes longitudinally, suggesting that DTI in this region could serve as a prognostic biomarker of PSP severity. The DRTT has previously been implicated as susceptible in PSP (Whitwell et al., 2011), a condition characterized by reduced thalamic functional connectivity with premotor cortex and cerebellum (Whitwell et al., 2011) and decreased connectivity between the brainstem and cortex (Gardner et al., 2013). These data are consistent with the hypothesis that PSP patients have reduced cerebellar efferent signaling, consistent with the finding of diminished motor cortex response to transcranial magnetic stimulation of the cerebellum (Shirota et al., 2010).

We identified correspondences between white matter microstructure in the SCP, and functional connectivity between the dentate and thalamus. However, future work should also measure connectivity between the dentate nucleus and basal ganglia, as previous studies have observed that changes in diffusion coefficients in the putamen, globus pallidus, and caudate nucleus distinguish PSP from Parkinson’s disease (Seppi et al., 2003).

It is a reasonable inference that PSP-related white matter degeneration, coupled with tau aggregation and neural death in the dentate nucleus, may cause the observed decline in cerebellar functional connectivity; however, it is worth remarking that the correlative analysis performed here does not strictly imply a causal relationship between degeneration of the white matter and decreased functional connectivity.

Nonetheless, this work identifies a potentially important link between longitudinal degradation of the DRTT and disease-related dysfunction in a key white matter pathway connecting the cerebellum to the cerebral cortex. Future studies should examine the clinical impact of this relationship on the development of motor and cognitive symptoms.

3.8 Conclusions

These findings demonstrate how pathological changes to white matter neuroanatomy may influence activity in distributed functional networks. The DRTT is an excellent example of how dysfunction and degeneration in a constrained anatomical region can influence neural activity dynamics in broader cortical networks, especially when white matter tracts contact essential neural hubs like the thalamus. Further studies of other Parkinson’s-plus syndromes, such as corticobasal syndrome, may determine whether these findings are generalizable to the broader spectrum of movement disorders. Additionally, this work should be contextualized by examination of cortical gray matter changes which may be relevant to the degenerative process; for instance, in the motor cortex.

CHAPTER 4

FUNCTIONAL BRAIN NETWORK DETECTION STRATEGIES FOR ARTERIAL SPIN LABELING PERFUSION MRI

4.1 Purpose

While traditional fMRI methods are useful for the interpretation of broad-based neural networks, the dependence of these approaches on the blood oxygenation level-dependent contrast presents substantial technical problems. In this chapter, an alternative approach is explored: arterial spin labeling-based functional connectivity. The use of perfusion-based signal for identification of brain connectivity patterns offers the possibility of detecting novel information about brain networks. Perfusion dynamics allow more quantitative approach to connectivity measurement, and the use of single-shot readouts with both gradient and spin echoes allows perfusion imaging with less vulnerability to susceptibility artifacts and mislocalized vascular signal sources.

4.2 Summary

Functionally connected brain resting-state networks (RSNs) are commonly identified using susceptibility-weighted blood oxygenation level-dependent (BOLD) contrast, which originates primarily from venous blood water. Arterial spin labeling (ASL)-based functional connectivity (ASL-FC) measures perfusion fluctuations at the capillary level and is less susceptibility-weighted. Here, ASL preprocessing strategies were systematically investigated and ASL-FC spatiotemporal information compared to BOLD-FC for common RSNs in healthy participants (n=20; age=29.5±7.3 years, sex=10M/10F). Pseudo-continuous ASL with a 3D gradient-and-spin-echo

(GRASE) readout (TR/TE=3900/13 ms, label duration=1800 ms, post-labeling delay=1800 ms) and gradient-echo BOLD[b] (TR/TE=1400/35 ms) at matched spatial resolution (3.8 mm isotropic) were acquired using 3T MRI. Seed-based connectivity was performed with various ASL preprocessing strategies: surround subtraction, frequency filtering, global signal regression, motion regression, component-based noise correction (CompCor), and spatial smoothing. ASL-based independent component analysis (ASL-ICA) was also performed, and results were spatially compared to canonical literature RSNs using Dice coefficients (significance: $p<0.05$ after false discovery rate correction). Spatial characteristics were contrasted between methods by calculating the center of mass, and temporal features quantified by calculating network power over the detectable frequency ranges. Surround subtraction, spatial smoothing, and CompCor significantly increased spatial overlap between ASL and BOLD RSNs. These were combined into a single ASL-FC preprocessing pipeline, which improved group-level ASL RSN consistency with BOLD, increasing the mean ASL-to-BOLD Dice score from 0.20 to 0.31. ASL-ICA RSNs were largely consistent with database BOLD RSNs reported in the literature, with spatial overlap similar to BOLD-ICA maps from this study (ASL mean Dice=0.49, BOLD mean=0.42). Spatial differences between ASL and BOLD RSNs included closer cortical localization for ASL-FC. Spectral analysis showed that ASL-FC contains power over a broad, constant low-frequency regime (0-0.06 Hz) compared to BOLD-FC, which peaked at 0.02 Hz following standard processing. Study findings are used to propose improved ASL-FC processing strategies and demonstrate that when these strategies are applied, ASL-FC provides unique spatial and temporal information.

---

[b] Strictly, the blood oxygenation level-dependent (BOLD) effect refers to the physiological phenomenon which is often the basis for fMRI. For brevity, in this chapter the term BOLD will also be used as a shorthand for T_2*-weighted sequences sensitive to this effect, which typically utilize gradient echoes and 2D echo-planar imaging.

4.3 Introduction

Human brain functional connectivity is most commonly evaluated using blood oxygenation level-dependent (BOLD) contrast, in which temporal correlations between BOLD signals are assessed in seed-based (Biswal et al., 1995; Fox et al., 2005) or independent component analyses (ICA) (Beckmann et al., 2005; McKeown et al., 1998) to identify co-activation patterns, defined broadly as resting-state networks (RSNs).

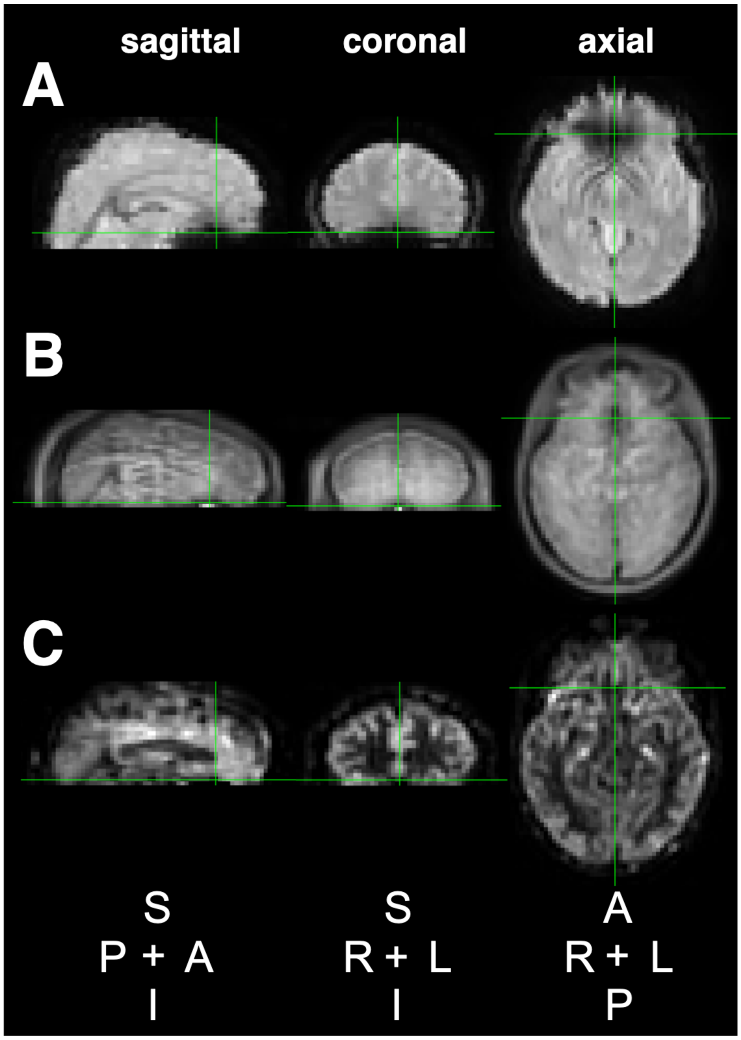

Fig. 4-1. **Comparison of ASL and T_2*-weighted echo planar imaging modalities.** Orthogonal representations of (A) T_2*-weighted blood oxygenation level-dependent (BOLD)-sensitive image with TE=35 ms, (B) unsubtracted arterial spin labeling (ASL) 3D GRASE with TE=13 ms, and (C) pair-wise subtracted cerebral blood flow (CBF)-weighted map from the ASL acquisition. Owing to the long TE in (A), distortion and dropout is apparent in regions of high susceptibility, such as the orbitofrontal cortex (green cross). These artifacts reduce when ASL is used, which may allow for brain connectivity and activation to be detected with higher fidelity in these regions.

BOLD signal fluctuations originate from changes in water relaxation near diamagnetic oxyhemoglobin and paramagnetic deoxyhemoglobin. Because arterial blood is consistently near full oxygen saturation, variations in oxygenation largely localize to capillary and venous vasculature (Duong et al., 2003). BOLD is therefore highly sensitive to changes in effective venous T_2 and T_2*, which may not always co-localize with neuronal activity (Kim et al., 1994). Such contrast can also extend into water in the extravascular spaces or cerebrospinal fluid (Donahue et al., 2011).

To exploit this contrast, BOLD sequences must be heavily susceptibility-weighted, and therefore are sensitive to magnetic susceptibility artifacts and distortion near air-tissue boundaries (e.g., **Fig. 4-1**). BOLD signal is also not a direct correlate of neural metabolism, but depends on multiple physiological parameters, including regional cerebral blood flow (CBF) and oxygen extraction fraction (Buxton et al., 1998; Ogawa et al., 1993; van Zijl et al., 1998). BOLD also requires multiple preprocessing steps, including removal of global artifacts, motion parameters, respiratory correction, and baseline drift detrending (Rane et al., 2014; Weissenbacher et al., 2009).

In principle, many of these limitations can be reduced with ASL-based functional connectivity (ASL-FC). ASL is an established non-invasive MRI technique for CBF measurement (Alsop et al., 2015; Williams et al., 1992), and uses radiofrequency pulses to invert magnetic spins in arterial blood water, which then act as an endogenous, diffusible tracer. By comparing labeled and unlabeled images, CBF-weighted signal is obtained, which can be quantified in absolute units (ml blood/100g tissue/minute) upon application of the solution to the flow-modified Bloch equation. ASL may provide more specific indicators of neural activity than BOLD, as CBF is tightly coupled to cortical glucose metabolism (Jueptner and Weiller, 1995; Musiek et al., 2012). Due to shorter echo times, CBF-weighted images have fewer susceptibility artifacts and may improve connectivity estimates in iron-rich regions with rapid T_2(*) dephasing, such as the cerebellar dentate nucleus (Deistung et al., 2016). Finally, ASL should not require identical preprocessing strategies to BOLD due to the acquisition design, in which spin-labeled and unlabeled volumes are interleaved. Subtraction of alternating images inherently compensates for instrument drift and other low-frequency noise. This approach is additionally advantageous because low-frequency activity may represent functionally meaningful information excised in typical BOLD preprocessing (Viviani et al., 2011).

However, ASL-based connectivity poses methodologic challenges. Because the signal contributions from labeled blood water constitute a small fraction of background intensity, ASL signal-to-noise ratio (SNR) is generally low compared to BOLD (cortical SNR=1-12). This can be improved by the use of 3D readouts (Gunther et al., 2005; Petersen et al., 2017) and pseudo-continuous ASL (pCASL) labeling (Dai et al., 2008). Additionally, ASL has poor temporal resolution due to the long combined labeling duration and post-labeling delay (typically 3500-4500 ms) and subtraction of control-label pairs, which produces an effective temporal resolution of 7000-9000 ms.

Here, previously unexamined preprocessing strategies were examined for RSN detection in ASL. Spatial and frequency information were compared between ASL-FC and BOLD-FC. The objectives were to identify preprocessing steps that improve ASL-FC fidelity in commonly observed networks, and to understand how these approaches provide additional spatiotemporal information compared to BOLD.

4.4 Methods

Imaging

Healthy participants (n=20; age=29.5±7.3 years, sex=10M/10F) provided informed, written consent in compliance with the Institutional Review Board. Participants were scanned at 3.0 Tesla (Philips, Best, The Netherlands) using body coil transmission and SENSE 32-channel phased array reception. Participants were instructed to remain awake with eyes open for the duration of the scan session.

The imaging protocol included a 20-minute (300-volume) resting-state pCASL scan (TR/TE=3900/13 ms, PLD=1800 ms, label duration=1800 ms, in-plane acceleration=3, through-plane acceleration=2, field-of-view=80x80x25, spatial resolution=3.8 mm isotropic). ASL implementation followed recent guidelines (Alsop et al., 2015). A 3D GRASE Cartesian readout was applied with in-plane and through-plane acceleration to reduce readout duration and associated signal smearing; a single-shot rather than multi-shot readout was utilized to improve the temporal resolution. To understand how ASL-based networks compared with those detected from BOLD, a 20-minute (840 volume) BOLD acquisition with single-shot gradient echo planar imaging readout (TR/TE=1400/35 ms) at identical spatial resolution (3.8 mm isotropic, field of view=80x80x25) was acquired. To test whether arousal may vary due to habituation to the MRI environment between the first and second scans, heart rate and respiration were monitored in a subset of participants (n=4) using a pulse oximeter and respiration bellows. Standard T_1-weighted magnetization-prepared rapid gradient-echo (MPRAGE) scans (TR/TE=8.9/4.6 ms, spatial resolution=1 mm isotropic) were acquired for co-registration.

ASL-FC and BOLD-FC pre-processing

The approach for this work was to apply systematic pre-processing steps in sequence to the pCASL data and compare network detection performance from each of these steps to standard BOLD-FC. Image preprocessing and connectivity analyses were performed using the FMRIB Software Library (FSL) (Smith et al., 2004) and custom Matlab scripts (Mathworks, Natick MA). For all analyses, data were motion-corrected using MCFLIRT (Jenkinson et al., 2002) and motion parameters preserved. From these motion-corrected data, seven preprocessing steps were individually tested for their effect on the spatial organization of five common RSNs: default mode network (DMN), visual network (VN), sensorimotor network (SMN), salience network (SN), and central executive network (CEN), also referred to as fronto-parietal network. These networks were chosen because they are routinely detected in functional connectivity studies. DMN and SN were also selected for having nodes adjacent to high-susceptibility limbic cortical regions. Preprocessing steps were:

1. Surround subtraction, in which each spin-labeled volume was subtracted from the mean of the preceding and following unlabeled volumes.
2. Moderate low-pass filtering (cutoff=0.10 Hz).
3. Strict low-pass filtering (cutoff=0.05 Hz).
4. Motion regression. Motion parameters (three translation, three rotation) were added as covariates to connectivity analysis; motion correction was performed on unsubtracted images, therefore displacement for labeled and unlabeled volumes were averaged for each subtracted pair.
5. Global signal regression (GSR).
6. Component-based noise correction (CompCor). White matter (WM) and lateral ventricular CSF regions were identified from T_1-weighted images using FSL-FAST. WM regions were eroded by 3 mm to avoid gray matter partial voluming. The combined WM-CSF mask was registered to ASL and BOLD scans. MELODIC (Beckmann and Smith, 2004) was used to decompose signals in this region into independent components. The top three components by explained variance were regressed from the whole brain.
7. Spatial smoothing (FWHM=5 mm).

To provide a standard for comparison, BOLD images were subject to preprocessing steps reflecting typical practices in functional connectivity literature. BOLD images were motion corrected using MCFLIRT, bandpass filtered (0.01-0.10 Hz), spatially smoothed (FWHM=5 mm), denoised using CompCor (nuisance components=3), and motion and global signal regressed.

Seed-based functional connectivity analysis

Using the ASL and BOLD pre-processed images, seed-based connectivity was performed in native space. Seed regions (diameter=5 voxels) were placed in the posterior cingulate cortex for DMN, right occipital pole for VN, right primary motor cortex for SMN, right anterior insula for SN, and right dorsolateral prefrontal cortex for CEN using standard anatomical landmarks. The same seed regions were used for ASL and BOLD. Voxel-wise regression analyses were performed with FEAT (Woolrich et al., 2001). Resultant maps were converted to z-statistics by Fisher's transform, and voxels with a z-statistic greater than two standard deviations above the mean of all voxels were included in the binary RSN mask. Such proportional thresholding can produce more stable network measures than thresholding at a fixed, arbitrary numerical value (Garrison et al., 2015). BOLD-FC maps were thresholded in the same manner. RSNs were compared using Sørensen–Dice coefficients (Dice, 1945; Sørensen, 1948). Paired t-tests with false discovery rate (FDR)=0.05 (Benjamini and Hochberg, 1995) were applied to determine significant differences between Dice coefficients. Finally, a combined preprocessing strategy was created which incorporated all preprocessing steps that significantly improved ASL-BOLD overlap for at least 40% of RSNs.

This pipeline was used for comparison of spatial and temporal ASL-FC features in subsequent analyses.

We next calculated group-level RSNs from the non-preprocessed ASL, combined-preprocessing ASL, and BOLD data. For group-level analyses, data were transferred to the 2-mm MNI152 brain using T_1-weighted images as registration intermediates. T_1-weighted images were nonlinearly warped to MNI space using FNIRT (Andersson et al., 2007), and this warp was then applied to subject RSNs. A one-sample permutation test was applied with the Randomise function running 500 permutations and threshold-free cluster enhancement (TFCE) (Smith and Nichols, 2009). Finally, group-level connectivity maps were binarized by inclusion of all voxels with z-score>1.5.

ASL-FC and BOLD-FC RSNs were examined for spatial differences by taking center-of-mass measures in specific nodes and calculating the distance to the cortical surface. ASL and BOLD were also compared temporally by calculating power spectra for combined-preprocessing ASL and BOLD time courses using the Fslpspec function. Mean power in each RSN was extracted for the interval between 0 and 0.10 Hz, and normalized for comparison, with a mean fixed at unity. To measure ASL-FC reproducibility, a subset of participants returned for follow-up scans on different days. Images were acquired and processed as above. Resulting binary RSN maps were registered to the first-day ASL scan using the T_1-weighted images for reference. Dice scores were calculated to measure inter-session reproducibility.

To ensure that RSN identification from ASL-FC is not due to BOLD contamination, ASL-FC analysis was repeated on unlabeled (control) ASL volumes exclusively. These images lacked perfusion weighting and are expected to be predominated by any possible residual BOLD effects at the short-to-intermediate TE=13 ms used. Dice coefficients were calculated to compare unlabeled ASL to subtracted ASL in terms of spatial overlap with BOLD.

ASL and BOLD were matched for duration, and therefore ASL included fewer volumes (150) than BOLD (840). To test whether this affected connectivity results, BOLD time courses were modified to approximate ASL by sampling every fifth BOLD volume (effective TR=7.0s) and reducing the final length to 150 volumes. Seed-based functional connectivity analysis was performed as before on downsampled BOLD.

Independent component analysis

While the main focus of this study was on seed-based connectivity, for completeness data-driven ICA was also investigated. ASL images were preprocessed using the optimal strategy found above, transformed to 2-mm MNI space, temporally concatenated, and decomposed into independent components using MELODIC. RSNs were identified by comparing the calculated components with the five canonical networks above. In cases where multiple components corresponded to a single RSN (e.g., right and left sub-networks), these were combined to yield a single composite network. Components were normalized and thresholded as in the seed-based analysis. Downsampled BOLD series were concatenated and ICA was conducted in the same manner. Downsampled images were used for BOLD-ICA because the number of components supported depends on input matrix size, and matching the input volume count reduces bias between methods.

These networks were compared to results from three datasets previously presented in the literature: Smith et al., (2009) utilized (1) resting-state BOLD and (2) BrainMap, which cataloged activations from over 30,000 fMRI participants, to show that similar networks could be derived from resting fluctuations and task-based functional co-activations; while (3) Yeo et al., (2011) utilized a clustering approach on 1,000 resting BOLD datasets to parcellate the brain into stable co-active networks. From Smith et al.'s 20-component resting-state results, DMN (map 4_{20}) and SMN (6_{20}) were selected without modification. Occipital and medial VN (1_{20}, 2_{20}), and left and right CEN (fronto-parietal network) (9_{20}, 10_{20}) were combined. From the 70-component decomposition, anterior insula and the ventromedial/anterior cingulate node (19_{70}, 21_{70}) were combined into SN. From the BrainMap analysis, the same component numbers were used for all networks except SN, for which no component was identified. Components were thresholded identically to the original paper. From Yeo et al., DMN (map 7_7), VN (1_7), SMN (2_7), SN (4_7) from the 7-network decomposition were used without modification, while (12_{17} and 13_{17}) from the 17-network decomposition were combined into CEN.

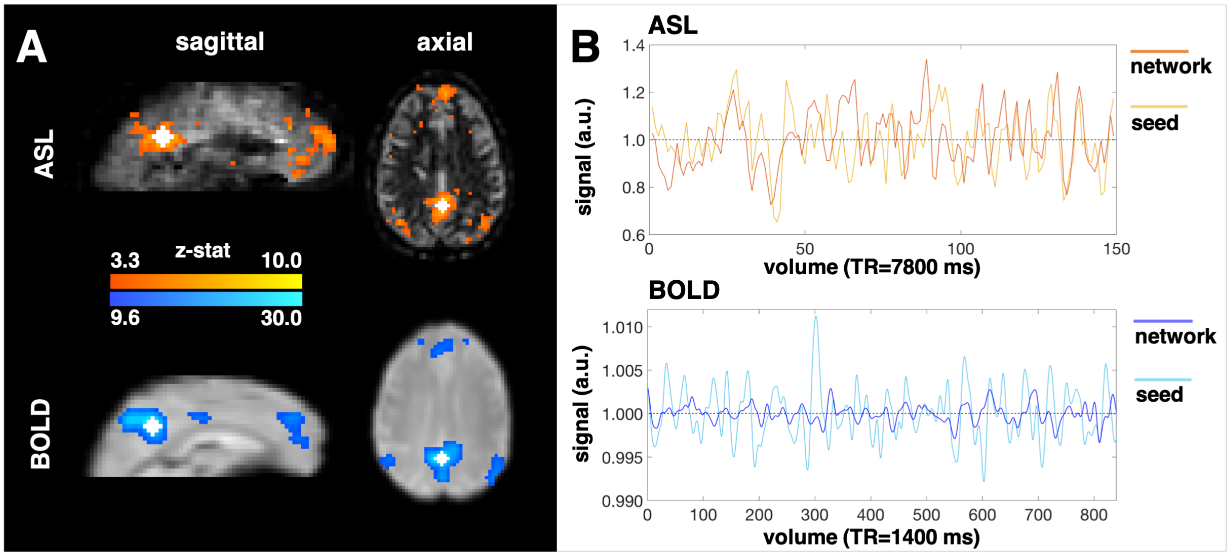

Fig. 4-2. ASL and BOLD-derived networks. (A) Representative arterial spin labeling (ASL) difference magnetization (ΔM) map from a 24-year-old female and blood oxygenation level-dependent (BOLD) image with 34-year-old male showing detection of the default mode network on a single-subject basis. Seed regions (volume = 1.81 mL) are demarcated in white. (B) Time-courses from seed regions and networks over the 20 min acquisition. Y-axis scales for ASL and BOLD differ as mean image intensity is several orders of magnitude higher for BOLD than subtracted ASL. Note that the TR was 1400 ms for BOLD and 7800 ms for one ASL control-label pair and that the vertical axes are scaled differently between ASL and BOLD owing to the large difference in mean signal intensity. Z-statistic scale differs between modalities because the mean z-statistic was higher for BOLD than ASL, and thus the threshold for inclusion in the network was higher.

4.5 Results

Demographics

Twenty healthy subjects (age=29.5±7.3 years, sex=10M/10F) were included in the study, of whom 8 (age=27.6±4.7 years, sex=4M/4F) returned for follow-up imaging (mean interval=30.1±32.1 days). Representative ASL and BOLD images, single-subject RSNs, and time series are shown in **Fig. 4-2**. In the subset of participants with physiological monitoring, the cardiac and respiratory frequencies were not significantly different between ASL and BOLD scans, nor between scans that were performed first vs. second (cardiac frequency: ASL=1.30±0.10 Hz, BOLD=1.25±0.15 Hz, p=0.32; respiration frequency: ASL=0.28±0.04 Hz, BOLD=0.27±0.03 Hz, p=0.22).

	none	**surround sub.**	**bandpass <0.10**	**bandpass <0.05**	**GSR**	**motion reg.**	**CompCor**	**smoothing**	**combined**
DMN	0.124	0.133	0.119	0.097	0.132	0.121	0.146	0.147	0.184
p-val.		0.0415	0.331	<0.001***	0.280	0.265	0.018*	<0.001***	<0.001***
VN	0.183	0.205	0.170	0.130	0.197	0.178	0.192	0.231	0.255
p-val.		0.010*	0.040	<0.001***	0.328	0.073	0.152	<0.001***	0.004**
SMN	0.130	0.135	0.122	0.096	0.149	0.129	0.146	0.154	0.173
p-val.		0.108	0.019*	<0.001***	0.052	0.527	0.029*	<0.001***	0.001**
SN	0.088	0.101	0.116	0.112	0.089	0.088	0.082	0.096	0.141
p-val.		0.003**	<0.001***	0.006**	0.895	0.624	0.217	0.001**	<0.001***
CEN	0.161	0.164	0.143	0.111	0.149	0.153	0.170	0.191	0.158
p-val.		0.456	<0.001***	<0.001***	0.051	0.140	0.009**	<0.001***	0.654

Table 4. Subject-level ASL-BOLD Dice scores. Mean subject-level Dice scores for each preprocessing strategy and resting-state network. P-values comparing each strategy to baseline listed below. Abbreviations: GSR=global signal regression, DMN=default mode network; VN=visual network; SMN=sensorimotor network; SN=salience network; CEN=central executive network. Significance key: *=p<0.05, **=p<0.01,***=p<0.001. Only comparisons surviving false discovery rate=0.05 correction are highlighted.

Seed-based functional connectivity.

Of the seven ASL preprocessing strategies, three met the criteria for significantly improving ASL-BOLD spatial overlap at the subject level: surround subtraction, CompCor, and spatial smoothing (**Table 4**). These were included in a combined preprocessing pipeline. Bandpass filtering, motion regression, and global signal regression did not improve ASL-BOLD overlap. In comparison with unpreprocessed ASL, the combined pipeline improved group-level ASL-BOLD Dice scores for all five networks; mean Dice score increased from 0.20 to 0.31 (**Fig. 4-3**; **Table 5**). To test whether results depended on the different number of volumes between ASL and BOLD, overlap between RSNs from ASL-FC and those from downsampled (150-volume) BOLD were calculated. ASL preprocessing similarly increased Dice scores for all five networks, from a mean of 0.23 to 0.37.

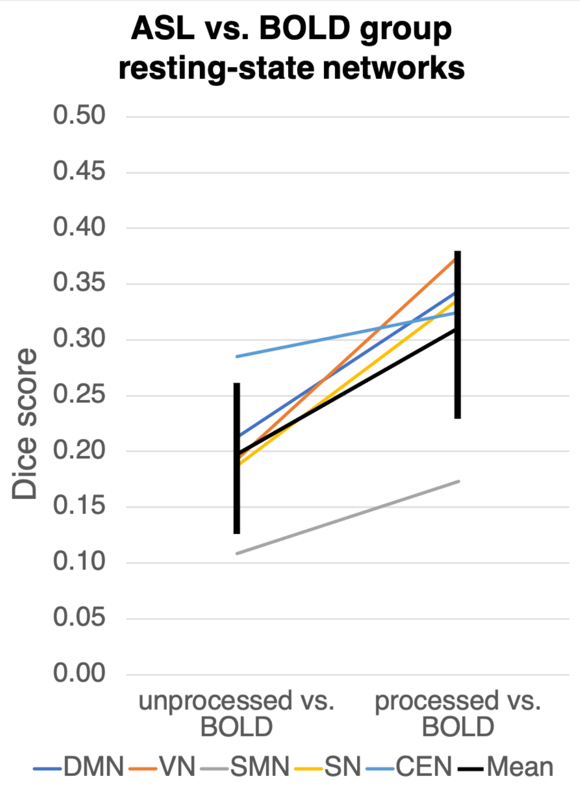

Fig. 4-3. Effects of ASL preprocessing on network overlap. The combined ASL preprocessing pipeline improved overlap between group ASL RSNs and group BOLD RSNs for all five networks. Error bars represent one standard deviation above and below the mean.

	ASL-FC vs. BOLD-FC (seed-based)	
	Unprocessed	**Combined preprocessing**
DMN	0.21	0.34
VN	0.19	0.37
SMN	0.11	0.17
SN	0.19	0.34
CEN	0.29	0.32
Mean± standard deviation	0.20±0.06	0.31±0.08

Table 5. Seed-based group-level ASL-BOLD Dice scores for five resting-state networks. These data correspond to **Fig. 4-3.** At the group level the combined ASL preprocessing strategy improved overlap between ASL and BOLD-derived networks substantially. We note that the sensorimotor network (SMN) was not as well detected in the seed-based analysis as in independent component analysis (see **Table 6**).

RSNs derived from ASL and BOLD differed spatially. Group-level DMN from ASL included a prefrontal node with center of mass located 5 mm closer to the cortical surface (anterior) than the BOLD-derived network (**Fig. 4-4A**). VN center of mass was localized 15 mm closer to the cortical surface (posterior) in ASL

than BOLD (**Fig. 4-4B**). SMN center of mass was 11 mm closer to the surface (superior) in ASL than BOLD (**Fig. 4-4C**). The medial SN node's center of mass was 9 mm closer to the orbitofrontal cortex (inferior) in ASL than BOLD (**Fig. 4-4D**). Finally, the CEN's center of mass was 12 mm closer to the cortical surface (superior) in ASL than BOLD (**Fig. 4-4E**).

ASL frequency profiles differed from BOLD. For all five RSNs, BOLD power spectra showed a peak near 0.02 Hz, with power decreasing above and below that value. ASL power spectra showed consistent power between 0 and 0.06 Hz, including frequencies below 0.01 Hz, and reducing above 0.06 Hz (**Fig. 4-5**). This cutoff corresponds to the Nyquist frequency for the ASL acquisition.

ASL-FC inter-session reproducibility was improved by combined preprocessing in four of five RSNs. DMN Dice increased from 0.14 to 0.18. VN Dice increased from 0.19 to 0.29. SMN

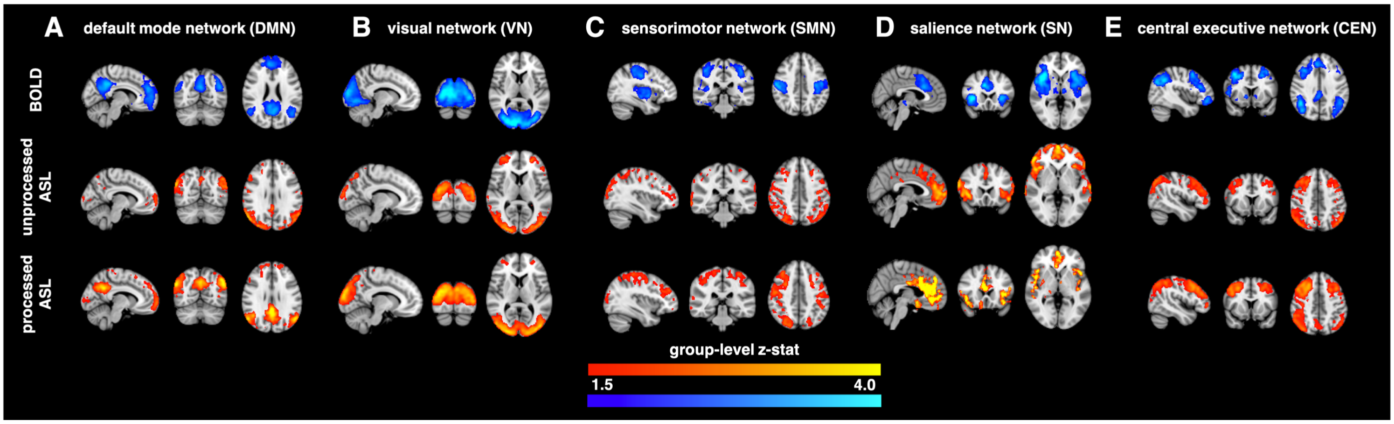

Fig. 4-4. Seed-based group-level results for (A) default mode network, (B) visual network, (C) sensorimotor network, (D) salience network, and (E) central executive network, derived from arterial spin labeling (ASL) and blood oxygenation level-dependent (BOLD) functional connectivity analysis. 2-mm MNI coordinates (x,y,z): A: (41,31,48); B: (50,20,40); C: (63,47,57), D: (43,73,36), E: (24,69,54).

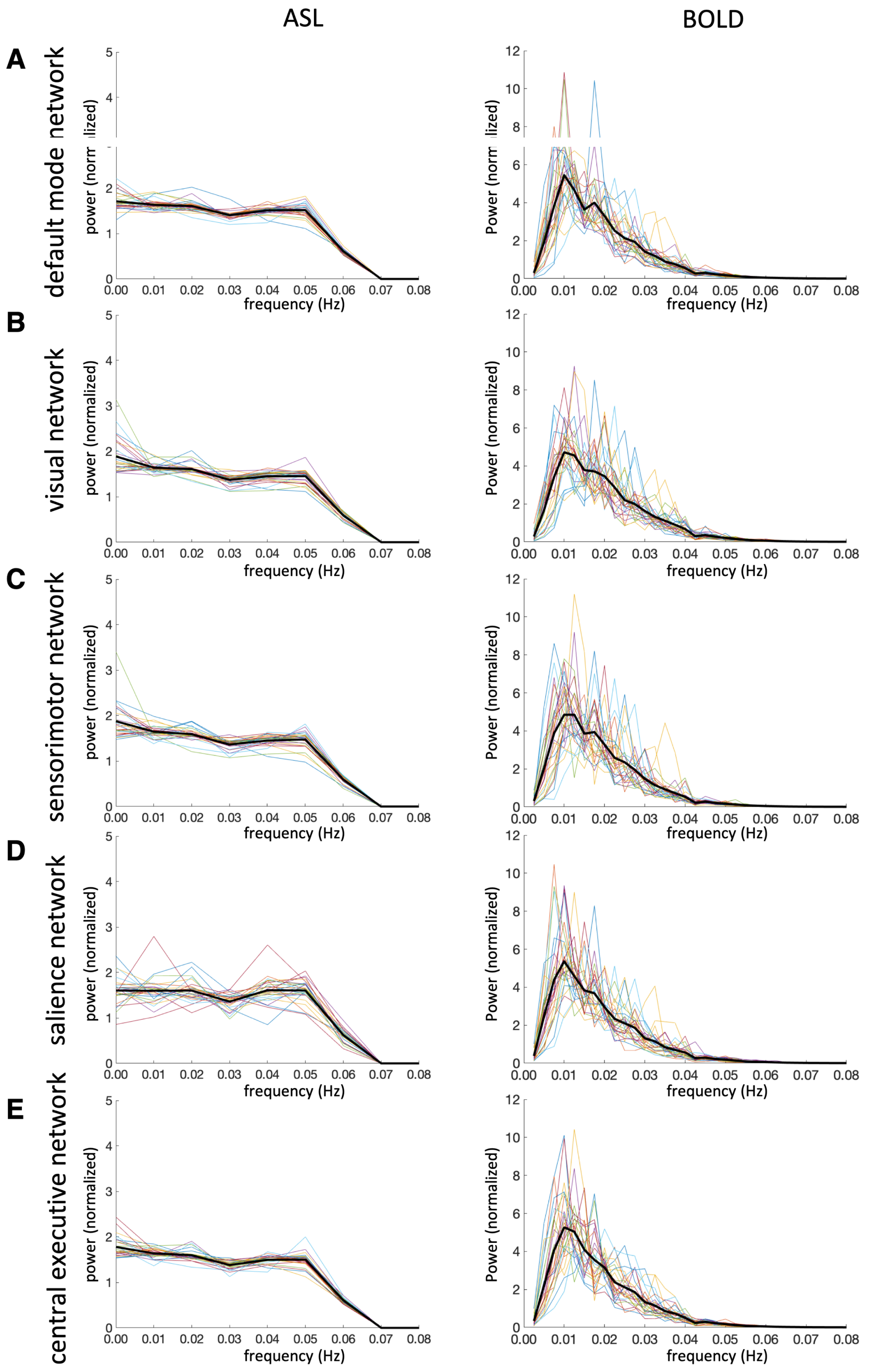

Fig. 4-5. Power spectra analysis for arterial spin labeling (ASL) and blood oxygenation level-dependent (BOLD) in (A) default mode network, (B) visual network, (C) sensorimotor network, (D) salience network, and (E) central executive network. Each color represents one participant, with the mean power for each participant fixed at 1.0 (i.e. normalized) for comparison. The thicker black line represents mean across all participants.

Dice increased from 0.18 to 0.25. CEN Dice increased from 0.17 to 0.24. By contrast, SN Dice decreased from 0.30 to 0.16. **Fig. 4-6** summarizes an example of RSNs derived from repeated scans.

Subtracted (perfusion-weighted) ASL significantly outperformed unlabeled ASL at identification of DMN, VN, SMN, and CEN ($p<0.001$ for each), the exception being SN, in which perfusion-weighting performed slightly worse than unlabeled ASL ($p=0.008$). These data on average are inconsistent with the RSN origin being primarily due to residual BOLD contamination in the moderate-TE 3D GRASE readout.

Independent component analysis

ASL data were preprocessed for ICA using the combined strategy, excluding CompCor, since ICA identifies orthogonal components including structured noise. Group ASL-ICA yielded 56

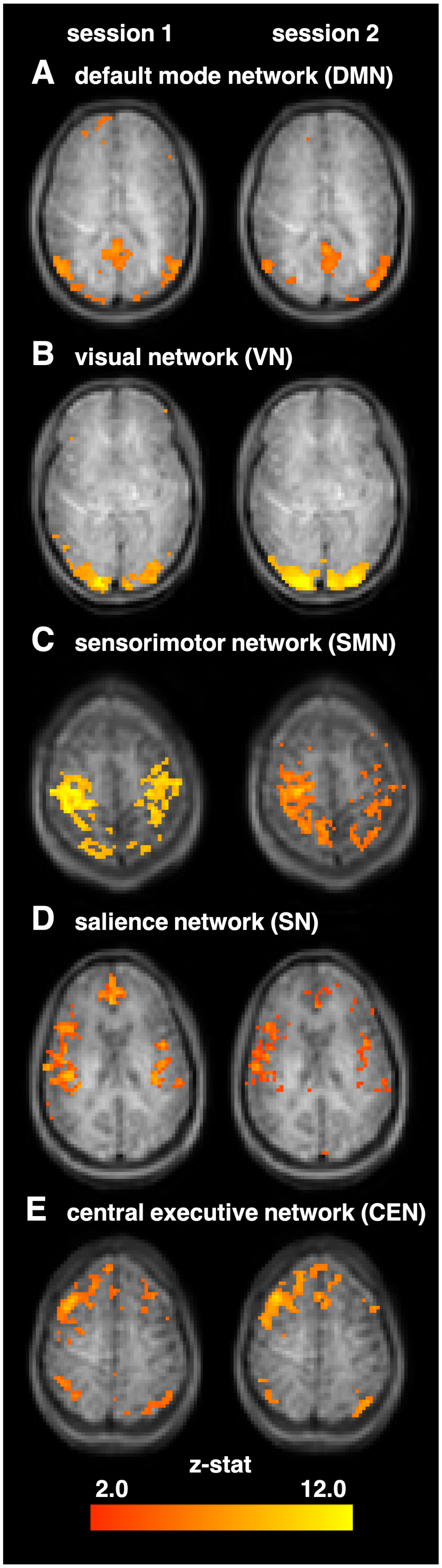

Fig. 4-6. ASL-FC Reproducibility. Participants underwent an identical imaging protocol an average of 25.6 days after the initial visit. Resulting networks were subject to seven preprocessing approaches (the combined approach is shown here). Examples of ASL-derived subject-level (A) default mode network, (B) visual network, (C) sensorimotor network, (D) salience network, and (E) central executive network are shown for both imaging sessions. Subject-level reproducibility scores were highest for visual network. As seen in (C; Session 2), not all networks could be clearly identified in each individual session.

independent components, and BOLD-ICA yielded 71, including components identified with the five common RSNs.

Our ASL-ICA spatially reflected RSNs from Smith et al., with Dice scores comparable to, or slightly higher than, those for BOLD-ICA (ASL-FC mean=0.49, BOLD-FC mean=0.42). ASL-ICA also performed comparably to our BOLD-ICA in reflecting the clustering-based RSNs from Yeo et al., with higher Dice scores for four of five networks (ASL-FC mean=0.41, BOLD-FC mean=0.34) (**Fig. 4-7**, **Table 6**). Finally, ASL-ICA also spatially reflected BrainMap-derived activation networks. Dice scores for our ASL-ICA were higher than for our BOLD-ICA in the four examined networks (ASL-FC mean=0.46, BOLD-FC mean=0.33).

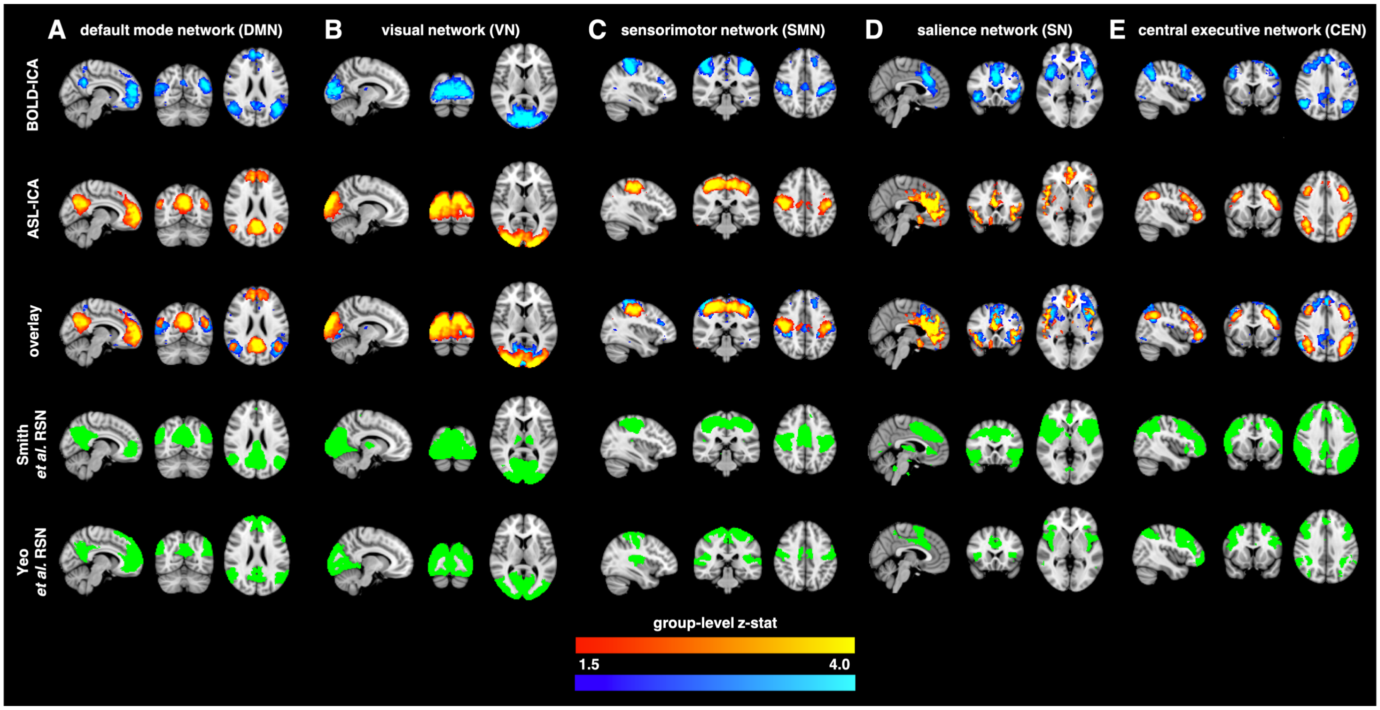

Fig. 4-7. Group-level independent component analysis (ICA) results for (A) default mode network, (B) visual network, (C) sensorimotor network, (D) salience network, and (E) central executive network, derived from arterial spin labeling (ASL) and blood oxygenation level-dependent (BOLD) functional connectivity analysis. RSNs from Smith et al. and Yeo et al. are shown for comparison. 2-mm MNI coordinates (x,y,z): A: (41,31,48); B: (50,20,40); C: (63,47,57), D: (43,73,36), E: (24,69,54).

4.6 Discussion

This study applied perfusion-weighted ASL-FC to healthy subjects to characterize spatial and temporal features of canonical brain networks. The goal was to determine whether ASL-FC preprocessing could largely replicate spatial patterns of BOLD RSNs, and if so, whether this approach provides new information on spatial or temporal features of RSNs. Systematic investigation of multiple preprocessing procedures demonstrated the effectiveness of surround subtraction, spatial smoothing, and regression of noise components from non-gray matter tissue. This approach improved seed-based ASL-BOLD spatial matching for the five distinct RSNs: DMN, VN, SMN, SN, and CEN. Residual differences between ASL and BOLD results also emphasize potential advantages of ASL-FC. ASL RSNs appear to localize more closely to cortical regions than BOLD RSNs, and include more information in frontal and orbitofrontal areas where poor BOLD SNR reduces detectability. These results may also be partially attributable to the broader range of contributing frequencies for ASL-FC than BOLD-FC. As with seed-based analysis, ASL-ICA identified major networks described in the BOLD literature, both RSNs from task-free fMRI and co-activation networks from task-based fMRI.

	ICA vs. RSNs from Smith et al.		**ICA vs. BrainMap activation networks**		**ICA vs. RSNs from Yeo et al.**	
	ASL	**BOLD**	**ASL**	**BOLD**	**ASL**	**BOLD**
DMN	0.55	0.45	0.36	0.26	0.44	0.36
VN	0.55	0.58	0.57	0.52	0.59	0.47
SMN	0.70	0.38	0.56	0.33	0.41	0.26
SN	0.22	0.34	n/a	n/a	0.15	0.28
CEN	0.42	0.34	0.36	0.19	0.44	0.31
Mean± standard deviation	0.49±0.18	0.42±0.10	0.46±0.12	0.33±0.14	0.41±0.16	0.34±0.08

Table 6. Independent component analysis group-level Dice scores vs Smith et al. RSNs, BrainMap activation networks from Smith et al., and Yeo et al. RSNs. These results indicate that ASL-FC with proper preprocessing can describe canonical brain networks at accurately as BOLD-FC at the group level.

ASL-FC was first proposed by Biswal et al. in 1997, but it remains relatively understudied. While CBF fluctuations from ASL correlate in the SMN (Chuang et al., 2008) and DMN (Zou et al., 2009), most previous studies have not taken advantage of both high-efficiency labeling and volumetric readouts, suggesting that gains in image quality and network sensitivity are achievable with recent perfusion imaging developments; such as pseudocontinuous labeling, background suppression (Maleki et al., 2012), and 3D readouts; which collectively increase SNR multi-fold and enable individual measurements to be used for connectivity analysis. Jann et al. (2013, 2015) utilized pCASL-based ICA to demonstrate that networks derived from ASL and BOLD were spatially similar, while Li et al. (2018) found that ASL-FC from pCASL with single-shot readout and BOLD-FC were similar in many RSNs. Likewise, Dai et al. (2016) found that pCASL-ICA produced fewer spurious, non-neural components than BOLD-ICA. These findings suggest that ASL-FC is reliable and offers unique advantages compared to typical methods. However, image analysis approaches have differed extensively, demonstrating the need for systematic development of analytic procedures tailored for ASL-FC.

Importantly, it cannot be assumed that a single preprocessing strategy will result in optimal detection of all RSNs. Heterogeneous results could be attributable to differences in vascular density and blood arrival times between RSNs (e.g., RSNs perfused by posterior circulation vs. anterior circulation, which have differences in arrival time of 200-500 ms). Thus, we synthesized the most advantageous approaches from individual networks into a generally applicable method, and showed that this produced improvements for all group-level RSNs (**Fig. 4-3**). Of these, spatial smoothing produced improvement in the greatest number of networks. This smoothing is applied in addition to blurring already present in the 3D GRASE readout, which we calculated as FWHM=7.8 mm from T_2 effects in the z-direction, using the formula PSF (FWHM)=$\frac{\sqrt{3}}{\pi}\Delta x\frac{T_s}{T_2}$, with the spatial resolution Δx=3.8 mm, readout duration T_s=300 ms, and gray matter parenchyma T_2=80 ms (Haacke et al., 1999, eq. 13.65). In our preprocessing Gaussian smoothing was applied equally in three dimensions, but the impact of smoothing in orthogonal directions may vary slightly owing to the differing effects of blurring from the readout combined with smoothing from the spherical Gaussian kernel.

For completeness, we performed ASL preprocessing using several strategies common in BOLD-FC, including some which proved ineffective for ASL. Motion regression may be less relevant to ASL-FC because some effects of gradual head movements will be cancelled by image subtraction.

GSR does not remove as much spurious non-neural signal from ASL as from BOLD, since this contrast originates mainly in gray matter. While the ASL signal is dominated by gray matter perfusion signal due to the longer arrival times and lower perfusion in white matter, white matter as well as CSF can still contribute noise to the final perfusion-weighted image. Partial voluming effects from white matter and CSF may also variably contribute, especially given the large voxel volumes used in typical ASL acquisitions (3-5 mm). Global signal is a major source of structured noise in ASL (Dai et al., 2016), and its removal has been shown to increase temporal SNR of ASL and test-retest reliability in CBF measurement (Wang, 2012) However, CBF quantification and ASL-FC depend on different parameters: the mean of the ASL signal, and its temporal variance, respectively. Therefore, it is not entirely clear from these data how GSR may influence ASL-FC.

Finally, low-pass frequency filtering was generally ineffective at both 0.05 and 0.10 Hz, likely because ASL-FC depends on a broad and consistent frequency regime as seen in power spectrum results. The effective sampling rate for ASL was 0.128 Hz, and hence 0.064 Hz is the upper limit of signal detection per the Nyquist theorem. However, bandpass filtering will still smooth the MRI time series at frequencies above this limit, and so high-pass filtering even at 0.10 Hz may affect the resulting correlation-dependent RSN maps.

Detection also depended on the use of seed-based or data-driven approaches. For instance, SMN detection was inaccurate in the seed-based analysis (**Fig. 4-4C**), but comparable to BOLD in ICA (**Fig. 4-7C**). Group-level ASL-ICA approximated results derived from two highly-cited studies, Smith et al. and Yeo et al., which used 30,000 activation fMRI datasets and 1,000 resting-state fMRI datasets, respectively. ASL-FC recapitulated these canonical RSNs with fidelity comparable to, or slightly better than, our BOLD-FC pipeline, indicating that ASL-ICA is a promising approach to describing the architecture of intrinsically connected networks.

We also demonstrate that ASL-FC and BOLD-FC produce RSNs with systematic spatial differences. While RSNs from the two modalities should have some degree of correspondence, discrepancies may also represent detection of different physiological information. We note that ASL RSNs typically localized nearer to the gray matter ribbon than BOLD RSNs. This may reflect network activity localized to the capillaries rather than venous vasculature, and therefore ASL-FC may more closely co-localize with regions of metabolic activity. For example, the prefrontal node of the DMN was located closer to the frontal pole of the brain in the preprocessed ASL RSN, possibly due to lower signal contribution from the anterior cerebral veins and more general venous pooling that may contribute to BOLD RSNs (**Fig. 4-4A**). Similarly, the ASL-derived VN featured less extension into the precuneus and posterior cingulate, potentially due to reduced contribution from posterior-circulation draining vasculature such as the straight sinus and inferior sagittal sinus (**Fig. 4-4B**).

ASL is also less affected by susceptibility artifact due to the comparatively short echo time, an effect reduced further when spin echo rather than gradient echo readouts are used. Consequently, signal is higher in regions near air-tissue boundaries, such as the orbitofrontal cortex. This is evident in the medial-frontal node of the SN, which extends markedly further into the ventral-most part of the frontal cortex (**Fig. 4-4D**). Detection of such novel spatial features in known RSNs may motivate future ASL-FC studies, especially in these functionally eloquent regions. The orbitofrontal cortex is critical for a variety of reward-processing and decision-making processes, yet this network remains incompletely characterized from existing BOLD methods.

These results should be interpreted in the context of limitations in imaging method and study design. First, even with recent improvements, SNR in ASL is low compared to BOLD, as CBF-related image intensity difference is 1-2% of equilibrium signal intensity. This may decrease sensitivity to correlated neural activity fluctuations, although SNR can be improved 2-4 fold with 3D readouts such as GRASE (Petersen et al., 2017) or stack of spirals (Dai et al., 2016; Vidorreta et al., 2017), and with pCASL labeling and background suppression (Gunther et al., 2005; Oshio and Feinberg, 1991). Correspondingly, subject-level ASL reproducibility was relatively low. This finding is consistent with (Jann et al., 2013), who measured lower between-session and between-scanner reproducibility for ASL than BOLD. Therefore, ASL-FC in its present state may be most useful at the group level. Future work may increase our sample of healthy subjects to further refine group-level network identification.

Second, ASL also has lower temporal resolution than BOLD, with a TR of 3500-4000 ms for pCASL. However, ASL-FC can access temporal dynamics inaccessible to BOLD-FC, including very low frequencies removed by baseline drift correction (less than 0.01 Hz) (**Fig. 4-5**). Future work may focus on understanding the physiological and functional origins of very-low-frequency connectivity, expanding our understanding of the time-scales on which distant brain regions communicate. It is also important to note that the recommended parameters for perfusion imaging from the ISMRM perfusion study group, which call for a segmented 3D GRASE readout, result in a temporal resolution too low for robust RSN detection (approximately 16s). Therefore, this work extends information provided in the white paper to provide parameter and post-processing suggestions when RSN detection is of interest.

Third, scan order was not completely randomized; ASL preceded BOLD for 80% of scan sessions. Physiological monitoring in a subset of participants showed no evidence in support of differences in cardiac or respiratory frequencies between first and second scans, suggesting that habituation to the scan environment is likely not a major confound. Further, recent work has shown that effects of the cardiac cycle on pCASL signal stability are minimal (Verbree and van Osch, 2018). As such, we do not believe that this is a major confound in our data. However, it should be noted that in dynamic acquisitions such as ASL-FC where each image is of interest (i.e., rather than a time-averaged CBF-weighted composite map), these effects may contribute differently to the network detection and therefore future work that extends cardiac gating to ASL-FC studies may be warranted.

Finally, while short-to-intermediate TE 3D GRASE ASL is less sensitive to susceptibility effects than conventional longer-TE gradient echo BOLD, some residual T_2* and T_2 effects are nonetheless possible. However, since ASL-FC analysis performed on unlabeled images resulted in lower spatial consistency with BOLD-FC for four of five tested networks, we believe that this effect is unlikely to be the major contributor to ASL network contrast reported in this study.

Despite these limitations, our results demonstrate the ability to visualize canonical RSNs from ASL-FC data and to measure connectivity in regions prone to poor SNR in conventional

BOLD acquisitions. Future studies that address the above limitations are needed, however, and if successful should improve network detection fidelity further.

4.7 Conclusions

We demonstrated that ASL-FC, including seed-based and ICA approaches, provides novel insights into the spatial and temporal features of functionally connected brain networks inaccessible to traditional methods. ASL-FC benefits from several denoising strategies, which produce improvements in network detection. While preprocessing of ASL-FC can improve spatial coherence between RSNs derived from ASL and BOLD, areas of difference between the two modalities may also reflect meaningful physiological phenomena, such as contrast compartmentalization to different vascular sources (e.g., capillary vs. venular) or distinct frequency information. One area of potential application is mapping the connectivity of regions that are problematic in BOLD imaging due to susceptibility-weighted image dropout, such as the orbitofrontal cortex, a functionally important region involved in the processing of reward, decision-making, and executive function, or the dentate nucleus, a key hub in motor and non-motor cerebellar feedback pathways.

CHAPTER 5

ARTERIAL SPIN LABELING REVEALS MEDIAL-LATERAL DIVISION IN ORBITOFRONTAL CORTEX CONNECTIVITY

5.1 Purpose

The previous chapter established that ASL-FC can identify canonical resting-state networks serving critical neural roles, and describe novel spatial and temporal features of such systems. This recently developed technique offers the potential to investigate regions that are problematic for BOLD fMRI approaches, providing insights into areas with high magnetic susceptibility and distortion or large draining veins. An important region with relatively poor image quality in traditional functional neuroimaging is the ventral frontal cortex, particularly the orbitofrontal cortex (OFC) near the ventral striatum, insula, and subgenual anterior cingulate gyrus. This zone is especially relevant to behavioral dysfunctions of reward valuation and aberrant learning. It is a site with strong dopaminergic connectivity, including direct projections to and from the ventral striatum/nucleus accumbens. In Chapter 2, we described elevated functional connectivity between the OFC and ventral striatum, part of a larger pattern of increased synchrony between limbic frontal cortex and the basal ganglia. However, a more complete understanding of OFC connectivity is necessary before these broad findings can be fully interpreted. This necessitates the application of novel perfusion-based connectivity methods to determine the constituent sub-regions of the OFC, a functionally diverse section of the frontal lobe.

5.2 Summary

The orbitofrontal cortex (OFC) is involved in reinforcement learning, decision-making, valuation of stimuli, and subjective pleasure. Subdivisions of the OFC are based on anatomy and cytoarchitectonics, but connectivity-based parcellations have also been proposed. To date, attempts to describe OFC functional connectivity have been limited by a severe signal dropout artifact in T_2*-weighted blood oxygenation level-dependent (BOLD) fMRI due to high susceptibility in the lower frontal lobe.

Here, an alternative approach is utilized to describe OFC connectivity and test the hypothesis that this region is divided into two major zones: a medial-caudal region and a lateral-orbital one. Arterial spin labeling (ASL) is an MRI technique to noninvasively measure cerebral blood flow, and can provide fMRI contrast. In healthy subjects (n=20), 20-minute resting-state ASL scans (TR/TE=3900/13 ms; spatial resolution=3.8 mm isotropic) were acquired. ASL was used to conduct seed-based connectivity analysis at every gray matter OFC voxel, and k-means clustering was applied to group the voxels based on their connectivity with all brain regions excluding the OFC itself. This approach bifurcated the OFC into two clusters, one combining medial and caudolateral zones, and one located in more anterior, orbital regions, confirming our hypothesis. These clusters correspond to results of previous meta-analyses of functional activations and more broadly with morphological divisions. Connectivity of the clusters was quantified; the medial cluster was most strongly associated with the ventromedial prefrontal cortex and insula, approximating the salience network, while the lateral cluster was associated with regions of dorsolateral prefrontal and parietal cortex.

These functional connectivity findings suggest an underlying structural connectivity difference between the two regions. We tested this hypothesis using tractography in high-resolution diffusion-weighted imaging from the Human Connectome Project, and results confirmed the major hypothesis, with the medial OFC more structurally connected to ventromedial prefrontal cortex and insula. Medial-lateral differences in structural connectivity were found to correlated with differences in functional connectivity. This study provides the first *in vivo* evidence for the functional subdivision of a high-susceptibility frontal region on the basis of blood perfusion dynamics, and confirms a long-standing hypothesis in orbitofrontal neuroanatomy.

5.3 Introduction

The orbitofrontal cortex (OFC) occupies the ventral surface of the brain's frontal lobe. Its best-described functions are integration of sensory information with reward circuitry, and monitoring the values of environmental stimuli in the context of learning and decision-making (Kringelbach, 2005). The OFC is extensively connected with the limbic system, including the ventral striatum/nucleus accumbens and the amygdala (Barbas and Zikopoulos, 2010). The OFC also receives convergent sensory information from olfactory, gustatory, and somatosensory cortex (Rolls, 2002). Its position at the nexus of cognitive processing, affective function, and sensory integration enables the OFC to mediate behavioral responding to environmental stimuli. The most frequently described function of the OFC is to encode the value or expected value of reinforcers by linking sensory processes to limbic circuits. The OFC and the anatomically proximate anterior cingulate cortex participate in limbic loops modulating feedback between cortex and basal ganglia (Alexander et al., 1986).

Functionally, evidence from meta-analysis of fMRI studies suggests that the OFC is divisible into a medial-caudolateral network, termed 'medial OFC', and a lateral-orbital network termed 'lateral OFC'. These subdivisions are thought to perform different roles in decision-making, with medial OFC attuned to positive reinforcers or rewarding stimuli, and lateral OFC more responsive to negative reinforcers and punishment stimuli (Kringelbach, 2005). An anterior-posterior gradient is also proposed, with more posterior regions responding to simpler primary rewards such as food, and anterior regions to more abstract, indirect reinforcers (Sescousse et al., 2013). Posterior OFC has more extensive connectivity with the amygdala, and is believed to modulate autonomic responding in a manner sensitive to dopamine levels (Zikopoulos et al., 2017). However, most OFC connectivity data are derived from anatomical studies using primate models, post-mortem human tissue histology, or *in vivo* diffusion tractography. The functional connectivity of the OFC remains poorly understood because the limbic cortex, particularly the caudal OFC, is subject to a profound signal dropout due to magnetic field inhomogeneity induced by air-tissue interfaces in the sinuses (Deichmann et al., 2002). Therefore, the signal-to-noise ratio in traditional BOLD fMRI sequences is very low compared to surrounding cortical regions.

Thus, a novel method is needed to accurately measure functional connectivity between the OFC and the rest of the brain. Arterial spin labeling (ASL) is a noninvasive MRI technique weighted to measure cerebral blood flow (CBF). ASL reflects neural activity in the underlying tissue, and scales linearly with glucose metabolism (Musiek et al., 2012). Due to shorter echo times, ASL is less susceptibility-weighted and therefore less vulnerable to signal dropout in high-susceptibility regions such as the OFC, the cerebellar dentate nucleus, and the temporal lobes adjacent to the aural canals. ASL is a novel but promising alternative contrast for functional connectivity, as its signal source is more weighted toward capillary than venous vasculature. In the previous chapter it was shown that ASL-based functional connectivity (ASL-FC) can recapitulate brain resting-state networks with fidelity comparable to BOLD-FC after optimized preprocessing.

Here, we utilize this method to examine the functional connectivity of the OFC and test the hypothesis that it contains distinct medial-caudal and lateral-orbital sub-regions. We employ a clustering-based parcellation method similar to that described in (Kahnt et al., 2012). Clustering-based parcellation of resting-state MRI data is an established technique to identify discrete cortical zones based on their connectivity profiles. Unsupervised clustering techniques have been used to define networks spanning the whole brain (A. L. Cohen et al., 2008) as well as in specific regions, such as Broca's area (Kelly et al., 2010), the supplementary motor area (Kim et al., 2010), insula (Cauda et al., 2011; Deen et al., 2011; Nelson et al., 2010), precuneus (Zhang and Li, 2012), and amygdala (Mishra et al., 2014). Functional connectivity-based parcellation was recently reviewed by (Eickhoff et al., 2015).

5.4 Methods

Image acquisition protocols for this work are described in the previous chapter. Functional connectivity was performed using ASL-FC, which we have shown is useful for detecting RSNs in both brain regions with high signal-to-noise ratio and those with high susceptibility artifacts. Briefly, healthy participants (n=20; age=29.5±7.3 years, sex=10M/10F) underwent 20-minute resting-state pseudo-continuous ASL scans (TR/TE=3900/13 ms, post-labeling delay=1800 ms, label duration=1800 ms, field-of-view=80x80x25, spatial resolution=3.8 mm isotropic) with 3D GRASE readout. Structural connectivity was measured using fiber tractography in Human Connectome Project data using methods similar to those described in Chapter 3.

For an overview of the strategy applied here, see **Fig. 5-1.** Image processing and data analysis were performed using the FMRIB Software Library (FSL) (Smith et al., 2004) and custom Matlab scripts (Mathworks, Natick MA). The OFC was drawn on axial slices of the T_1-weighted images. The region extended in the rostral-caudal direction from the frontal pole to the anterior boundary of the insula at its separation from the temporal lope. In the inferior-superior direction it extended from the lowest extent of the frontal lobe to no higher than the bottom of the corpus collosum genu. FAST was then used to segment the T_1-weighted image into gray and white matter; white matter voxels were excluded from the OFC mask. T_1-weighted images were linearly registered to the mean ASL image using FLIRT, and the OFC binary mask was then transferred to ASL space using the same affine transformation matrix.

ASL images were motion-corrected using MCFLIRT. Surround subtraction was applied: each spin-labeled image was subtracted from the mean of the preceding and following unlabeled images. This method was preferable to simple paired subtraction because it reduces frame-to-frame variability and residual BOLD effects (Lu et al., 2006), and has been shown to improve resting-

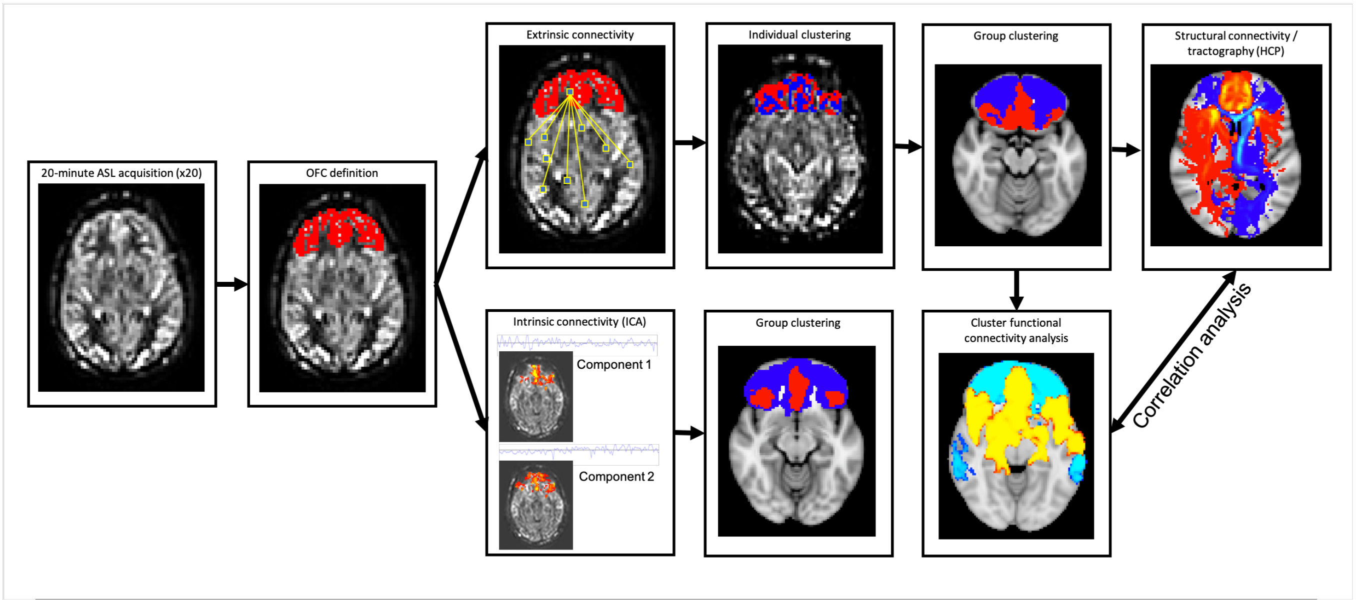

Fig. 5-1. Orbitofrontal cortex connectivity study design. 20 resting-state ASL scans were acquired in healthy subjects. OFC masks were hand-drawn, and white matter voxels were defined by FSL-FIRST and removed. The OFC was parcellated both on the basis of extrinsic seed-based connectivity (top) and intrinsic independent component analysis (bottom). Both of these results were used for separate group-level clustering using k-means algorithms. The functional connectivity (top-right) and structural connectivity (bottom-right) of the resulting clusters was then mapped and compared. Functional connectivity of the clusters was derived from the ASL-FC data used to define those clusters. Structural connectivity (tractography) analysis was performed using Human Connectome Project diffusion-weighted data. Structural and functional results were correlated against one another. This figure is a schematic of the study design and not intended to directly reflect results.

state network identification (Chapter 4). Global signal regression was applied to remove whole-brain signals, as these can outweigh the effects of the subtle local fluctuations needed for separation of spatially proximate signal sources. ASL data were smoothed using a full width at half-maximum (FWHM)=5-mm Gaussian kernel.

Functional connectivity analysis for OFC parcellation was then performed using two complementary methods with mutually exclusive input data. First, functional connectivity was performed on the basis of *extrinsic* connectivity of OFC voxels with non-OFC brain regions, and clustering analysis was applied to these results. Second, parcellation was performed using independent components analysis of only *intrinsic* OFC connectivity, i.e. between voxels inside the OFC gray matter, omitting non-OFC areas. This pairing of methods was used to ensure that results were not due to the particular features of one approach, and to demonstrate that physiologically distinct sub-regions are identifiable on the basis both of internally similar activity patterns, and congruent connections with the rest of the brain.

While clustering analysis can produce a connectivity map corresponding to a given cluster, these results cannot be used to test the hypothesis that two clusters have different connectivity, as this would involve circular reasoning or ‘double-dipping,’ since connectivity maps were used to derive the original clusters (Eickhoff et al., 2015). Therefore, a second modality is necessary to test for differences in connectivity. For this purpose, we used structural connectivity in a separate cohort of 91 healthy individuals from the Human Connectome Project (Sotiropoulos et al., 2013). These high-resolution datasets were acquired with multiple b-values and 270 directions, providing precise estimates of the orientation distribution function at each brain voxel.

Extrinsic functional connectivity

Extrinsic functional connectivity analysis was performed using FEAT (Woolrich et al., 2001). A separate functional connectivity analysis was performed using each OFC voxel as a seed region. Thus, for each scan, *n* connectivity maps were generated, where *n* is the number of OFC voxels. These maps were converted to z-statistics using Fisher's transform. For each subject, OFC voxels were clustered on the basis of their connectivity with non-OFC brain voxels. A connectivity matrix of size $[n * (b\text{-}n)]$ was constructed, where b is the total number of voxels in the brain. k-means clustering with k=2 was performed to decompose the OFC into two spatial clusters.

Next, the resulting clusters were transferred to subject T_1-weighted images using the inverse affine matrix, and normalized to the 2-mm MNI152 brain by nonlinearly warping the T_1-weighted image using FNIRT. To produce group-level results, MNI-space single-subject clusters were used as inputs in group-level k-means clustering. The resulting clusters constituted the group-level OFC parcellation.

Next, the connectivity patterns between the clusters and the rest of the brain were determined. Group-level medial and lateral clusters were back-transformed from MNI space to each subject native space using the inverse warps. Native-space medial and lateral clusters were then used as seed regions in FEAT to determine the connectivity of the whole cluster. Thus, for each scan, a single medial OFC and single lateral OFC connectivity map was created. Finally, medial and lateral connectivity maps from subject-level clusters were normalized to MNI space and input into a one-sample permutation test using Randomise with 500 permutations and threshold-free cluster enhancement (Smith and Nichols, 2009) to produce final composite group-level connectivity maps. It is important to note that this analysis describes the connectivity pattern corresponding to each cluster, but should not be treated as a statistical *comparison* between clusters.

Intrinsic functional connectivity

Functional connectivity within the OFC was calculated on ASL series using independent component analysis with FSL's MELODIC tool. ASL images were multiplied by the OFC gray matter binary mask to exclude all voxels outside this region. MELODIC decomposed each image into two independent components, whose spatial maps were then transformed to MNI space using the T_1-weighted image as a registration intermediate. Finally, group-level clusters were generated using second-order clustering as described for the extrinsic connectivity analysis above.

Structural connectivity

Structural connectivity was performed using probabilistic tractography in FSL's fiber-tracking program 'Fdt' (Behrens et al., 2007, 2003). Probabilistic tractography allows a statistical comparison of the differential connectivity of a seed to various target regions. Diffusion parameters at each voxel were modeled with 'bedpostx,' which uses Bayesian estimation to build the voxelwise orientation distributions. Fiber-tracking was performed with 'probtrackx2' using the group-level medial and lateral OFC clusters as seed regions. Step length was set at 0.5 mm, and a curvature threshold of 0.2 was used to exclude streamlines with sharp bends. 300 streamlines were calculated per tract, per subject. To determine whether significant differences in structural connectivity exist between the medial and lateral clusters, paired permutation tests were performed using Randomise with threshold-free cluster enhancement and correction for multiple comparisons.

Functional vs. structural connectivity

To determine if differences between the functional networks that defined the medial and lateral OFC clusters were related to the structural connectivity in those same clusters, the difference of connectivity with the medial and lateral OFC for all non-OFC voxels was taken. For functional connectivity, we calculated the difference in connectivity z-score with the medial and lateral OFC, while for structural connectivity, we calculated the difference between the number of streamlines arriving from the medial vs. lateral OFC. Across all non-OFC brain voxels, these were correlated in a Spearman's rank test to mitigate outlier effects.

5.5 Results

Extrinsic functional connectivity

Clustering analysis resulted in the identification of two major OFC subdivisions. A medial cluster included the straight gyrus and orbital medial gyrus and the caudal parts of the OFC. A lateral OFC cluster consisted of the areas anterior to the orbital sulcus (**Fig. 5-2A**).

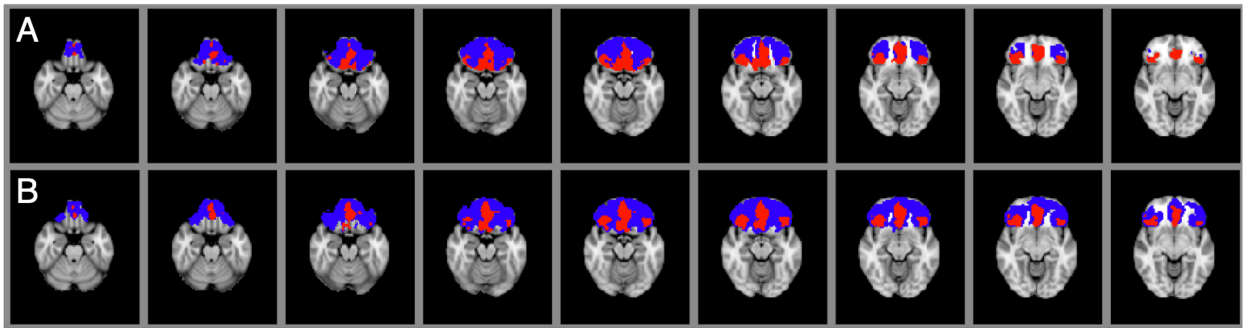

Fig. 5-2. Orbitofrontal cortex clustering results. (A) Orbitofrontal clusters derived from extrinsic perfusion-based functional connectivity. Red cluster corresponds to medial OFC, blue cluster to lateral OFC. (B) Orbitofrontal clusters derived from intrinsic perfusion-based functional connectivity analysis. Red cluster corresponds to medial OFC, blue cluster to lateral OFC.

Intrinsic functional connectivity

Results from independent component analysis of voxels within the OFC produced results spatially similar to the extrinsic connectivity analysis: the two group-level components corresponded to medial-caudolateral and lateral-orbital zones similar to those derived from extrinsic connectivity (**Fig. 5-2B**). Therefore, we conclude that two separate approaches to perfusion-based functional connectivity, using different input data but no anatomical priors, produce similar estimates of the most parsimonious division of the OFC.

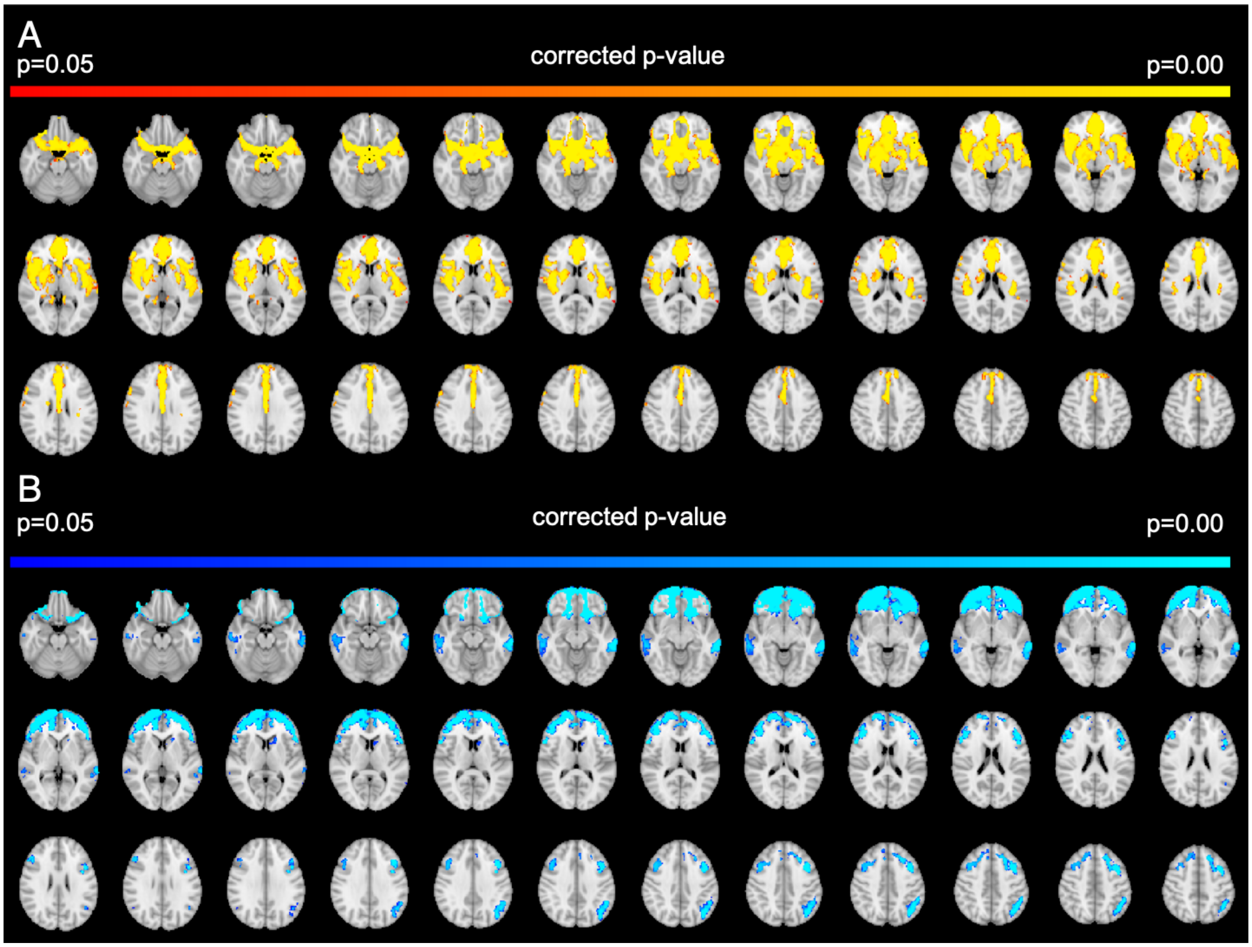

Fig. 5-3. Functional connectivity maps of orbitofrontal clusters. (A) Group-level connectivity for medial OFC. Corrected p-values from a 1-sample permutation test with significance determined clusterwise are displayed. (B) Group-level connectivity for lateral OFC using the same statistical procedure.

Medial and lateral OFC connectivity

The functional networks associated with these two clusters differed spatially. The medial OFC cluster was functionally connected primarily with the ventromedial prefrontal cortex as well as the bilateral insular cortex (**Fig. 5-3A**). The lateral OFC cluster connected with a broader region of frontal and parietal cortex (**Fig. 5-3B**).

Tractography-based structural connectivity using Human Connectome Project data also indicated differing connectivity of medial and lateral clusters. The medial OFC cluster was structurally connected with regions associated with the salience network, including ventromedial

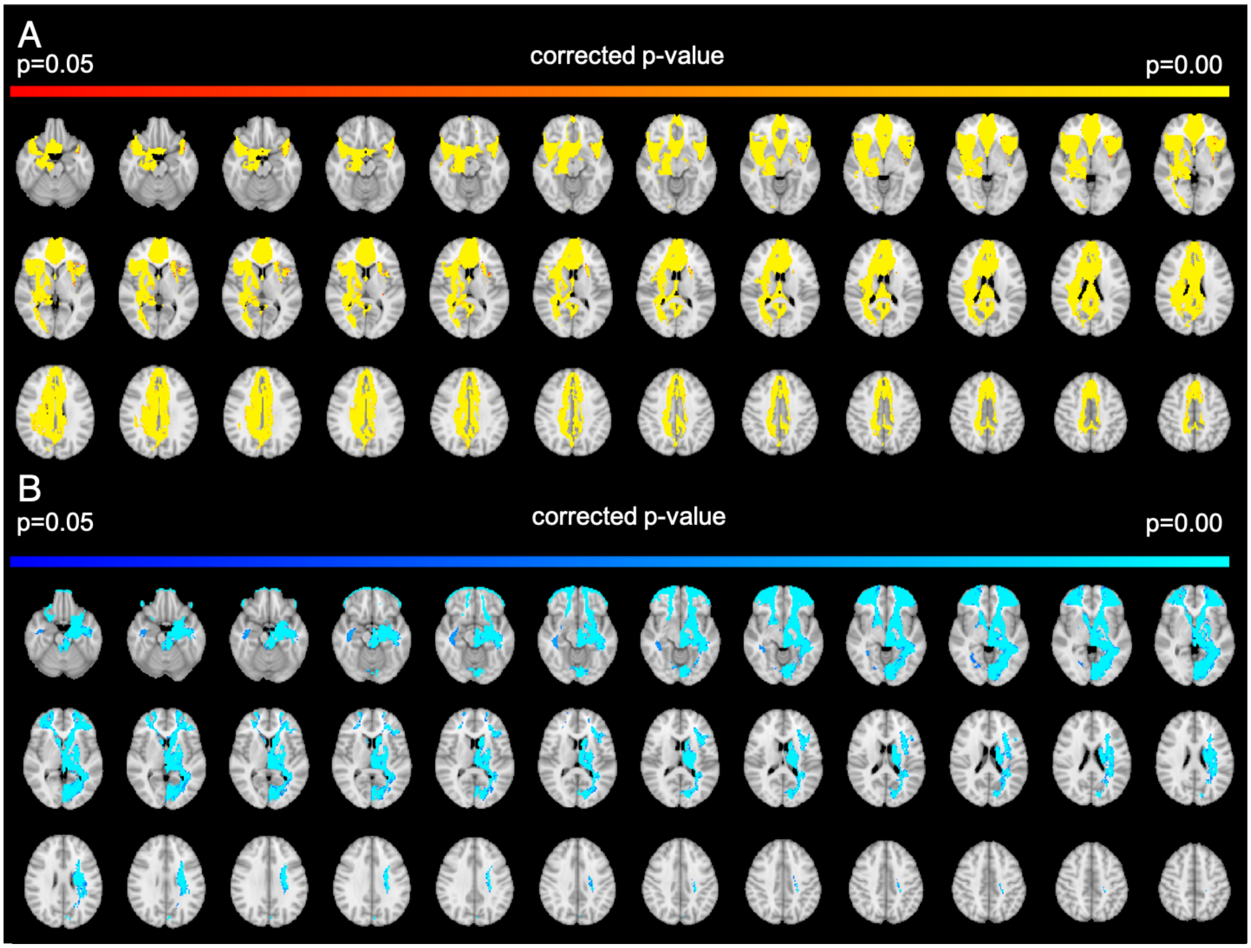

Fig. 5-4. Structural connectivity differences between orbitofrontal clusters. (A) Regions of greater structural connectivity with medial OFC than lateral OFC. Corrected p-values from a 2-sample permutation test with significance determined clusterwise are displayed. (B) Regions of greater structural connectivity for lateral OFC than medial OFC created using the same statistical procedure.

prefrontal cortex and bilateral insular cortex, results similar to the functional connectivity analysis (**Fig. 5-4A**). The lateral OFC cluster connected with a broader region of frontal and parietal cortex (**Fig. 5-4B**). The apparent laterality seen here, with lateral OFC seeming to have greater connections with left-sided structures, is likely due to slight asymmetries in the seed clusters and potentially artifactual.

Across all non-OFC brain voxels, the difference in functional connectivity between medial and lateral OFC was significantly correlated with the difference in structural connectivity between medial and lateral OFC (Spearman's rho=0.20, p<0.001) (**Fig. 5-5**).

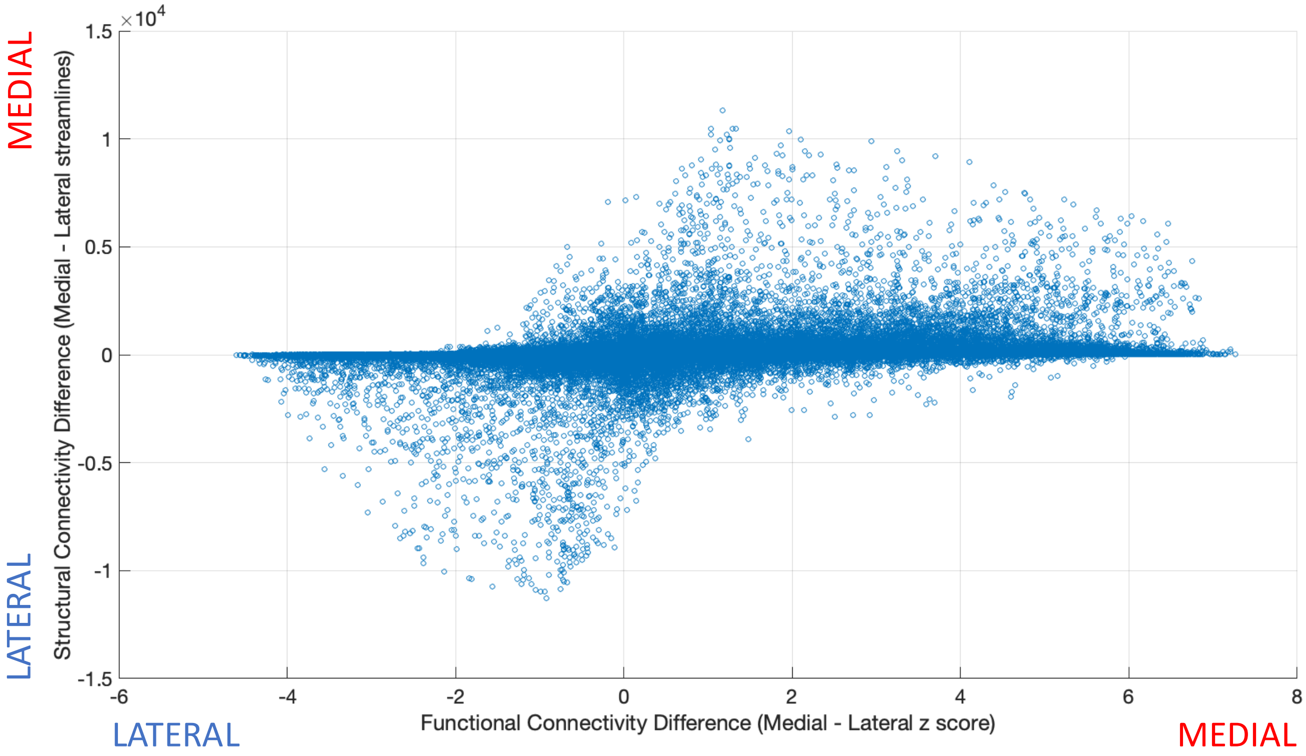

Fig. 5-5. Functional vs. structural orbitofrontal connectivity. Medial-lateral differences in structural vs. functional connectivity across all standard-space brain voxels outside the OFC. X-axis represents functional connectivity z-score differences between medial and lateral OFC connectivity with a given voxel. Y-axis represents structural connectivity streamline count differences between medial and lateral OFC connectivity.

5.6 Discussion

In this study, we found that multiple functional connectivity methods can parcellate the human OFC on the basis of resting-state perfusion fluctuations, and that independent extrinsic and intrinsic connectivity methods yield highly congruent results. We utilized data-driven clustering analysis to subdivide the OFC, meaning that no anatomical priors were incorporated in the clustering algorithm. Both extrinsic and intrinsic functional connectivity identified two major clusters corresponding to separable medial and lateral zones, confirming our major hypothesis. The connectivity of these clusters with the rest of the brain was determined, demonstrating that the medial cluster is defined by high connectivity with components of the ventromedial prefrontal cortex and the bilateral insula, regions corresponding to the well-described salience network (Seeley et al., 2007). The lateral OFC was marked by greater connectivity to symmetrical regions of dorsolateral prefrontal cortex and corresponding nodes in the parietal cortex, matching the definition of the central executive/fronto-parietal network, although the right-sided parietal node fell just short of significance (corrected peak p-value=0.054). We have shown in the previous chapter that both salience and central executive networks are readily identifiable using ASL-FC.

Our results confirm a longstanding hypothesis about the OFC, that the major functional division of this region is into medial and lateral zones. This idea was previously supported by the results of a meta-analysis of activations from fMRI experiments, which used coordinates from task-based fMRI reported in BrainMap (Laird et al., 2005) as a data source for functional connectivity (Zald et al., 2014). This study found that medial and lateral OFC are co-activate with different brain regions, with medial OFC connective with default mode network and limbic regions, and lateral OFC with dorsolateral prefrontal cortex. However, this study defined medial and lateral regions *a priori* rather than using data to determine parcellation.

A second set of findings arguing for functional division of the OFC is derived from the fMRI activations mapped within the OFC itself, a method more similar to our intrinsic connectivity analysis, although using task-based fMRI rather than the resting state. fMRI stimuli associated with rewards tend to produce increased in activity in the medial part of the OFC, while those associated with punishing or aversive stimuli belong to more lateral regions (Kringelbach, 2005). Though simplistic, this distinction is nonetheless powerfully explanatory of the observed data, with very well-defined clusters evident for both positive and negative reinforcement categories.

A third line of evidence for this medial-lateral distinction came from a clustering-based connectivity study which utilized BOLD fMRI to parcellate the OFC using methods similar to our extrinsic connectivity approach. This study also found a broad medial-lateral distinction, although parcellation into more fine-grained nodes was also described (Kahnt et al., 2012). Despite these important findings, this method is limited by the poor signal-to-noise ratio of T_2*-weighted sequences in the ventral frontal cortex.

Finally, existing tractography data provide evidence for medial-lateral OFC separation, with the orbital-lateral region receiving inputs from higher sensory areas and projecting to the lateral striatum, and the medial zone connected more strongly with the hypothalamus and medial PFC (Price, 2010).

Here, we confirm and extend these findings using a novel perfusion-dependent approach to connectivity-based clustering. Results from two different data-driven methods with no anatomical inputs—intrinsic and extrinsic OFC parcellation—confirm the appearance of two main subdivisions, a contiguous one centered on the midline, and one separated between the lateral ventral surfaces of both hemispheres. These clusters are distinguished by their differential connectivity to broader regions of the cerebral cortex. Medial OFC was more was connected with regions generally described as the salience network, including the ventromedial prefrontal cortex and bilateral insula, while the lateral OFC had greater connectivity to the dorsolateral prefrontal cortex, and regions of the parietal lobes corresponding to the fronto-parietal or central executive network.

These findings are confirmed by the use of structural connectivity in a different neuroimaging dataset: high-resolution diffusion-weighted MRI from the Human Connectome Project. Clusters defined by ASL-FC approaches were used to seed tractography, and the resulting structural connectivity maps allowed testing of the hypothesis that the medial and lateral OFC areas belonged to different anatomical networks. The results of structural connectivity were highly similar to functional connectivity, indicating that the observed resting fMRI signal patterns reflected underlying white matter pathways. While the use of a second dataset suggests that connectivity results are generalizable beyond the perfusion images acquired for this study, this approach also presents a potential limitation, as it only permits structure-function comparison at the group level rather than within the same subject. Therefore, it would be enlightening to obtain both long-acquisition perfusion scans and high-resolution diffusion-weighted imaging in the same participants, whether healthy individuals or persons with altered OFC connectivity due to conditions such as Parkinson's disease-related impulsive-compulsive behaviors.

Another important point is that the medial OFC network described here and the extended salience network of Chapter 4 correspond closely with regions of relatively high perfusion and short blood bolus arrival time (Donahue et al., 2014). This suggests a potential confounding effect, where different perfusion properties of these areas may partially account for their apparent synchrony. However, differences in bolus arrival times are much shorter than the time scales contributing to our ASL-FC results, less than one TR in our imaging sequence. Arrival time varies by about 0.7 s from shortest to longest, and is thus not likely to account for the longer synchrony effects described here. It is possible that the medial OFC and its network are indeed served by different vasculature than the lateral network, which could partly explain their functional separation from lateral OFC, alongside their white matter connections. Future studies will examine variable blood arrival times and mean perfusion rates in these networks.

5.7 Conclusions

While these results support the conclusions of previous imaging and anatomical studies, they also provide new insights into the structure and function of the OFC. We have utilized a novel modality: connectivity-based clustering of perfusion-weighted MRI, which has several advantages for OFC imaging and functional connectivity analysis, including low susceptibility, less venous bias, and a more quantitative relationship between signal and neural activity. The appearance of the same two major clusters using both extrinsic and intrinsic connectivity and a novel ASL-based parcellation approach is strong evidence in support of the validity of the long-debated concept that the OFC is primarily divisible into medial and lateral regions. Moreover, the parallel use of diffusion tractography in a large, well-validated dataset of healthy controls, the Human Connectome Project, argues that these clusters represent divisions of the underlying neural architecture.

CHAPTER 6

CONCLUSIONS AND FUTURE DIRECTIONS

Taken together, these experiments demonstrate the utility of structural and functional approaches to brain network mapping.

Reward-incentivized impulsive and compulsive behaviors (ICBs) are linked with fMRI synchrony in the mesocorticolimbic network. In Chapter 2, connectivity in pathways between the basal ganglia and ventral frontal cortex was shown to reflect learning of reinforced cue associations. This suggests a mechanism by which increased ventral striatal connectivity in PD patients with ICBs leads to heightened reward sensitivity, and to altered behavior. This network effect is potentially caused by ICB-linked differences in the ventral striatum itself. Individuals with ICBs have an altered pharmacological profile in the nucleus accumbens, with reduced D_2/D_3 receptor availability (Stark et al., 2018a) and abnormal hemodynamic properties. Greater ventral striatal blood flow changes after dopaminergic therapy indicate enhanced neural responses to dopamine agonists in the ICB+ population (Claassen et al., 2017).

Future studies of mesocorticolimbic connectivity should focus on the specific roles of single regions of frontal associative cortex. While we observed increased functional connectivity with the orbitofrontal cortex, insula, and anterior cingulate gyrus, separate contributions of these components remain undetermined. Moreover, while these regions all participate in reinforced learning and reward-motivated decision-making, the conclusions described here do not discriminate among their constituent sub-regions, which may profoundly differ in function.

In particular, it would be illuminating to identify which of two major orbitofrontal networks is responsible for our finding of elevated connectivity with ventral striatum in ICBs. It is also possible that changes in both medial and lateral OFC are involved in the various impulsive or perseverative behaviors caused by dopamine replacement, since persons with ICBs evince both heightened responses to rewarding stimuli and decreased concern with negative social or economic consequences. Another intriguing question is the relevance of an anterior-posterior gradient in stimulus representation, separating abstract reinforcers from directly rewarding ones (Kouneiher et al., 2009; Kringelbach and Rolls, 2004). As ICBs revolve around a gamut of activities, ranging from hypersexuality to problem gambling, discrete cortico-striatal networks may contribute to distinct ICB types. Alternatively, various ICBs may be manifestations of dysfunction in the same network. Application of ASL-FC methods described in Chapters 4 and 5 will enable quantitative and spatially precise hypothesis testing about ICB-related synchrony changes.

While frontal circuits rely on the basal ganglia to modulate cognitive and behavioral processes, cortico-striatal loops are not the only major feedback system serving the cerebral cortex. The cerebellum performs an analogous role in receiving cortical input, processing signals via intricate multistep computational transforms, and sending reciprocal feedback to the cortex via the thalamus. Like cortico-striatal loops, cerebellar connections also operate in parallel channels, with the same sections of cortex sending afferents to, and receiving efferents from, the cerebellum (Middleton and Strick, 1998). While these arcs are traditionally associated with motor control, increasing evidence also implicates cerebellar loops in a host of nonmotor processes, including learning, executive control, attention, and language (Strick et al., 2009).

The core cerebellar output system is comprised of the white matter fibers of the dentato-rubro-thalamic tract (DRTT), sometimes called the dentato-thalamic tract. The DRTT is the major cerebellar efferent, integrating Purkinje cell input at the deep gray matter dentate nucleus, and sending projections to the thalamus via the superior cerebellar peduncle and red nucleus. Chapter 3 combined structural and functional connectivity to characterize the precise neuroanatomy of its newly described nondecussating (ipsilateral) branch, the nd-DRTT (Meola et al., 2016). These ipsilateral projections target different thalamic sub-regions than the contralateral pathway, suggesting that the two tracts may be functionally differentiable, while still retaining some overlap in communication.

In parallel with tractography, seed-based functional connectivity was used to show linkage between unilateral cerebellar dentate and bilateral thalamus, arguing independently for the existence of ipsilateral DRTT fibers. Across various thalamic sub-nuclei, functional connectivity bias toward ipsilateral and contralateral connectivity correlated with bias in structural connectivity, arguing that results are not limited by the particularities of one analysis method or imaging modality.

Future studies may involve anatomical examination of this tract in postmortem brains of individuals with previously acquired *in vivo* tractography. This approach should include patients with diseases affecting the DRTT, to determine whether physical evidence supports the hypothesis that both d-DRTT and nd-DRTT undergo degeneration in movement disorders such as essential tremor or progressive supranuclear palsy. Our results suggest a possible *in vivo* experiment; in patients with essential tremor and bilateral thalamic DBS leads, inactivation of one side's electrode would ordinarily be expected to disinhibit tremor on the contralateral side. However, our observations of the nd-DRTT implies that effects may be bilateral.

Preliminary evidence in progressive supranuclear palsy also suggests that structural changes in the DRTT are linked to altered functional connectivity between cerebellum and cerebrum, though the functional implications of these changes remain unclear. Future studies should test whether declines in DRTT white matter microstructure are linked with loss of gray matter thickness in sensorimotor cortical regions that receive projections from the cerebellum and DRTT via the thalamus.

While we have shown that conventional connectivity approaches provide insights into both the limbic frontal network and DRTT, novel methods are required to examine more susceptible regions. In Chapter 4, we systematically developed an approach to correlate perfusion fluctuations across the brain. Due to shorter echo times, arterial spin labeling (ASL) is less sensitive to magnetic field inhomogeneity, allowing detection of activity in such areas. ASL allows the *in vivo* measurement of cerebral blood flow, which has a consistent relationship with neuronal energy utilization, and can be used as an alternative fMRI modality. To test this approach, we first examined several well-known sensory, motor, and cognitive brain networks. We demonstrate that canonical RSNs such as the default mode network and sensorimotor network can be delineated from physiological noise with accuracy comparable to conventional BOLD-based, T_2*-weighted scans. We developed an optimized preprocessing pipeline for ASL-FC, and showed that it improved detection accuracy for each of five examined networks. We found that both seed-based approaches and independent component analysis can be utilized for ASL-FC, and that the latter produces RSNs well-matched with networks derived from large sets of resting-state and task-based fMRI.

This work is extended further in Chapter 5 with the application of ASL-FC to the identification of orbitofrontal cortex (OFC) sub-regions. The OFC is critical to regulation of behavior, reward-motivated learning, and decision-making. In Chapter 2 we described the OFC as having increased ventral striatal functional connectivity in ICBs, although that finding is qualified by the presence of major signal artifacts. We hypothesized that the foremost OFC structural/functional division is between medial and lateral regions. To test this proposition, we developed a new approach based on model-free clustering of ASL signal fluctuations. To our knowledge, this was the first study to perform clustering-based parcellation on perfusion-weighted resting-state data.

Based on connectivity of OFC voxels with the cerebral cortex generally, and on the OFC's internal perfusion correlations, we conclude that the hypothesis is confirmed. The medial OFC is more connected with regions corresponding to the salience network, while the lateral OFC has greater connectivity with fronto-parietal regions and central executive network. To confirm this conclusion, we again utilized high-resolution diffusion-weighted images from the Human Connectome Project to perform tractography, building structural connectivity maps of the medial and lateral OFC for comparison with functional connectivity. We found that medial and lateral regions exhibited significantly different structural connectivity, with the former sending more streamlines to ventromedial prefrontal cortex and insula. This confirmed that ASL-FC-derived clusters correspond to divisions of the underlying neuroanatomy.

ASL-FC and BOLD-FC were obtained for this cohort; however, we have not yet compared the results of OFC clustering between the two modalities. While (Kahnt et al., 2012) found a two-cluster OFC solution similar to ours using BOLD-FC, performing this analysis on the same group of subjects will allow a more direct assessment of the similarities and differences between the two methods.

These studies illustrate the importance of multimodal approaches to human brain mapping. The problem of false positives inherent in both functional imaging (due to spurious noise-related correlations) and structural imaging (due to imprecision in tractography) can be substantially ameliorated by checking one method against the other. While functional connectivity can exist absent direct white matter links due to intermediate synapses, the presence of a detectable white matter path between two functionally correlated regions provides at least qualifying evidence that connectivity is non-artifactual. Conversely, fMRI correlation between two regions may help to validate tractographic paths. For example, convergent structural and functional results are illustrated by the ipsilateral branch of the DRTT and its thalamic target. The mutual support of structure and function is also illustrated in the case of OFC parcellation, where a hypothesis generated by functional connectivity was tested and supported using structural tractography on an independent dataset.

Future work in this vein should apply the multimodal imaging methods described here to the study of brain networks in disease states. OFC connectivity should be examined not only in healthy brains, but in the context of dopaminergic dysfunction in PD-related ICBs. Evidence from conventional neuroimaging in Chapter 2 suggests that ventral striatal connectivity with this dopamine-responsive region is increased in patients with ICB; however, the application of ASL-FC might allow this hypothesis to be tested with greater precision.

REFERENCES

Agosta, F., Galantucci, S., Svetel, M., Lukić, M.J., Copetti, M., Davidovic, K., Tomić, A., Spinelli, E.G., Kostić, V.S., Filippi, M., 2014. Clinical, cognitive, and behavioural correlates of white matter damage in progressive supranuclear palsy. J. Neurol. 261, 913–924. https://doi.org/10.1007/s00415-014-7301-3

Alesch, F., Pinter, M.M., Helscher, R.J., Fertl, L., Benabid, A.L., Koos, W.T., 1995. Stimulation of the ventral intermediate thalamic nucleus in tremor dominated Parkinson's disease and essential tremor. Acta Neurochir. (Wien). 136, 75–81. https://doi.org/10.1007/BF01411439

Alexander, G.E., DeLong, M.R., Strick, P.L., 1986. Parallel organization of functionally segregated circuits linking basal ganglia and cortex. Annu. Rev. Neurosci. 9, 357–381. https://doi.org/10.1146/annurev.neuro.9.1.357

Alsop, D.C., Detre, J.A., Golay, X., G??nther, M., Hendrikse, J., Hernandez-Garcia, L., Lu, H., Macintosh, B.J., Parkes, L.M., Smits, M., Van Osch, M.J.P., Wang, D.J.J., Wong, E.C., Zaharchuk, G., 2015. Recommended implementation of arterial spin-labeled Perfusion mri for clinical applications: A consensus of the ISMRM Perfusion Study group and the European consortium for ASL in dementia. Magn. Reson. Med. 73, 102–116. https://doi.org/10.1002/mrm.25197

American Psychiatric Association, 2013. DSM-V, American Journal of Psychiatry. https://doi.org/10.1176/appi.books.9780890425596.744053

Amiez, C., Joseph, J.-P., Procyk, E., 2005. Anterior cingulate error-related activity is modulated by predicted reward. Eur. J. Neurosci. 21, 3447–3452. https://doi.org/10.1111/j.1460-9568.2005.04170.x

Amrani, K., Dykes, R.W., Lamarre, Y., 1996. Bilateral contributions to motor recovery in the monkey following lesions of the deep cerebellar nuclei. Brain Res. 740, 275–284. https://doi.org/10.1016/S0006-8993(96)00899-2

Andersson, J., Jenkinson, M., Smith, S., 2007. Non-linear registration, aka spatial normalisation. FMRIB Technial Report TR07JA2., Oxford Centre for Functional Magnetic Resonance Imaging of the Brain, Department of Clinical Neurology, Oxford University, Oxford, UK. https://doi.org/10.1016/j.neuroimage.2008.10.055

Anthofer, J., Steib, K., Fellner, C., Lange, M., Brawanski, A., Schlaier, J., 2014. The variability of atlas-based targets in relation to surrounding major fibre tracts in thalamic deep brain stimulation. Acta Neurochir. (Wien). 156, 1497–1504. https://doi.org/10.1007/s00701-014-2103-z

Antonini, A., Schwarz, J., Oertel, W.H., Pogarell, O., Leenders, K.L., 1997. Long-term changes of striatal dopamine D2 receptors in patients with Parkinson's disease: A study with positron emission tomography and [11C]raclopride. Mov. Disord. https://doi.org/10.1002/mds.870120107

Aumann, T.D., Horne, M.K., 1996. Ramification and termination of single axons in the cerebellothalamic pathway of the rat. J. Comp. Neurol. 376, 420–430. https://doi.org/10.1002/(SICI)1096-9861(19961216)376:3<420::AID-CNE5>3.0.CO;2-4

Baik, K., Cha, J., Ham, J.H., Baek, G.M., Sunwoo, M.K., Hong, J.Y., Shin, N.Y., Kim, J.S., Lee, J.M., Lee, S.K., Sohn, Y.H., Lee, P.H., 2014. Dopaminergic modulation of resting-state functional connectivity in de novo patients with Parkinson's disease. Hum. Brain Mapp. https://doi.org/10.1002/hbm.22561

Baker, M., Litvan, I., Houlden, H., Adamson, J., Dickson, D., Perez-Tur, J., Hardy, J., Lynch, T., Bigio, E., Hutton, M., 1999. Association of an extended haplotype in the tau gene with progressive supranuclear palsy. Hum. Mol. Genet. 8, 711–715. https://doi.org/10.1093/hmg/8.4.711

Barbas, H., 2010. Prefrontal Cortex: Structure and Anatomy, in: Encyclopedia of Neuroscience. https://doi.org/10.1016/B978-008045046-9.00427-7

Barbas, H., Zikopoulos, B., 2010. Sequential and parallel circuits for emotional processing in primate orbitofrontal cortex, in: The Orbitofrontal Cortex. https://doi.org/10.1093/acprof:oso/9780198565741.003.0004

Beaulieu, C., 2002. The basis of anisotropic water diffusion in the nervous system - A technical review. NMR Biomed. https://doi.org/10.1002/nbm.782

Bechara, A., Damasio, A.R., Damasio, H., Anderson, S.W., 1994. Insensitivity to future consequences following damage to human prefrontal cortex. Cognition. https://doi.org/10.1016/0010-0277(94)90018-3

Bechara, A., Dolan, S., 2002. Decision-making and addiction (part II): Myopia for the future or hypersensitivity to reward? Neuropsychologia. https://doi.org/10.1016/S0028-3932(02)00016-7

Beckmann, C.F., DeLuca, M., Devlin, J.T., Smith, S.M., 2005. Investigations into resting-state connectivity using independent component analysis. Philos. Trans. R. Soc. B Biol. Sci. https://doi.org/10.1098/rstb.2005.1634

Beckmann, C.F., Smith, S.M., 2004. Probabilistic Independent Component Analysis for Functional Magnetic Resonance Imaging. IEEE Trans. Med. Imaging 23, 137–152. https://doi.org/10.1109/TMI.2003.822821

Behrens, T.E.J., Berg, H.J., Jbabdi, S., Rushworth, M.F.S., Woolrich, M.W., 2007. Probabilistic diffusion tractography with multiple fibre orientations: What can we gain? Neuroimage 34, 144–155. https://doi.org/10.1016/j.neuroimage.2006.09.018

Behzadi, Y., Restom, K., Liau, J., Liu, T.T., 2007. A component based noise correction method (CompCor) for BOLD and perfusion based fMRI. Neuroimage 37, 90–101. https://doi.org/10.1016/j.neuroimage.2007.04.042

Benjamini, Y., Hochberg, Y., 1995. Benjamini Y, Hochberg Y. Controlling the false discovery rate: a practical and powerful approach to multiple testing. J. R. Stat. Soc. B 57, 289–300. https://doi.org/10.2307/2346101

Beucke, J.C., Sepulcre, J., Talukdar, T., Linnman, C., Zschenderlein, K., Endrass, T., Kaufmann, C., Kathmann, N., 2013. Abnormally High Degree Connectivity of the Orbitofrontal Cortex in Obsessive-Compulsive Disorder. JAMA Psychiatry 70, 619. https://doi.org/10.1001/jamapsychiatry.2013.173

Biswal, B., Zerrin Yetkin, F., Haughton, V.M., Hyde, J.S., 1995. Functional connectivity in the motor cortex of resting human brain using echo-planar mri. Magn. Reson. Med. 34, 537–541. https://doi.org/10.1002/mrm.1910340409

Biswal, B.B., Kylen, J. Van, Hyde, J.S., 1997. Simultaneous Assessment of Flow and BOLD Signals in Resting - State Functional Connectivity Maps. NMR Biomed 10, 165–170. https://doi.org/10.1002/(SICI)1099-1492(199706/08)10:4/53.0.CO;2-7

Bogacz, R., Gurney, K., 2007. The Basal Ganglia and Cortex Implement Optimal Decision Making Between Alternative Actions. Neural Comput. 19, 442–477. https://doi.org/10.1162/neco.2007.19.2.442

Bossaerts, P., 2010. Risk and risk prediction error signals in anterior insula. Brain Struct. Funct. 214, 645–653. https://doi.org/10.1007/s00429-010-0253-1

Boubela, R.N., Kalcher, K., Huf, W., Seidel, E.M., Derntl, B., Pezawas, L., Našel, C., Moser, E., 2015. FMRI measurements of amygdala activation are confounded by stimulus correlated signal fluctuation in nearby veins draining distant brain regions. Sci. Rep. https://doi.org/10.1038/srep10499

Broca, P.P., 1861. Remarks on the seat of the faculty of articulated language, following an observation of aphemia (loss of speech). Bull. la Société Anat. https://doi.org/52, 281-302

Brodmann, K., 1909. Vergleichende Lokalisationslehre der Grosshirnrinde. J. Nerv. Ment. Dis. https://doi.org/10.1097/00005053-191012000-00013

Bush, G., Luu, P., Posner, M.I., 2000. Cognitive and emotional influences in anterior cingulate cortex. Trends Cogn. Sci. 4, 215–222. https://doi.org/10.1016/S1364-6613(00)01483-2

Buxton, R.B., Uludağ, K., Dubowitz, D.J., Liu, T.T., 2004. Modeling the hemodynamic response to brain activation, in: NeuroImage. https://doi.org/10.1016/j.neuroimage.2004.07.013

Buxton, R.B., Wong, E.C., Frank, L.R., 1998. Dynamics of blood flow and oxygenation changes during brain activation: The balloon model. Magn. Reson. Med. https://doi.org/10.1002/mrm.1910390602

Cador, M., Robbins, T.W., Everitt, B.J., 1989. Involvement of the amygdala in stimulus-reward associations: Interaction with the ventral striatum. Neuroscience 30, 77–86. https://doi.org/10.1016/0306-4522(89)90354-0

Carriere, N., Lopes, R., Defebvre, L., Delmaire, C., Dujardin, K., 2015. Impaired corticostriatal connectivity in impulse control disorders in Parkinson disease. Neurology 84, 2116–2123. https://doi.org/10.1212/WNL.0000000000001619

Cauda, F., D'Agata, F., Sacco, K., Duca, S., Geminiani, G., Vercelli, A., 2011. Functional connectivity of the insula in the resting brain. Neuroimage 55, 8–23.

https://doi.org/10.1016/J.NEUROIMAGE.2010.11.049

Cavada, C., 2002. The Anatomical Connections of the Macaque Monkey Orbitofrontal Cortex. A Review. Cereb. Cortex. https://doi.org/10.1093/cercor/10.3.220

Cerasa, A., Gioia, M.C., Salsone, M., Donzuso, G., Chiriaco, C., Realmuto, S., Nicoletti, A., Bellavia, G., Banco, A., D'amelio, M., Zappia, M., Quattrone, A., 2014. Neurofunctional correlates of attention rehabilitation in Parkinson's disease: An explorative study. Neurol. Sci. https://doi.org/10.1007/s10072-014-1666-z

Chakravorti, S., Morgan, V.L., Trujillo Diaz, P., Wirz Gonzalez, R., Dawant, B.M., 2018. A structural connectivity approach to validate a model-based technique for the segmentation of the pulvinar complex, in: Gimi, B., Krol, A. (Eds.), Medical Imaging 2018: Biomedical Applications in Molecular, Structural, and Functional Imaging. SPIE, p. 28. https://doi.org/10.1117/12.2293685

Cherubini, A., Péran, P., Caltagirone, C., Sabatini, U., Spalletta, G., 2009. Aging of subcortical nuclei: Microstructural, mineralization and atrophy modifications measured in vivo using MRI. Neuroimage 48, 29–36. https://doi.org/10.1016/j.neuroimage.2009.06.035

Cho, S.S., Yoon, E.J., Bang, S.A., Park, H.S., Kim, Y.K., Strafella, A.P., Kim, S.E., 2012. Metabolic changes of cerebrum by repetitive transcranial magnetic stimulation over lateral cerebellum: A study with FDG PET. Cerebellum 11, 739–748. https://doi.org/10.1007/s12311-011-0333-7

Chuang, K.H., van Gelderen, P., Merkle, H., Bodurka, J., Ikonomidou, V.N., Koretsky, A.P., Duyn, J.H., Talagala, S.L., 2008. Mapping resting-state functional connectivity using perfusion MRI. Neuroimage 40, 1595–1605. https://doi.org/10.1016/j.neuroimage.2008.01.006

Chun, M.-H., Chang, M.-C., 2017. Bilateral ataxia after tumor resection in a patient with a unilateral thalamic tumor. Neurol. Asia 22, 85–88.

Claassen, D.O., Stark, A.J., Spears, C.A., Petersen, K.J., van Wouwe, N., Kessler, R., Zald, D., Donahue, M., 2017. Mesocorticolimbic hemodynamic response in Parkinson's disease patients with compulsive behaviors. Mov. Disord.

Claassen, D.O., Stark, A.J., Spears, C.A., Petersen, K.J., van Wouwe, N.C., Kessler, R.M., Zald, D.H., Donahue, M.J., 2017. Mesocorticolimbic hemodynamic response in Parkinson's disease patients with compulsive behaviors. Mov. Disord. https://doi.org/10.1002/mds.27047

Claassen, D.O., van den Wildenberg, W.P.M., Ridderinkhof, K.R., Jessup, C.K., Harrison, M.B., Wooten, G.F., Wylie, S.A., 2011. The risky business of dopamine agonists in Parkinson disease and impulse control disorders. Behav. Neurosci. https://doi.org/10.1037/a0023795

Clark, L., Bechara, A., Damasio, H., Aitken, M.R.F., Sahakian, B.J., Robbins, T.W., 2008. Differential effects of insular and ventromedial prefrontal cortex lesions on risky decision-making. Brain 131, 1311–1322. https://doi.org/10.1093/brain/awn066

Coenen, V.A., Allert, N., Mädler, B., 2011. A role of diffusion tensor imaging fiber tracking in deep brain stimulation surgery: DBS of the dentato-rubro-thalamic tract (drt) for the treatment of therapy-refractory tremor. Acta Neurochir. (Wien). 153, 1579–1585. https://doi.org/10.1007/s00701-011-1036-z

Coenen, V.A., Allert, N., Paus, S., Kronenbürger, M., Urbach, H., Mädler, B., 2014. Modulation of the Cerebello-Thalamo-Cortical network in thalamic deep brain stimulation for tremor: A diffusion tensor imaging study. Neurosurgery 75, 657–669. https://doi.org/10.1227/NEU.0000000000000540

Cohen, A.L., Fair, D.A., Dosenbach, N.U.F., Miezin, F.M., Dierker, D., Van Essen, D.C., Schlaggar, B.L., Petersen, S.E., 2008. Defining functional areas in individual human brains using resting functional connectivity MRI. Neuroimage 41, 45–57. https://doi.org/10.1016/J.NEUROIMAGE.2008.01.066

Cohen, M.X., Elger, C.E., Weber, B., 2008. Amygdala tractography predicts functional connectivity and learning during feedback-guided decision-making. Neuroimage 39, 1396–1407. https://doi.org/10.1016/j.neuroimage.2007.10.004

Cole, D.M., Oei, N.Y.L., Soeter, R.P., Both, S., Van Gerven, J.M.A., Rombouts, S.A.R.B., Beckmann, C.F., 2013. Dopamine-dependent architecture of cortico-subcortical network connectivity. Cereb. Cortex 23, 1509–1516. https://doi.org/10.1093/cercor/bhs136

Cools, R., Barker, R.A., Sahakian, B.J., Robbins, T.W., 2001. Enhanced or Impaired Cognitive Function in Parkinson's Disease as a Function of Dopaminergic Medication and Task Demands. Cereb. Cortex 11, 1136–1143. https://doi.org/10.1093/cercor/11.12.1136

Cools, R., Lewis, S.J.G., Clark, L., Barker, R.A., Robbins, T.W., 2007. L-DOPA Disrupts Activity in the Nucleus Accumbens during Reversal Learning in Parkinson's Disease. Neuropsychopharmacology 32, 180–189. https://doi.org/10.1038/sj.npp.1301153

Cui, S.Z., Li, E.Z., Zang, Y.F., Weng, X.C., Ivry, R., Wang, J.J., 2000. Both sides of human cerebellum involved in preparation and execution of sequential movements. Neuroreport 11, 3849–53. https://doi.org/10.1097/00001756-200011270-00049

Cusack, R., Russell, B., Cox, S.M.L., De Panfilis, C., Schwarzbauer, C., Ansorge, R., 2005. An evaluation of the use of passive shimming to improve frontal sensitivity in fMRI. Neuroimage. https://doi.org/10.1016/j.neuroimage.2004.08.029

Dagher, A., Robbins, T.W., 2009. Personality, Addiction, Dopamine: Insights from Parkinson's

Disease. Neuron 61, 502–510. https://doi.org/10.1016/j.neuron.2009.01.031

Dai, W., Garcia, D., De Bazelaire, C., Alsop, D.C., 2008. Continuous flow-driven inversion for arterial spin labeling using pulsed radio frequency and gradient fields. Magn. Reson. Med. 60, 1488–1497. https://doi.org/10.1002/mrm.21790

Dai, W., Varma, G., Scheidegger, R., Alsop, D.C., 2016. Quantifying fluctuations of resting state networks using arterial spin labeling perfusion MRI. J. Cereb. Blood Flow Metab. 36, 463–473. https://doi.org/10.1177/0271678X15615339

Damoiseaux, J.S., Greicius, M.D., 2009. Greater than the sum of its parts: a review of studies combining structural connectivity and resting-state functional connectivity. Brain Struct. Funct. https://doi.org/10.1007/s00429-009-0208-6

Damoiseaux, J.S., Rombouts, S.A.R.B., Barkhof, F., Scheltens, P., Stam, C.J., Smith, S.M., Beckmann, C.F., 2006. Consistent resting-state networks across healthy subjects. Proc. Natl. Acad. Sci. 103, 13848–13853. https://doi.org/10.1073/pnas.0601417103

Deen, B., Pitskel, N.B., Pelphrey, K.A., 2011. Three Systems of Insular Functional Connectivity Identified with Cluster Analysis. Cereb. Cortex 21, 1498–1506. https://doi.org/10.1093/cercor/bhq186

Deichmann, R., Josephs, O., Hutton, C., Corfield, D.R., Turner, R., 2002. Compensation of Susceptibility-Induced BOLD Sensitivity Losses in Echo-Planar fMRI Imaging. Neuroimage 15, 120–135. https://doi.org/10.1006/nimg.2001.0985

Deistung, A., Stefanescu, M.R., Ernst, T.M., Schlamann, M., Ladd, M.E., Reichenbach, J.R., Timmann, D., 2016. Structural and Functional Magnetic Resonance Imaging of the Cerebellum: Considerations for Assessing Cerebellar Ataxias. Cerebellum. https://doi.org/10.1007/s12311-015-0738-9

Detre, J.A., Leigh, J.S., Williams, D.S., Koretsky, A.P., 1992. Perfusion imaging. Magn. Reson. Med. https://doi.org/10.1002/mrm.1910230106

Dice, L.R., 1945. Measures of the Amount of Ecologic Association Between Species. Ecology 26, 297–302. https://doi.org/10.2307/1932409

Dolan, R.., 2007. The human amygdala and orbital prefrontal cortex in behavioural regulation. Philos. Trans. R. Soc. B Biol. Sci. 362, 787–799. https://doi.org/10.1098/rstb.2007.2088

Donahue, M.J., Faraco, C.C., Strother, M.K., Chappell, M.A., Rane, S., Dethrage, L.M., Hendrikse, J., Siero, J.C.W., 2014. Bolus arrival time and cerebral blood flow responses to hypercarbia. J. Cereb. Blood Flow Metab. https://doi.org/10.1038/jcbfm.2014.81

Donahue, M.J., Hoogduin, H., Van Zijl, P.C.M., Jezzard, P., Luijten, P.R., Hendrikse, J., 2011. Blood oxygenation level-dependent (BOLD) total and extravascular signal changes and $\Delta R2^*$ in human visual cortex at 1.5, 3.0 and 7.0 T. NMR Biomed. 24, 25–34. https://doi.org/10.1002/nbm.1552

Draganski, B., Kherif, F., Kloppel, S., Cook, P.A., Alexander, D.C., Parker, G.J.M., Deichmann, R., Ashburner, J., Frackowiak, R.S.J., 2008. Evidence for Segregated and Integrative Connectivity Patterns in the Human Basal Ganglia. J. Neurosci. https://doi.org/10.1523/jneurosci.1486-08.2008

Dubbelink, K.T.E.O., Schoonheim., M.M., Deijen, J.B., Twisk, J.W.R., Barkhof, F., Berendse, H.W., 2014. Functional connectivity and cognitive decline over 3 years in Parkinson disease. Neurology. https://doi.org/10.1212/WNL.0000000000001020

Duong, T.Q., Yacoub, E., Adriany, G., Hu, X., Uğurbil, K., Kim, S.G., 2003. Microvascular BOLD contribution at 4 and 7 T in the human brain: Gradient-echo and spin-echo fMRI with suppression of blood effects. Magn. Reson. Med. https://doi.org/10.1002/mrm.10472

Dutt, S., Binney, R.J., Heuer, H.W., Luong, P., Attygalle, S., Bhatt, P., Marx, G.A., Elofson, J., Tartaglia, M.C., Litvan, I., McGinnis, S.M., Dickerson, B.C., Kornak, J., Waltzman, D., Voltarelli, L., Schuff, N., Rabinovici, G.D., Kramer, J.H., Jack, C.R., Miller, B.L., Rosen, H.J., Boxer, A.L., 2016. Progression of brain atrophy in PSP and CBS over 6 months and 1 year. Neurology 87, 2016–2025. https://doi.org/10.1212/WNL.0000000000003305

Eickhoff, S.B., Thirion, B., Varoquaux, G., Bzdok, D., 2015. Connectivity-based parcellation: Critique and implications. Hum. Brain Mapp. 36, 4771–4792. https://doi.org/10.1002/hbm.22933

Ellerman, J.M., Flament, D., Kim, S.G., Fu, Q.G., Merkle, H., Ebner, T.J., Ugurbil, K., 1994. Spatial patterns of functional activation of the cerebellum investigated using high field (4 T) MRI. NMR Biomed 7, 63–68. https://doi.org/fmri_Mary M-Converted #89; Used to be #2195

Fenoy, A.J., Schiess, M.C., 2017. Deep Brain Stimulation of the Dentato-Rubro-Thalamic Tract: Outcomes of Direct Targeting for Tremor. Neuromodulation Technol. Neural Interface 20, 429–436. https://doi.org/10.1111/ner.12585

Flood, S., Jansen, J., 1966. The efferent fibres of the cerebellar nuclei and their distribution on the cerebellar peduncles in the cat. Cells Tissues Organs 63, 137–166. https://doi.org/10.1159/000142786

Fox, M.D., Corbetta, M., Vincent, J.L., Van Essen, D.C., Raichle, M.E., Snyder, A.Z., 2005. From The Cover: The human brain is intrinsically organized into dynamic, anticorrelated functional networks. Proc. Natl. Acad. Sci. https://doi.org/10.1073/pnas.0504136102

Friedman, J., Hastie, T., Tibshirani, R., 2010. Regularization Paths for Generalized Linear Models via Coordinate Descent. J. Stat. Softw. 33, 1–22.

https://doi.org/10.1359/JBMR.0301229

Fritsch, G.T., Hitzig, E., 1870. Ueber die elektrische Erregbarkeit des Grosshirns. Arch. fuer Anat. Physiol. und wissenschaftliche Med.

Gardner, R.C., Boxer, A.L., Trujillo, A., Mirsky, J.B., Guo, C.C., Gennatas, E.D., Heuer, H.W., Fine, E., Zhou, J., Kramer, J.H., Miller, B.L., Seeley, W.W., 2013. Intrinsic connectivity network disruption in progressive supranuclear palsy. Ann. Neurol. 73, 603–616. https://doi.org/10.1002/ana.23844

Garrison, K.A., Scheinost, D., Finn, E.S., Shen, X., Constable, R.T., 2015. The (in)stability of functional brain network measures across thresholds. Neuroimage. https://doi.org/10.1016/j.neuroimage.2015.05.046

Genovese, C.R., Lazar, N.A., Nichols, T., 2002. Thresholding of Statistical Maps in Functional Neuroimaging Using the False Discovery Rate. Neuroimage 15, 870–878. https://doi.org/10.1006/nimg.2001.1037

Ghahremani, D.G., Lee, B., Robertson, C.L., Tabibnia, G., Morgan, A.T., De Shetler, N., Brown, A.K., Monterosso, J.R., Aron, A.R., Mandelkern, M.A., Poldrack, R.A., London, E.D., 2012. Striatal Dopamine D2/D3 Receptors Mediate Response Inhibition and Related Activity in Frontostriatal Neural Circuitry in Humans. J. Neurosci. https://doi.org/10.1523/jneurosci.4284-11.2012

Goetz, C.G., Tilley, B.C., Shaftman, S.R., Stebbins, G.T., Fahn, S., Martinez-Martin, P., Poewe, W., Sampaio, C., Stern, M.B., Dodel, R., Dubois, B., Holloway, R., Jankovic, J., Kulisevsky, J., Lang, A.E., Lees, A., Leurgans, S., LeWitt, P.A., Nyenhuis, D., Olanow, C.W., Rascol, O., Schrag, A., Teresi, J.A., van Hilten, J.J., LaPelle, N., Agarwal, P., Athar, S., Bordelan, Y., Bronte-Stewart, H.M., Camicioli, R., Chou, K., Cole, W., Dalvi, A., Delgado, H., Diamond, A., Dick, J.P., Duda, J., Elble, R.J., Evans, C., Evidente, V.G., Fernandez, H.H., Fox, S., Friedman, J.H., Fross, R.D., Gallagher, D., Goetz, C.G., Hall, D., Hermanowicz, N., Hinson, V., Horn, S., Hurtig, H., Kang, U.J., Kleiner-Fisman, G., Klepitskaya, O., Kompoliti, K., Lai, E.C., Leehey, M.L., Leroi, I., Lyons, K.E., McClain, T., Metzer, S.W., Miyasaki, J., Morgan, J.C., Nance, M., Nemeth, J., Pahwa, R., Parashos, S.A., Schneider, J.S.J.S., Schrag, A., Sethi, K., Shulman, L.M., Siderowf, A., Silverdale, M., Simuni, T., Stacy, M., Stern, M.B., Stewart, R.M., Sullivan, K., Swope, D.M., Wadia, P.M., Walker, R.W.R., Walker, R.W.R., Weiner, W.J., Wiener, J., Wilkinson, J., Wojcieszek, J.M., Wolfrath, S., Wooten, F., Wu, A., Zesiewicz, T.A., Zweig, R.M., 2008. Movement Disorder Society-Sponsored Revision of the Unified Parkinson's Disease Rating Scale (MDS-UPDRS): Scale presentation and clinimetric testing results. Mov. Disord. 23, 2129–2170. https://doi.org/10.1002/mds.22340

Golbe, L.I., Davis, P.H., Schoenberg, B.S., Duvoisin, R.C., 1988. Prevalence and natural history of progressive supranuclear palsy. Neurology 38, 1031–4. https://doi.org/10.1212/WNL.38.7.1031

Gorell, J.M., Ordidge, R.J., Brown, G.G., Deniau, J.C., Buderer, N.M., Helpern, J.A., 1995. Increased iron-related MRI contrast in the substantia nigra in Parkinson's disease [published erratum appears in Neurology 1995 Jul;45(7):1420]. Neurology.

Gottfried, J.A., O'Doherty, J., Dolan, R.J., 2003. Encoding predictive reward value in human amygdala and orbitofrontal cortex. Science (80-.). https://doi.org/10.1126/science.1087919

Goulden, N., Khusnulina, A., Davis, N.J., Bracewell, R.M., Bokde, A.L., McNulty, J.P., Mullins, P.G., 2014. The salience network is responsible for switching between the default mode network and the central executive network: Replication from DCM. Neuroimage.

https://doi.org/10.1016/j.neuroimage.2014.05.052

Greicius, M.D., Krasnow, B., Reiss, A.L., Menon, V., 2003. Functional connectivity in the resting brain: A network analysis of the default mode hypothesis. Proc. Natl. Acad. Sci. https://doi.org/10.1073/pnas.0135058100

Greicius, M.D., Supekar, K., Menon, V., Dougherty, R.F., 2009. Resting-State Functional Connectivity Reflects Structural Connectivity in the Default Mode Network. Cereb. Cortex 19, 72–78. https://doi.org/10.1093/cercor/bhn059

Gunther, M., Oshio, K., Feinberg, D.A., 2005. Single-shot 3D imaging techniques improve arterial spin labeling perfusion measurements. Magn Reson Med. https://doi.org/10.1002/mrm.20580

Gupta, D., Saini, J., Kesavadas, C., Sarma, P.S., Kishore, A., 2010. Utility of susceptibility-weighted MRI in differentiating Parkinson’s disease and atypical parkinsonism. Neuroradiology. https://doi.org/10.1007/s00234-010-0677-6

Haacke, E.M., Brown, R.W., Thompson, M.R., Venkatesan, R., 1999. Haacke - Magnetic Resonance Imaging - Physical Principles and Sequence Design.pdf, Journal of Applied Physics. https://doi.org/10.1063/1.3554697

Haber, S.N., 2011. Neuroanatomy of Reward: A View from the Ventral Striatum, Neurobiology of Sensation and Reward.

Haber, S.N., Behrens, T.E.J., 2014. The Neural Network Underlying Incentive-Based Learning: Implications for Interpreting Circuit Disruptions in Psychiatric Disorders. Neuron. https://doi.org/10.1016/j.neuron.2014.08.031

Hacker, C.D., Perlmutter, J.S., Criswell, S.R., Ances, B.M., Snyder, A.Z., 2012. Resting state functional connectivity of the striatum in Parkinson’s disease. Brain 135, 3699–3711.

https://doi.org/10.1093/brain/aws281

Hadland, K.A., Rushworth, M.F.S., Gaffan, D., Passingham, R.E., 2003. The anterior cingulate and reward-guided selection of actions. J. Neurophysiol. 89, 1161–4. https://doi.org/10.1152/jn.00634.2002

Hagmann, P., Cammoun, L., Gigandet, X., Meuli, R., Honey, C.J., Van Wedeen, J., Sporns, O., 2008. Mapping the structural core of human cerebral cortex. PLoS Biol. https://doi.org/10.1371/journal.pbio.0060159

Hauw, J.J., Daniel, S.E., Dickson, D., Horoupian, D.S., Jellinger, K., Lantos, P.L., McKee, A., Tabaton, M., Litvan, I., 1994. Preliminary NINDS neuropathologic criteria for Steele-Richardson-Olszewski syndrome (progressive supranuclear palsy). Neurology 44, 2015–9. https://doi.org/10.1212/WNL.44.11.2015

Hein, K.H.M., Neher, P., Christophe, J., Alexandre, M., 2016. Tractography - based connectomes are dominated by false - positive connections. bioRxiv. https://doi.org/http://dx.doi.org/10.1101/084137

Helmich, R.C., Derikx, L.C., Bakker, M., Scheeringa, R., Bloem, B.R., Toni, I., 2010. Spatial remapping of cortico-striatal connectivity in parkinson’s disease. Cereb. Cortex. https://doi.org/10.1093/cercor/bhp178

Henssen, A., Zilles, K., Palomero-Gallagher, N., Schleicher, A., Mohlberg, H., Gerboga, F., Eickhoff, S.B., Bludau, S., Amunts, K., 2016. Cytoarchitecture and probability maps of the human medial orbitofrontal cortex. Cortex. https://doi.org/10.1016/j.cortex.2015.11.006

Hitchcott, P.K., Bonardi, C.M.T., Phillips, G.D., 1997. Enhanced stimulus-reward learning by intra-amygdala administration of a D3 dopamine receptor agonist. Psychopharmacology (Berl). 133, 240–248. https://doi.org/10.1007/s002130050397

Honey, C.J., Sporns, O., Cammoun, L., Gigandet, X., Thiran, J.P., Meuli, R., Hagmann, P., 2009. Predicting human resting-state functional connectivity from structural connectivity. Proc. Natl. Acad. Sci. https://doi.org/10.1073/pnas.0811168106

Hu, Y., Salmeron, B.J., Gu, H., Stein, E.A., Yang, Y., 2015. Impaired Functional Connectivity Within and Between Frontostriatal Circuits and Its Association With Compulsive Drug Use and Trait Impulsivity in Cocaine Addiction. JAMA psychiatry 21224, 584. https://doi.org/10.1001/jamapsychiatry.2015.1

Hyman, S., Sydor, A., Brown, R., Malenka, R., Nestler, E., 2009. Molecular Neuropharmacology: A Foundation for Clinical Neuroscience, Second Edition, in: Molecular Neuropharmacology: A Foundation for Clinical Neuroscience (2nd Ed.). pp. 265–266.

Ikemoto, S., Panksepp, J., 1999. The role of nucleus accumbens dopamine in motivated behavior: a unifying interpretation with special reference to reward-seeking. Brain Res. Rev. 31, 6–41. https://doi.org/10.1016/S0165-0173(99)00023-5

Immisch, I., Quintern, J., Straube, A., 2003. Unilateral cerebellar lesions influence arm movements bilaterally. Neuroreport 14, 837–40. https://doi.org/10.1097/01.wnr.0000069060.85441.bb

Ishizawa, K., Lin, W.L., Tiseo, P., Honer, W.G., Davies, P., Dickson, D.W., 2000. A qualitative and quantitative study of grumose degeneration in progressive supranuclear palsy. J. Neuropathol. Exp. Neurol. 59, 513–24.

Jäncke, L., Specht, K., Mirzazade, S., Peters, M., 1999. The Effect of Finger-Movement Speed of the Dominant and the Subdominant Hand on Cerebellar Activation: A Functional Magnetic Resonance Imaging Study. Neuroimage 9, 497–507.

https://doi.org/10.1006/nimg.1998.0426

Jankovic, J., 2008. Parkinson ' s disease : clinical features and diagnosis Parkinson ' s disease : clinical features and diagnosis. J. Neurol. Neurosurg. Physiatry. https://doi.org/10.1136/jnnp.2007.131045

Jann, K., Gee, D.G., Kilroy, E., Schwab, S., Smith, R.X., Cannon, T.D., Wang, D.J.J., 2015. Functional connectivity in BOLD and CBF data: similarity and reliability of resting brain networks. Neuroimage 106, 111–122. https://doi.org/10.1016/j.neuroimage.2014.11.028

Jann, K., Orosz, A., Dierks, T., Wang, D.J.J., Wiest, R., Federspiel, A., 2013. Quantification of network perfusion in ASL cerebral blood flow data with seed based and ICA approaches. Brain Topogr. 26, 569–580. https://doi.org/10.1007/s10548-013-0280-3

Jenkinson, M., Bannister, P., Brady, M., Smith, S., 2002. Improved optimization for the robust and accurate linear registration and motion correction of brain images. Neuroimage 17, 825–841. https://doi.org/10.1016/S1053-8119(02)91132-8

Johansen-Berg, H., Gutman, D.A., Behrens, T.E.J., Matthews, P.M., Rushworth, M.F.S., Katz, E., Lozano, A.M., Mayberg, H.S., 2008. Anatomical Connectivity of the Subgenual Cingulate Region Targeted with Deep Brain Stimulation for Treatment-Resistant Depression. Cereb. Cortex 18, 1374–1383. https://doi.org/10.1093/cercor/bhm167

Jueptner, M., Weiller, C., 1995. Does measurement of regional cerebral blood flow reflect synaptic activity?—Implications for PET and fMRI. Neuroimage. https://doi.org/10.1006/nimg.1995.1017

Juttukonda, M.R., Franco, G., Englot, D.J., Lin, Y.-C., Petersen, K.J., Trujillo, P., Hedera, P., Landman, B.A., Kang, H., Donahue, M.J., Konrad, P.E., Dawant, B.M., Claassen, D.O., 2019. White matter differences between essential tremor and Parkinson disease. Neurology

92, e30–e39. https://doi.org/10.1212/WNL.0000000000006694

Kahnt, T., Chang, L.J., Park, S.Q., Heinzle, J., Haynes, J.-D., 2012. Connectivity-based parcellation of the human orbitofrontal cortex. J. Neurosci. 32, 6240–50. https://doi.org/10.1523/JNEUROSCI.0257-12.2012

Kahnt, T., Park, S.Q., Heinzle, J., Chang, L.J., Haynes, J.-D., 2012. Connectivity-Based Parcellation of the Human Orbitofrontal Cortex. J. Neurosci. https://doi.org/10.1523/jneurosci.0257-12.2012

Kanazawa, M., Shimohata, T., Toyoshima, Y., Tada, M., Kakita, A., Morita, T., Ozawa, T., Takahashi, H., Nishizawa, M., 2009. Cerebellar involvement in progressive supranuclear palsy: A clinicopathological study. Mov. Disord. 24, 1312–1318. https://doi.org/10.1002/mds.22583

Kelly, C., Uddin, L.Q., Shehzad, Z., Margulies, D.S., Castellanos, F.X., Milham, M.P., Petrides, M., 2010. Broca's region: linking human brain functional connectivity data and non-human primate tracing anatomy studies. Eur. J. Neurosci. 32, 383–398. https://doi.org/10.1111/j.1460-9568.2010.07279.x

Kim, J.-H., Lee, J.-M., Jo, H.J., Kim, S.H., Lee, J.H., Kim, S.T., Seo, S.W., Cox, R.W., Na, D.L., Kim, S.I., Saad, Z.S., 2010. Defining functional SMA and pre-SMA subregions in human MFC using resting state fMRI: Functional connectivity-based parcellation method. Neuroimage 49, 2375–2386. https://doi.org/10.1016/J.NEUROIMAGE.2009.10.016

Kim, S.G., Hendrich, K., Hu, X., Merkle, H., Ugurbil, K., 1994. Potential pitfalls of functional MRI using conventional gradient- recalled echo techniques. NMR Biomed. 7, 69–74.

Kingsley, P.B., 2006. Introduction to diffusion tensor imaging mathematics: Part I. Tensors, rotations, and eigenvectors. Concepts Magn. Reson. Part A Bridg. Educ. Res.

https://doi.org/10.1002/cmr.a.20048

Knake, S., Belke, M., Menzler, K., Pilatus, U., Eggert, K.M., Oertel, W.H., Stamelou, M., Höglinger, G.U., 2010. In vivo demonstration of microstructural brain pathology in progressive supranuclear palsy: A DTI study using TBSS. Mov. Disord. 25, 1232–1238. https://doi.org/10.1002/mds.23054

Koch, M.A., Norris, D.G., Hund-Georgiadis, M., 2002. An investigation of functional and anatomical connectivity using magnetic resonance imaging. Neuroimage. https://doi.org/10.1006/nimg.2001.1052

Kouneiher, F., Charron, S., Koechlin, E., 2009. Motivation and cognitive control in the human prefrontal cortex. Nat. Neurosci. https://doi.org/10.1038/nn.2321

Kringelbach, M.L., 2005. The human orbitofrontal cortex: linking reward to hedonic experience. Nat. Rev. Neurosci. 6, 691–702. https://doi.org/10.1038/nrn1747

Kringelbach, M.L., n.d. for Functional Magnetic Resonance Imaging of the the human orbitofrontal cortex: linking reward to hedonic experience. https://doi.org/10.1038/nrn1747

Kringelbach, M.L., Rolls, E.T., 2004. The functional neuroanatomy of the human orbitofrontal cortex: evidence from neuroimaging and neuropsychology. Prog. Neurobiol. 72, 341–372. https://doi.org/10.1016/J.PNEUROBIO.2004.03.006

Krings, T., Erberich, S.G., Roessler, F., Reul, J., Thron, A., 1999. MR blood oxygenation level-dependent signal differences in parenchymal and large draining vessels: Implications for functional MR imaging. Am. J. Neuroradiol.

Küper, M., Thürling, M., Stefanescu, R., Maderwald, S., Roths, J., Elles, H.G., Ladd, M.E., Diedrichsen, J., Timmann, D., 2012. Evidence for a motor somatotopy in the cerebellar dentate nucleus-An fMRI study in humans. Hum. Brain Mapp. 33, 2741–2749.

https://doi.org/10.1002/hbm.21400

Kwon, H.G., Hong, J.H., Hong, C.P., Lee, D.H., Ahn, S.H., Jang, S.H., 2011. Dentatorubrothalamic tract in human brain: diffusion tensor tractography study. Neuroradiology 53, 787–791. https://doi.org/10.1007/s00234-011-0878-7

Laird, A.R., Lancaster, J.L., Fox, P.T., 2005. BrainMap: The Social Evolution of a Human Brain Mapping Database. Neuroinformatics 3, 065–078. https://doi.org/10.1385/NI:3:1:065

Lawson, R.P., Drevets, W.C., Roiser, J.P., 2013. Defining the habenula in human neuroimaging studies. Neuroimage 64, 722–7. https://doi.org/10.1016/j.neuroimage.2012.08.076

Le Bihan, D., Breton, E., Lallemand, D., Grenier, P., Cabanis, E., Laval-Jeantet, M., 1986. MR imaging of intravoxel incoherent motions: application to diffusion and perfusion in neurologic disorders. Radiology. https://doi.org/10.1148/radiology.161.2.3763909

Li, Z., Vidorreta, M., Katchmar, N., Alsop, D.C., Wolf, D.H., Detre, J.A., 2018. Effects of resting state condition on reliability, trait specificity, and network connectivity of brain function measured with arterial spin labeled perfusion MRI. Neuroimage 173, 165–175. https://doi.org/10.1016/J.NEUROIMAGE.2018.02.028

Lu, H., Donahue, M.J., Van Zijl, P.C.M., 2006. Detrimental effects of BOLD signal in arterial spin labeling fMRI at high field strength. Magn. Reson. Med. 56, 546–552. https://doi.org/10.1002/mrm.20976

Luo, C.Y., Song, W., Chen, Q., Zheng, Z.Z., Chen, K., Cao, B., Yang, J., Li, J.P., Huang, X.Q., Gong, Q.Y., Shang, H.F., 2014. Reduced functional connectivity in early-stage drug-naive Parkinson's disease: A resting-state fMRI study. Neurobiol. Aging. https://doi.org/10.1016/j.neurobiolaging.2013.08.018

Maldjian, J., 1994. WFU PickAtlas User Manual v2 . 4. Hum. Brain Mapp. 63, 1–13.

Maleki, N., Dai, W., Alsop, D.C., 2012. Optimization of background suppression for arterial spin labeling perfusion imaging. Magn. Reson. Mater. Physics, Biol. Med. https://doi.org/10.1007/s10334-011-0286-3

Mark, M.H., 2001. Lumping and splitting the Parkinson Plus syndromes: dementia with Lewy bodies, multiple system atrophy, progressive supranuclear palsy, and cortical-basal ganglionic degeneration. Neurol. Clin.

McFarland, N.R., Haber, S.N., 2000. Convergent inputs from thalamic motor nuclei and frontal cortical areas to the dorsal striatum in the primate. J. Neurosci.

McKeown, M.J., Makeig, S., Brown, G.G., Jung, T.P., Kindermann, S.S., Bell, A.J., Sejnowski, T.J., 1998. Analysis of fMRI data by blind separation into independent spatial components. Hum. Brain Mapp. https://doi.org/10.1002/(SICI)1097-0193(1998)6:3<160::AID-HBM5>3.0.CO;2-1

Menke, R.A., Scholz, J., Miller, K.L., Deoni, S., Jbabdi, S., Matthews, P.M., Zarei, M., 2009. MRI characteristics of the substantia nigra in Parkinson's disease: A combined quantitative T1 and DTI study. Neuroimage. https://doi.org/10.1016/j.neuroimage.2009.05.017

Menzies, L., Chamberlain, S.R., Laird, A.R., Thelen, S.M., Sahakian, B.J., Bullmore, E.T., 2008. Integrating evidence from neuroimaging and neuropsychological studies of obsessive-compulsive disorder: The orbitofronto-striatal model revisited. Neurosci. Biobehav. Rev. 32, 525–549. https://doi.org/10.1016/j.neubiorev.2007.09.005

Meola, A., Comert, A., Yeh, F.-C., Sivakanthan, S., Fernandez-Miranda, J.C., 2016. The nondecussating pathway of the dentatorubrothalamic tract in humans: human connectome-based tractographic study and microdissection validation. J. Neurosurg. 124, 1406–1412. https://doi.org/10.3171/2015.4.JNS142741

Mesulam, M.M., 1994. Distributed locality and large-scale neurocognitive networks. Behav. Brain Sci. https://doi.org/10.1017/S0140525X0003346X

Middleton, F.A., Strick, P.L., 2000. Basal ganglia and cerebellar loops: Motor and cognitive circuits, in: Brain Research Reviews. https://doi.org/10.1016/S0165-0173(99)00040-5

Middleton, F.A., Strick, P.L., 1998. Cerebellar output: motor and cognitive channels. Trends Cogn. Sci. 2, 348–354. https://doi.org/10.1016/S1364-6613(98)01220-0

Mishra, A., Rogers, B.P., Chen, L.M., Gore, J.C., 2014. Functional connectivity-based parcellation of amygdala using self-organized mapping: A data driven approach. Hum. Brain Mapp. 35, 1247–1260. https://doi.org/10.1002/hbm.22249

Morel, A., Magnin, M., Jeanmonod, D., 1997. Multiarchitectonic and stereotactic atlas f the human thalamus. J. Comp. Neurol. 387, 588–630. https://doi.org/10.1002/(SICI)1096-9861(19971103)387:4<588::AID-CNE8>3.0.CO;2-Z

Morgane, P.J., Mokler, D.J., 2006. The limbic brain: Continuing resolution. Neurosci. Biobehav. Rev. https://doi.org/10.1016/j.neubiorev.2005.04.020

Mori, S., Wakana, S., Nagae-Poetscher, L.M., Van Zijl, P.C.M., 2005. MRI Atlas of Human White Matter, American Journal of Neuroradiology. https://doi.org/10.1016/B978-008043924-2/50055-9

Mukherjee, P., Berman, J.I., Chung, S.W., Hess, C.P., Henry, R.G., 2008. Diffusion tensor MR imaging and fiber tractography: Theoretic underpinnings. Am. J. Neuroradiol. https://doi.org/10.3174/ajnr.A1051

Müller-Oehring, E.M., Sullivan, E. V., Pfefferbaum, A., Huang, N.C., Poston, K.L., Bronte-Stewart, H.M., Schulte, T., 2015. Task-rest modulation of basal ganglia connectivity in mild to moderate Parkinson's disease. Brain Imaging Behav. https://doi.org/10.1007/s11682-014-

9317-9

Murray, A.M., Ryoo, H.L., Gurevich, E., Joyce, J.N., 1994. Localization of dopamine D3 receptors to mesolimbic and D2 receptors to mesostriatal regions of human forebrain. Proc. Natl. Acad. Sci. U. S. A. 91, 11271–5. https://doi.org/10.1073/pnas.91.23.11271

Murray, E.A., 2007. The amygdala, reward and emotion. Trends Cogn. Sci. 11, 489–497. https://doi.org/10.1016/j.tics.2007.08.013

Musiek, E.S., Chen, Y., Korczykowski, M., Saboury, B., Martinez, P.M., Reddin, J.S., Alavi, A., Kimberg, D.Y., Wolk, D.A., Julin, P., Newberg, A.B., Arnold, S.E., Detre, J.A., 2012. Direct comparison of fluorodeoxyglucose positron emission tomography and arterial spin labeling magnetic resonance imaging in Alzheimer's disease. Alzheimer's Dement. 8, 51–59. https://doi.org/10.1016/j.jalz.2011.06.003

N/A, 2015. NINDS | Parkinson's Disease | Challenges, Progress, and Promise [WWW Document]. 15-5595.

Nelson, S.M., Dosenbach, N.U.F., Cohen, A.L., Wheeler, M.E., Schlaggar, B.L., Petersen, S.E., 2010. Role of the anterior insula in task-level control and focal attention. Brain Struct. Funct. 214, 669–680. https://doi.org/10.1007/s00429-010-0260-2

O'Doherty, J., Rolls, E.T., Francis, S., Bowtell, R., McGlone, F., Kobal, G., Renner, B., Ahne, G., 2000. Sensory-specific satiety-related olfactory activation of the human orbitofrontal cortex. Neuroreport. https://doi.org/10.1097/00001756-200003200-00046

Ogawa, S., Lee, T.M., Kay, A.R., Tank, D.W., 1990. Brain magnetic resonance imaging with contrast dependent on blood oxygenation. Proc. Natl. Acad. Sci. https://doi.org/10.1073/pnas.87.24.9868

Ogawa, S., Menon, R.S., Tank, D.W., Kim, S.G., Merkle, H., Ellermann, J.M., Ugurbil, K.,

1993. Functional brain mapping by blood oxygenation level-dependent contrast magnetic resonance imaging. A comparison of signal characteristics with a biophysical model. Biophys. J. 64, 803–812. https://doi.org/10.1016/S0006-3495(93)81441-3

Ojemann, J.G., Akbudak, E., Snyder, A.Z., McKinstry, R.C., Raichle, M.E., Conturo, T.E., 1997. Anatomic Localization and Quantitative Analysis of Gradient Refocused Echo-Planar fMRI Susceptibility Artifacts. Neuroimage 6, 156–167. https://doi.org/10.1006/NIMG.1997.0289

Olds, J., Milner, P., 1954. Positive reinforcement produced by electrical stimulation of septal area and other regions of rat brain. J. Comp. Physiol. Psychol. 47, 419–427. https://doi.org/10.1037/h0058775

Oshio, K., Feinberg, D. a, 1991. GRASE (Gradient- and spin-echo) imaging: a novel fast MRI technique. Magn. Reson. Med. 20, 344–349. https://doi.org/10.1002/mrm.1910200219

Padoa-Schioppa, C., 2011. Neurobiology of Economic Choice: A Good-Based Model. Annu. Rev. Neurosci. https://doi.org/10.1146/annurev-neuro-061010-113648

Pandya, D.N., Yeterian, E.H., 2013. Architecture and Connections of Cortical Association Areas. https://doi.org/10.1007/978-1-4757-9619-3_1

Park, H.J., Friston, K., 2013. Structural and functional brain networks: From connections to cognition. Science (80-.). https://doi.org/10.1126/science.1238411

Patenaude, B., Smith, S.M., Kennedy, D.N., Jenkinson, M., 2011. A Bayesian model of shape and appearance for subcortical brain segmentation. Neuroimage 56, 907–922. https://doi.org/10.1016/j.neuroimage.2011.02.046

Penfield, W., Boldrey, E., 1937. Somatic motor and sensory representation in the cerebral cortex of man as studied by electrical stimulation. Brain. https://doi.org/10.1093/brain/60.4.389

Perez-Lloret, S., Rey, M. V, Fabre, N., Ory, F., Spampinato, U., Montastruc, J.-L., Rascol, O.,

2011. Impulse-control disorders in Parkinson’s disease patients. Eur. J. Neurol. 18, 483.

Pessiglione, M., 2005. Thalamic Neuronal Activity in Dopamine-Depleted Primates: Evidence for a Loss of Functional Segregation within Basal Ganglia Circuits. J. Neurosci. https://doi.org/10.1523/jneurosci.4056-04.2005

Peters, S.K., Dunlop, K., Downar, J., 2016. Cortico-Striatal-Thalamic Loop Circuits of the Salience Network: A Central Pathway in Psychiatric Disease and Treatment. Front. Syst. Neurosci. 10, 104. https://doi.org/10.3389/fnsys.2016.00104

Petersen, K.J., Claassen, D.O., Donahue, M.J., 2017. Functional connectivity mapping using 3D GRASE arterial spin labeling MRI, in: International Society for Magnetic Resonance in Medicine.

Pierce, R.C., Kumaresan, V., 2006. The mesolimbic dopamine system: The final common pathway for the reinforcing effect of drugs of abuse? Neurosci. Biobehav. Rev. https://doi.org/10.1016/j.neubiorev.2005.04.016

Poewe, W., Gauthier, S., Aarsland, D., Leverenz, J.B., Barone, P., Weintraub, D., Tolosa, E., Dubois, B., 2008. Diagnosis and management of Parkinson ’ s disease dementia. Int. J. https://doi.org/10.1111/j.1742-1241.2008.01869.x

Price, J.L., 2010. Connections of orbital cortex, in: The Orbitofrontal Cortex. pp. 1–20. https://doi.org/10.1093/acprof:oso/9780198565741.003.0003

Raichle, M.E., 2015. The Brain’s Default Mode Network. Annu. Rev. Neurosci. https://doi.org/10.1146/annurev-neuro-071013-014030

Rane, S., Mason, E., Hussey, E., Gore, J., Ally, B.A., Donahue, M.J., 2014. The effect of echo time and post-processing procedure on blood oxygenation level-dependent (BOLD) functional connectivity analysis. Neuroimage 95, 39–47.

https://doi.org/10.1016/j.neuroimage.2014.03.055

Rolls, E.T., 2002. The Orbitofrontal Cortex and Reward. Cereb. Cortex. https://doi.org/10.1093/cercor/10.3.284

Sarter, M., Berntson, G.G., Cacioppo, J.T., 1996. Brain Imaging and Cognitive Neuroscience: Toward Strong Inference in Attributing Function to Structure. Am. Psychol. https://doi.org/10.1037/0003-066X.51.1.13

Sauseng, P., Klimesch, W., Schabus, M., Doppelmayr, M., 2005. Fronto-parietal EEG coherence in theta and upper alpha reflect central executive functions of working memory, in: International Journal of Psychophysiology. https://doi.org/10.1016/j.ijpsycho.2005.03.018

Schlaier, J., Anthofer, J., Steib, K., Fellner, C., Rothenfusser, E., Brawanski, A., Lange, M., 2015. Deep Brain Stimulation for Essential Tremor: Targeting the Dentato-Rubro-Thalamic Tract? Neuromodulation Technol. Neural Interface 18, 105–112. https://doi.org/10.1111/ner.12238

Seehaus, A.K., Roebroeck, A., Chiry, O., Kim, D.S., Ronen, I., Bratzke, H., Goebel, R., Galuske, R.A.W., 2013. Histological validation of DW-MRI tractography in human postmortem tissue. Cereb. Cortex. https://doi.org/10.1093/cercor/bhs036

Seeley, W.W., Menon, V., Schatzberg, A.F., Keller, J., Glover, G.H., Kenna, H., Reiss, A.L., Greicius, M.D., 2007. Dissociable Intrinsic Connectivity Networks for Salience Processing and Executive Control. J. Neurosci. https://doi.org/10.1523/JNEUROSCI.5587-06.2007

Seppi, K., Schocke, M.F.H., Esterhammer, R., Kremser, C., Brenneis, C., Mueller, J., Boesch, S., Jaschke, W., Poewe, W., Wenning, G.K., 2003. Diffusion-weighted imaging discriminates progressive supranuclear palsy from PD, but not from the parkinson variant of multiple system atrophy. Neurology 60, 922–7.

https://doi.org/10.1212/01.WNL.0000049911.91657.9D

Sescousse, G., Caldú, X., Segura, B., Dreher, J.C., 2013. Processing of primary and secondary rewards: A quantitative meta-analysis and review of human functional neuroimaging studies. Neurosci. Biobehav. Rev. https://doi.org/10.1016/j.neubiorev.2013.02.002

Shima, K., Tanji, J., 1998. Role for cingulate motor area cells in voluntary movement selection based on reward. Science (80-.). 282, 1335–8. https://doi.org/10.1126/science.282.5392.1335

Shirota, Y., Hamada, M., Hanajima, R., Terao, Y., Matsumoto, H., Ohminami, S., Tsuji, S., Ugawa, Y., 2010. Cerebellar dysfunction in progressive supranuclear palsy: a transcranial magnetic stimulation study. Mov. Disord. 25, 2413–2419. https://doi.org/10.1002/mds.23298

Shulman, G.L., Fiez, J.A., Corbetta, M., Buckner, R.L., Miezin, F.M., Raichle, M.E., Petersen, S.E., 1997. Common blood flow changes across visual tasks: II. Decreases in cerebral cortex. J. Cogn. Neurosci. https://doi.org/10.1162/jocn.1997.9.5.648

Skudlarski, P., Jagannathan, K., Calhoun, V.D., Hampson, M., Skudlarska, B.A., Pearlson, G., 2008. Measuring brain connectivity: Diffusion tensor imaging validates resting state temporal correlations. Neuroimage. https://doi.org/10.1016/j.neuroimage.2008.07.063

Smith, S.M., Fox, P.T., Miller, K.L., Glahn, D.C., Fox, P.M., Mackay, C.E., Filippini, N., Watkins, K.E., Toro, R., Laird, A.R., Beckmann, C.F., 2009. Correspondence of the brain's functional architecture during activation and rest. Proc. Natl. Acad. Sci. 106, 13040–13045. https://doi.org/10.1073/pnas.0905267106

Smith, S.M., Jenkinson, M., Woolrich, M.W., Beckmann, C.F., Behrens, T.E.J., Johansen-Berg, H., Bannister, P.R., De Luca, M., Drobnjak, I., Flitney, D.E., Niazy, R.K., Saunders, J., Vickers, J., Zhang, Y., De Stefano, N., Brady, J.M., Matthews, P.M., 2004. Advances in functional and structural MR image analysis and implementation as FSL, in: NeuroImage. pp. S208–S219. https://doi.org/10.1016/j.neuroimage.2004.07.051

Smith, S.M., Nichols, T.E., 2009. Threshold-free cluster enhancement: Addressing problems of smoothing, threshold dependence and localisation in cluster inference. Neuroimage. https://doi.org/10.1016/j.neuroimage.2008.03.061

Song, S.K., Sun, S.W., Ramsbottom, M.J., Chang, C., Russell, J., Cross, A.H., 2002. Dysmyelination revealed through MRI as increased radial (but unchanged axial) diffusion of water. Neuroimage. https://doi.org/10.1006/nimg.2002.1267

Sørensen, 1948. {A method of establishing groups of equal amplitude in plant sociology based on similarity of species and its application to analyses of the vegetation on Danish commons}. Biol. Skr. 5.

Soteropoulos, D.S., Baker, S.N., 2008. Bilateral representation in the deep cerebellar nuclei. J. Physiol. 586, 1117–1136. https://doi.org/10.1113/jphysiol.2007.144220

Sotiropoulos, S.N., Jbabdi, S., Xu, J., Andersson, J.L., Moeller, S., Auerbach, E.J., Glasser, M.F., Hernandez, M., Sapiro, G., Jenkinson, M., Feinberg, D.A., Yacoub, E., Lenglet, C., Van Essen, D.C., Ugurbil, K., Behrens, T.E.J., 2013. Advances in diffusion MRI acquisition and processing in the Human Connectome Project. Neuroimage 80, 125–143. https://doi.org/10.1016/J.NEUROIMAGE.2013.05.057

Sporns, O., Chialvo, D.R., Kaiser, M., Hilgetag, C.C., 2004. Organization, development and function of complex brain networks. Trends Cogn. Sci. https://doi.org/10.1016/j.tics.2004.07.008

Sridharan, D., Levitin, D.J., Menon, V., 2008. A critical role for the right fronto-insular cortex in switching between central-executive and default-mode networks. Proc. Natl. Acad. Sci. https://doi.org/10.1073/pnas.0800005105

Stark, A.J., Smith, C.T., Lin, Y.-C., Petersen, K.J., Trujillo, P., Van Wouwe, N.C., Kang, X.H., Donahue, M.J., Kessler, R.M., Zald, D.H., Claassen, X.D.O., 2018a. Nigrostriatal and mesolimbic D<inf>2/3</inf>receptor expression in Parkinson's disease patients with compulsive reward-driven behaviors. J. Neurosci. 38. https://doi.org/10.1523/JNEUROSCI.3082-17.2018

Stark, A.J., Smith, C.T., Petersen, K.J., Trujillo, P., van Wouwe, N.C., Donahue, M.J., Kessler, R.M., Deutch, A.Y., Zald, D.H., Claassen, D.O., 2018b. [^{18}F]fallypride characterization of striatal and extrastriatal D2/3receptors in Parkinson's disease. NeuroImage Clin. 18. https://doi.org/10.1016/j.nicl.2018.02.010

Strick, P.L., Dum, R.P., Fiez, J.A., 2009. Cerebellum and Nonmotor Function. Annu. Rev. Neurosci. https://doi.org/10.1146/annurev.neuro.31.060407.125606

Surova, Y., Nilsson, M., Lätt, J., Lampinen, B., Lindberg, O., Hall, S., Widner, H., Nilsson, C., van Westen, D., Hansson, O., 2015. Disease-specific structural changes in thalamus and dentatorubrothalamic tract in progressive supranuclear palsy. Neuroradiology 57, 1079–1091. https://doi.org/10.1007/s00234-015-1563-z

Tahmasian, M., Bettray, L.M., van Eimeren, T., Drzezga, A., Timmermann, L., Eickhoff, C.R., Eickhoff, S.B., Eggers, C., 2015. A systematic review on the applications of resting-state fMRI in Parkinson's disease: Does dopamine replacement therapy play a role? Cortex. https://doi.org/10.1016/j.cortex.2015.08.005

Tambasco, N., Montanari, G.E., Pelliccioli, G.P., Mancini, M.L., Paciaroni, M., Gallai, V., Leone, F., Chiarini, P., 2016. Magnetization transfer changes of grey and white matter in

Parkinson’s disease. Neuroradiology. https://doi.org/10.1007/s00234-002-0925-5

Tanaka, S.C., Doya, K., Okada, G., Ueda, K., Okamoto, Y., Yamawaki, S., 2004. Prediction of immediate and future rewards differentially recruits cortico-basal ganglia loops. Nat. Neurosci. 7, 887–893. https://doi.org/10.1038/nn1279

Tessitore, A., Esposito, F., Vitale, C., Santangelo, G., Amboni, M., Russo, A., Corbo, D., Cirillo, G., Barone, P., Tedeschi, G., 2012. Default-mode network connectivity in cognitively unimpaired patients with Parkinson disease. Neurology. https://doi.org/10.1212/WNL.0b013e31827689d6

Thorpe, S.J., Rolls, E.T., Maddison, S., 1983. The orbitofrontal cortex: Neuronal activity in the behaving monkey. Exp. Brain Res. https://doi.org/10.1007/BF00235545

Tibshirani, R., 1996. Regression Selection and Shrinkage via the Lasso. J. R. Stat. Soc. B. https://doi.org/10.2307/2346178

Tomlinson, C.L., Stowe, R., Patel, S., Rick, C., Gray, R., Clarke, C.E., 2010. Systematic review of levodopa dose equivalency reporting in Parkinson’s disease. Mov. Disord. 25, 2649–2653. https://doi.org/10.1002/mds.23429

Torres, C. V., Moro, E., Lopez-Rios, A.-L., Hodaie, M., Chen, R., Laxton, A.W., Hutchison, W.D., Dostrovsky, J.O., Lozano, A.M., 2010. Deep Brain Stimulation of the Ventral Intermediate Nucleus of the Thalamus for Tremor in Patients With Multiple Sclerosis. Neurosurgery 67, 646–651. https://doi.org/10.1227/01.NEU.0000375506.18902.3E

Trujillo, P., Smith, A.K., Summers, P.E., Mainardi, L.M., Cerutti, S., Smith, S.A., Costa, A., 2015. High-resolution quantitative imaging of the substantia nigra, in: Proceedings of the Annual International Conference of the IEEE Engineering in Medicine and Biology Society, EMBS. https://doi.org/10.1109/EMBC.2015.7319619

Tye, K.M., Stuber, G.D., de Ridder, B., Bonci, A., Janak, P.H., 2008. Rapid strengthening of thalamo-amygdala synapses mediates cue–reward learning. Nature 453, 1253–1257. https://doi.org/10.1038/nature06963

Uylings, H.B.M., -Arigita, E.J.S., de Vos, K., Pool, C.W., Evers, P., Rajkowska, G., 2010. 3-D Cytoarchitectonic parcellation of human orbitofrontal cortex. Correlation with postmortem MRI. Psychiatry Res. - Neuroimaging. https://doi.org/10.1016/j.pscychresns.2010.04.012

Van Den Heuvel, M.P., Mandl, R.C.W., Kahn, R.S., Hulshoff Pol, H.E., 2009. Functionally linked resting-state networks reflect the underlying structural connectivity architecture of the human brain. Hum. Brain Mapp. https://doi.org/10.1002/hbm.20737

Van Wouwe, N.C., Claassen, D.O., Neimat, J.S., Kanoff, K.E., Wylie, S.A., 2017. Dopamine Selectively Modulates the Outcome of Learning Unnatural Action–Valence Associations. J. Cogn. Neurosci. 29, 816–826. https://doi.org/10.1162/jocn_a_01099

van Zijl, P.C., Eleff, S.M., Ulatowski, J.A., Oja, J.M., Uluğ, A.M., Traystman, R.J., Kauppinen, R.A., 1998. Quantitative assessment of blood flow, blood volume and blood oxygenation effects in functional magnetic resonance imaging. Nat. Med. 4, 159–67.

Verbree, J., van Osch, M.J.P., 2018. Influence of the cardiac cycle on pCASL: cardiac triggering of the end-of-labeling. Magn. Reson. Mater. Physics, Biol. Med. 31, 223–233. https://doi.org/10.1007/s10334-017-0611-6

Vidorreta, M., Wang, Z., Chang, Y. V., Wolk, D.A., Fernández-Seara, M.A., Detre, J.A., 2017. Whole-brain background-suppressed pCASL MRI with 1D-accelerated 3D RARE Stack-Of-Spirals readout. PLoS One. https://doi.org/10.1371/journal.pone.0183762

Viviani, R., Messina, I., Walter, M., 2011. Resting state functional connectivity in perfusion imaging: Correlation maps with Bold connectivity and resting state perfusion. PLoS One 6, e27050. https://doi.org/10.1371/journal.pone.0027050

Voon, V., Fox, S.H., 2007. Medication-Related Impulse Control and Repetitive Behaviors in Parkinson Disease. Arch. Neurol. 64, 1089. https://doi.org/10.1001/archneur.64.8.1089

Voon, V., Mehta, A.R., Hallett, M., 2011. Impulse control disorders in Parkinson's disease: Recent advances. Curr. Opin. Neurol. https://doi.org/10.1097/WCO.0b013e3283489687

Wallis, L.I., Paley, M.N.J., Graham, J.M., Grünewald, R.A., Wignall, E.L., Joy, H.M., Griffiths, P.D., 2008. MRI assessment of basal ganglia iron deposition in Parkinson's disease. J. Magn. Reson. Imaging. https://doi.org/10.1002/jmri.21563

Wedeen, V.J., Wang, R.P., Schmahmann, J.D., Benner, T., Tseng, W.Y.I., Dai, G., Pandya, D.N., Hagmann, P., D'Arceuil, H., de Crespigny, A.J., 2008. Diffusion spectrum magnetic resonance imaging (DSI) tractography of crossing fibers. Neuroimage. https://doi.org/10.1016/j.neuroimage.2008.03.036

Weintraub, D., 2009. Impulse control disorders in Parkinson's disease: prevalence and possible risk factors. Parkinsonism Relat. Disord. 15 Suppl 3, S110–S113. https://doi.org/10.1016/S1353-8020(09)70794-1

Weintraub, D., David, A.S., Evans, A.H., Grant, J.E., Stacy, M., 2015. Clinical spectrum of impulse control disorders in Parkinson's disease. Mov. Disord. 30, 121–127. https://doi.org/10.1002/mds.26016

Weissenbacher, A., Kasess, C., Gerstl, F., Lanzenberger, R., Moser, E., Windischberger, C., 2009. Correlations and anticorrelations in resting-state functional connectivity MRI: A quantitative comparison of preprocessing strategies. Neuroimage 47, 1408–1416. https://doi.org/10.1016/j.neuroimage.2009.05.005

Whitwell, J.L., Avula, R., Master, A., Vemuri, P., Senjem, M.L., Jones, D.T., Jack, C.R., Josephs, K.A., 2011. Disrupted thalamocortical connectivity in PSP: a resting-state fMRI, DTI, and VBM study. Parkinsonism Relat. Disord. 17, 599–605. https://doi.org/10.1016/j.parkreldis.2011.05.013

Whitwell, J.L., Schwarz, C.G., Reid, R.I., Kantarci, K., Jack, C.R., Josephs, K.A., 2014. Diffusion tensor imaging comparison of progressive supranuclear palsy and corticobasal syndromes. Parkinsonism Relat. Disord. 20, 493–8. https://doi.org/10.1016/j.parkreldis.2014.01.023

Wiesendanger, R., Wiesendanger, M., 1985. Cerebello-cortical linkage in the monkey as revealed by transcellular labeling with the lectin wheat germ agglutinin conjugated to the marker horseradish peroxidase. Exp Brain Res 59, 105–117.

Williams, D.R., Holton, J.L., Strand, C., Pittman, A., De Silva, R., Lees, A.J., Revesz, T., 2007. Pathological tau burden and distribution distinguishes progressive supranuclear palsy-parkinsonism from Richardson's syndrome. Brain 130, 1566–1576. https://doi.org/10.1093/brain/awm104

Williams, D.S., Detre, J.A., Leigh, J.S., Koretsky, A.P., 1992. Magnetic resonance imaging of perfusion using spin inversion of arterial water. Proc. Natl. Acad. Sci. U. S. A. 89, 212–6.

Woolrich, M.W., Ripley, B.D., Brady, M., Smith, S.M., 2001. Temporal Autocorrelation in Univariate Linear Modeling of FMRI Data. Neuroimage 14, 1370–1386. https://doi.org/10.1006/NIMG.2001.0931

Xue, G., Lu, Z., Levin, I.P., Bechara, A., 2010. The impact of prior risk experiences on subsequent risky decision-making: The role of the insula. Neuroimage 50, 709–716. https://doi.org/10.1016/j.neuroimage.2009.12.097

Yamada, K., 2009. Diffusion tensor tractography should be used with caution. Proc. Natl. Acad.

Sci. https://doi.org/10.1073/pnas.0812352106

Yeo, B.T.T., Krienen, F.M., Sepulcre, J., Sabuncu, M.R., Lashkari, D., Hollinshead, M., Roffman, J.L., Smoller, J.W., Zöllei, L., Polimeni, J.R., Fischl, B., Liu, H., Buckner, R.L., 2011. The organization of the human cerebral cortex estimated by intrinsic functional connectivity. J. Neurophysiol. 106, 1125–65. https://doi.org/10.1152/jn.00338.2011

Yu, R., Liu, B., Wang, L., Chen, J., Liu, X., 2013. Enhanced Functional Connectivity between Putamen and Supplementary Motor Area in Parkinson's Disease Patients. PLoS One. https://doi.org/10.1371/journal.pone.0059717

Zald, D.H., McHugo, M., Ray, K.L., Glahn, D.C., Eickhoff, S.B., Laird, A.R., 2014. Meta-Analytic Connectivity Modeling Reveals Differential Functional Connectivity of the Medial and Lateral Orbitofrontal Cortex. Cereb. Cortex 24, 232–248. https://doi.org/10.1093/cercor/bhs308

Zeeb, F.D., Floresco, S.B., Winstanley, C.A., 2010. Contributions of the orbitofrontal cortex to impulsive choice: interactions with basal levels of impulsivity, dopamine signalling, and reward-related cues. Psychopharmacology (Berl). 211, 87–98. https://doi.org/10.1007/s00213-010-1871-2

Zhang, S., Li, C.R., 2012. Functional connectivity mapping of the human precuneus by resting state fMRI. Neuroimage 59, 3548–3562. https://doi.org/10.1016/J.NEUROIMAGE.2011.11.023

Zhang, Y., Walter, R., Ng, P., Luong, P.N., Dutt, S., Heuer, H., Rojas-Rodriguez, J.C., Tsai, R., Litvan, I., Dickerson, B.C., Tartaglia, M.C., Rabinovici, G., Miller, B.L., Rosen, H.J., Schuff, N., Boxer, A.L., 2016. Progression of Microstructural Degeneration in Progressive Supranuclear Palsy and Corticobasal Syndrome: A Longitudinal Diffusion Tensor Imaging

Study. PLoS One 11, e0157218. https://doi.org/10.1371/journal.pone.0157218

Zhang, Y., Zhang, J., Xu, J., Wu, X., Zhang, Y., Feng, H., Wang, J., Jiang, T., 2014. Cortical gyrification reductions and subcortical atrophy in Parkinson's disease. Mov. Disord. 29, 122–126. https://doi.org/10.1002/mds.25680

Zikopoulos, B., Höistad, M., John, Y., Barbas, H., 2017. Posterior Orbitofrontal and Anterior Cingulate Pathways to the Amygdala Target Inhibitory and Excitatory Systems with Opposite Functions. J. Neurosci. 37, 5051–5064. https://doi.org/10.1523/JNEUROSCI.3940-16.2017

Zou, Q., Wu, C.W., Stein, E.A., Zang, Y., Yang, Y., 2009. Static and dynamic characteristics of cerebral blood flow during the resting state. Neuroimage 48, 515–524. https://doi.org/10.1016/j.neuroimage.2009.07.006